Universität der Bundeswehr München
Fakultät für Luft- und Raumfahrttechnik
Institut für Thermodynamik

Conjugate Heat Transfer Simulations for Hypersonic Flight

Axel Buck, M.Sc.

Vollständiger Abdruck der von der
Fakultät für Luft- und Raumfahrttechnik
der Universität der Bundeswehr München
zur Erlangung des akademischen Grades eines

Doktor-Ingenieurs (Dr.-Ing.)

genehmigten Dissertation

Vorsitzender: Prof. Dr.-Ing. habil. Lars Zigan
1. Berichterstatter: Prof. Dr.-Ing. Christian Mundt
2. Berichterstatter: Prof. Dr.-Ing. habil. Cord-Christian Rossow

Die Dissertation wurde am 11.01.2024 bei der Universität der Bundeswehr München eingereicht und durch die Fakultät für Luft- und Raumfahrttechnik am 12.04.2024 angenommen.

Tag der Prüfung: 16.05.2024

Preface

Die vorliegende Arbeit entstand während meiner Zeit als wissenschaftlicher Mitarbeiter am Institut für Thermodynamik der Universität der Bundeswehr München.

Zunächst möchte ich mich bei meinem Doktorvater Prof. Dr.-Ing. Christian Mundt bedanken, der mir die Möglichkeit gegeben hat, in diesem sehr spannenden Themenbereich zu promovieren. Ich weiß die Chance, mich weiterzubilden und einen Beitrag zur Wissenschaft zu leisten, sehr zu schätzen. Hervorheben möchte ich dabei die Freiheiten, die Sie mir in der Ausrichtung meiner Dissertation gegeben haben, die Möglichkeit Konferenzen zu besuchen und das Vertrauen in mich bei den bearbeiteten Projekten. Weiterhin bedanke ich mich bei Prof. Dr.-Ing. habil. Cord-Christian Rossow für die Übernahme des Koreferats und bei Prof. Dr.-Ing. habil. Lars Zigan für die Übernahme des Prüfungsvorsitzes.

Des Weiteren möchte ich mich beim gesamten Institut LRT10 für die angenehme Arbeitsatmosphäre in den letzten Jahren bedanken. Die fachlichen Diskussionen mit den Kollegen haben oft sehr geholfen, vor allem aber den persönlichen Austausch innerhalb und außerhalb des Instituts, beim Spritwoch und den vielfältigen Ausflügen werde ich sehr vermissen. Vielen Dank hier vor allem an Marvin Feike, Dominik James und Fabian Teschner. Dominik James bin ich zusätzlich für die Übernahme des Lektorates zu Dank verpflichtet.

Zuletzt möchte ich mich bei meinen Eltern bedanken, die mich immer unterstützt haben. Ohne Euch wäre das so nicht möglich gewesen.

21.05.2024
Axel Buck

Abstract

In recent years, interest in hypersonic flight was renewed due to promising new civil and military applications. Because of the high Mach number, hypersonic flows are characterized by a large thermal load on the vehicle, accurate prediction of which is crucial for mission success. Coupled fluid/solid simulations, also known as Conjugate Heat Transfer (CHT) simulations can be used to determine the temperature distribution in the fluid and solid simultaneously.

In this thesis, the fluid mechanics solver NSMB (Navier Stokes Multi Block) was extended with CHT functionality. The solid domain is spatially discretized with the 3D finite-volume method, a time-accurate explicit Runge-Kutta method is used for the temporal discretization, and the two domains are tightly coupled. Along the domain interface, the CHT boundary condition is solved, which ensures energy conservation and temperature continuity. In addition to the conductive heat fluxes, the heat fluxes due to species diffusion and convex surface radiation are included. Constant and temperature-dependent material properties can be used for the solid material. Improvements for the turbulent heat flux model and bow shock mesh adaptation are also implemented in NSMB to improve the fluid solution. The CHT method was then successfully validated against multiple test cases.

An analysis of the implemented algorithm shows that a method that is first-order accurate in space at the solid/fluid interface is more robust than a second-order method. Furthermore, it was found that the heat flux due to species diffusion is negligible in equilibrium flows at moderate freestream Mach numbers. CHT analysis of a challenging shock/turbulent boundary layer interaction case reveals that unsteady heating effects can also be important for short duration experiments. The CHT simulation matched experimental results significantly better than fluid-only simulations. Finally, coupled simulations of a generic flap at different flap angles and forebody nose radii in hypersonic flow showed that a thick entropy layer can decrease the flap temperature and increase the flap effectiveness. Additionally, separation length increases due to the higher surface temperature in coupled simulations.

Kurzfassung

In den letzten Jahren gab es, aufgrund vielversprechender neuer ziviler und militärischer Anwendungen, ein erneuertes Interesse an Hyperschall-Flug. Wegen der hohen Machzahl zeichnen sich Hyperschall-Strömungen durch eine hohe thermische Last auf den Flugkörper aus. Diese muss korrekt bestimmt werden, um Hyperschall-Missionen erfolgreich durchführen zu können. Mittels gekoppelter Fluid/Festkörper Simulationen, auch Conjugate Heat Transfer (CHT) Simulationen genannt, kann die Temperaturverteilung in Fluid und Festkörper simultan bestimmt werden.

In dieser Arbeit wurde der Strömungslöser NSMB (Navier Stokes Multi Block) um CHT Funktionalität erweitert. Der Festkörper wird dabei mit der 3D-Finite-Volumen Methode diskretisiert, ein zeitechtes, explizites Runge-Kutta Verfahren wird für die Zeitdiskretisierung verwendet, und Fluid und Festkörper sind eng gekoppelt. An der Grenzfläche zwischen den beiden Bereichen wird die CHT Randbedingung aufgeprägt, die sicherstellt, dass Energie erhalten wird und der Temperaturverlauf kontinuierlich ist. Zusätzlich zu den Wärmeströmen durch Wärmeleitung wird Wärmetransport durch Spezies-Diffusion und der konvexe Wandwärmestrom berücksichtigt. Konstante und temperaturabhängige Materialeigenschaften des Festkörpers sind möglich. Des Weiteren wurde NSMB um ein verbessertes Modell für den turbulenten Wärmestrom und einen neuen Algorithmus zur Netzanpassung erweitert. Die CHT Methodik wurde dann mittels mehrerer Testfälle erfolgreich validiert.

Eine Analyse des implementierten Algorithmus zeigt, dass die Methode erster Ordnung an der Fluid/Festkörper-Grenzfläche robuster ist, als die Methode zweiter Ordnung. Des Weiteren stellte sich heraus, dass der Wärmestrom durch Spezies-Diffusion für Gleichgewichts-Strömungen bei moderaten Machzahlen vernachlässigbar ist. Die gekoppelte Simulation eines Falls mit Stoß/Grenzschicht Interaktion zeigt, dass instationäre Aufheizungseffekte auch für Strömungs-Probleme mit kurzer Dauer relevant sein können. In der CHT Simulation ist die Übereinstimmung mit den experimentellen Daten wesentlich besser als in der Simulation des Fluids allein. Zuletzt wurde eine generische Klappe mit verschiedenen Klappenwinkeln und Nasenradien mit Anströmung im Hyperschall untersucht. Die gekoppelte Simulation zeigt, dass eine dicke Entropieschicht die Klappentemperatur verringern und die Klappeneffektivität vergrößern kann. Außerdem vergrößert sich die Länge der Ablösung aufgrund der höheren Wandtemperatur in gekoppelten Simulationen.

Contents

List of Figures

List of Tables

Nomenclature

Latin symbols

A	Area	$[\mathrm{m}^2]$
a	Thermal diffusivity	$[\mathrm{m}^2/\mathrm{s}]$
C	Aerodynamic coefficient	$[-]$
C	Molar concentration	$[\mathrm{mol}/\mathrm{m}^3]$
c	Specific heat capacity	$[\mathrm{J}/\mathrm{kg\,K}]$
c	Speed of sound	$[\mathrm{m}/\mathrm{s}]$
E	Specific total energy	$[\mathrm{J}/\mathrm{kg}]$
e	Specific internal energy	$[\mathrm{J}/\mathrm{kg}]$
$\boldsymbol{F}$	Flux vector	
g	Specific gibbs energy	$[\mathrm{J}/\mathrm{kg}]$
H	Specific total enthalpy	$[\mathrm{J}/\mathrm{kg}]$
h	Specific enthalpy	$[\mathrm{J}/\mathrm{kg}]$
I_{sp}	Specific impulse	$[\mathrm{s}]$
K	Equilibrium constant	
k	Reaction rate coefficient	
k	Specific turbulence kinetic energy	$[\mathrm{J}/\mathrm{kg}]$
L	Reference length	$[\mathrm{m}]$
M	Molar mass	$[\mathrm{kg}/\mathrm{mol}]$
m	Mass	$[\mathrm{kg}]$
$\boldsymbol{n}$	Unit normal vector	$[-]$
p	Pressure	$[\mathrm{Pa}]$
Q	Heat	$[\mathrm{J}]$
q	Heat flux	$[\mathrm{W}/\mathrm{m}^2]$
R	Specific gas constant	$[\mathrm{J}/\mathrm{kg\,K}]$
S	Source term	
S	Strain rate	$[1/\mathrm{s}]$
s	Specific entropy	$[\mathrm{J}/\mathrm{K\,kg}]$
s	Surface coordinate	$[\mathrm{m}]$
T	Temperature	$[\mathrm{K}]$
t	Time	$[\mathrm{s}]$
U	Velocity magnitude	$[\mathrm{m}/\mathrm{s}]$
u_i	Velocity in i-direction	$[\mathrm{m}/\mathrm{s}]$
V	Volume	$[\mathrm{m}^3]$
$\boldsymbol{W}$	State vector	

| x, y, z | Spacial coordinates | [m] |
| Y | Species mass fraction | $[-]$ |

Greek symbols

α	Heat transfer coefficient	$[\mathrm{W}/\mathrm{m^2\,K}]$
δ_{ij}	Kronecker delta	
γ	Ratio of specific heats	$[-]$
ϵ	Turbulence dissipation	$[\mathrm{m^2}/\mathrm{s^3}]$
η	Kolmogorov length scale	[m]
λ	Thermal conductivity	$[\mathrm{W}/\mathrm{m\,K}]$
μ	Dynamic viscosity	$[\mathrm{Pa\,s}]$
ν	Kinematic viscosity	$[\mathrm{m^2}/\mathrm{s}]$
ν	Stoichiometric coefficient	$[-]$
ρ	Density	$[\mathrm{kg}/\mathrm{m^3}]$
τ	Shear stress	$[\mathrm{N}/\mathrm{m^2}]$
ϕ	Placeholder for scalar variable	
ω	Specific turbulence dissipation	$[\mathrm{1}/\mathrm{s}]$

Dimensionless numbers

Bi	Biot number
CFL	Courant-Friedrichs-Lewy Number
Da	Damköhler number
Kn	Knudsen number
Ma	Mach number
Pr	Prandtl number
Re	Reynolds number
Sc	Schmidt number

Abbreviations

CFD	Computational Fluid Dynamics
CHT	Conjugate Heat Transfer
DNS	Direct Numerical Simulation
EARSM	Explicit Algebraic Reynolds Stress Model
EDM	Eddy Diffusivity Model
ENO	Essentially Non-Oscillatory
ET	Equalized Timescales
EVM	Linear Eddy Viscosity Model
FEM	Finite-Element Method
FVM	Finite-Volume Method
HLLC	Harten, Lax, van Leer, Contact scheme
HLLE	Harten, Lax, van Leer, Einfeldt scheme
HLLESU	Harten, Lax, van Leer, Einfeldt Shock Unsteadiness scheme
LES	Large-Eddy Simulation

MUSCL	Monotonic Upstream-centered Scheme for Conservation Laws
NLEVM	Non-Linear Eddy Viscosity Model
NSMB	Navier Stokes Multi Block
RANS	Reynolds-Averaged Navier-Stokes
RSM	Reynolds Stress Model
RST	Reynolds Stress Tensor
STBLI	Shock/Turbulent Boundary Layer Interaction
STI	Shock Turbulence Interaction
TKE	Turbulence Kinetic Energy
URANS	Unsteady Reynolds-Averaged Navier-Stokes

Subscripts

∞	Freestream variable
F	Fluid
lam	Laminar
n	Wall normal
S	Solid
s	Species index
T	Turbulent
t	Total
W	Wall

Superscripts

n	Variable at time increment n

Accents

$\overline{\Box}$	Reynolds-average
$\hat{\Box}$	Filtered
$\tilde{\Box}$	Favre-average
$\Box'$	Reynolds-fluctuation
$\Box''$	Favre-fluctuation
$\Box'''$	Unresolved fluctuation in LES

Constants

$\mathscr{R}$	Universal gas constant	$8.314\,462\,\mathrm{J/mol\,K}$
σ	Stefan-Boltzmann constant	$5.670\,374 \times 10^{-8}\,\mathrm{W/m^2\,K^4}$

CHAPTER 1

Introduction

In the second half of the last century, significant efforts were made by multiple countries to achieve hypersonic flight [1]. Large milestones were achieved, such as the first manned reentry from space and the first flight of a hypersonic airplane [2]. During the past couple of years, interest renewed in hypersonic flight with proposals of civil hypersonic planes by newly formed companies and the looming threat of hypersonic weapon systems.

Early hypersonic flight was achieved by reentry vehicles, such as the Apollo and Soyuz capsules. Current development sees the introduction of hypersonic cruise missiles, while other programs shift towards hypersonic glide vehicles. Another concept that has recently been pursued is the hypersonic passenger or cargo plane. In addition to the significant reduction in travel times at hypersonic speed, there are even some claims of possible energy savings for high-speed passenger flight [3]. These are based on two factors: Firstly, the reduced travel time reduces the gravity losses during flight. Secondly, since the proposed hypersonic passenger flight takes place at much higher altitudes of around $30\,\text{km}$ compared to current passenger air traffic at around $11\,\text{km}$, the ambient air density is significantly lower, which reduces the aerodynamic drag.

Unlike the supersonic and subsonic flow regimes, the realm of hypersonic flow is best not defined by a single value of Mach number, but rather by the occurring physical effects. In the hypersonic regime, the kinetic energy of the incoming flow is large, resulting in high temperatures in the flow. This affects the boundary layer thickness and the thermodynamic state of the fluid. Typically, these processes become relevant at a Mach number $\text{Ma} = {}^{U}\!/_{c} > 5$.

It is important to note, however, that the total energy consumption of a flight not only consists of the energy consumption at cruise speed, but also the energy required to reach the cruise altitude. Whether hypersonic flight can become a fast and energy efficient mode of transport therefore depends on a range of other factors, such as vehicle weight, distance traveled, and possible flight corridors.

Hypersonic aerodynamic flight might also be the future of space missions, since a hypersonic airbreathing vehicle could accelerate the payload in the atmosphere. Concepts for such vehicles were proposed in the second half of the last century, but

ultimately failed due to engineering difficulties [2]. Since airbreathing engines only carry the fuel and use the ingested air as oxidizer, their specific impulse I_{sp} is significantly larger compared to rocket engines. While typical rocket engines have an I_{sp} of around $350\,s$, the I_{sp} of Ramjets and Scramjets can be one order of magnitude larger, depending on the operating conditions [4]. This significant increase in efficiency reduces the fuel consumption for space access and might help make space flight acceptable even in the face of climate change. To this day, however, access to space via an airbreathing vehicle has not yet been achieved.

1.1   Motivation

The new interest in hypersonic flight brings new challenges in vehicle design, which stem from the harsh environment that the vehicles must withstand. Ever-evolving computational capabilities together with new modeling approaches open the door for better numerical analysis. This, in turn, reduces the need for experimental data and in-flight testing, which lowers the cost and development time of new projects.

For the success of civil hypersonic flight, an accurate understanding of the aerothermodynamic behavior of the vehicle is crucial. Better understanding of aerodynamic heating allows engineers to optimize, i.e., reduce the thickness of thermal protection systems, which results in a lower overall vehicle weight. This lowers the energy consumption and operating cost. If hypersonic flight is to be used for passenger flight, a good understanding of the flow is especially important for safety reasons. In this thesis, numerical methods for simulating the heating of hypersonic vehicles are developed to progress towards these goals.

1.2   Aerodynamic Heating in High-Speed Flight

Unlike low-speed flows, which can have a cooling effect on a vehicle with $T_\infty < T_{vehicle}$, high speed flows are characterized by their strong aerodynamic heating. This is a result of the high kinetic energy of the gas, which is converted into internal energy during the compression at the front of the body. The resulting gas temperature near the body is therefore significantly higher than the freestream temperature. The ratio of the total temperature T_t to the static temperature T of a perfect gas scales with the square of the Mach number:

$$\frac{T_t}{T} = 1 + \frac{\gamma - 1}{2}\mathrm{Ma}^2. \tag{1.1}$$

Along the stagnation streamline of a blunt body, which is approximately an inviscid 1D compression, the total temperature is equal to the stagnation temperature. Figure 1.1 shows the ratio over the freestream Mach number for a ratio of specific heats $\gamma = 1.4$. While the value is near unity for $\mathrm{Ma}_\infty < 1$, it increases strongly with the Mach number, and exceeds $T_t/T = 6$ for hypersonic flight.
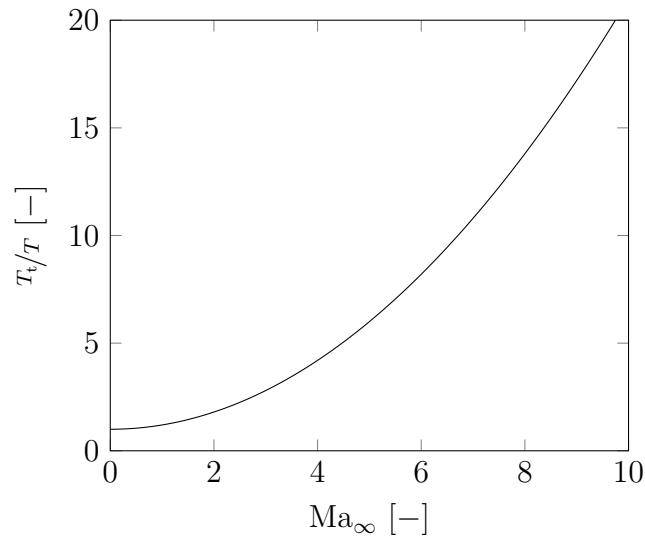
Figure 1.1: Ratio of total temperature to static temperature over freestream Mach number

An additional effect that has shown to affect the heating is entropy layer swallowing. To withstand the high heat load, the nose sections of hypersonic vehicles are blunt. This results in a curved bow shock around the vehicle with a variable entropy and temperature downstream. Since the boundary layer grows along the vehicle, it ingests the external inviscid flow, including the hot, high entropy gas that the near-normal shock portion produces. [1]

Due to the high velocity, many hypersonic flows are also characterized by a high Reynolds number $Re = \rho U L / \mu$ that exceeds the critical Reynolds number. Turbulence must therefore be taken into account. Turbulence increases the transport of momentum and energy, which results in a steeper temperature gradient in the boundary layer and, in turn, increases the heat flux towards the body.

Locally, shock waves impinging on the vehicle, e.g., near control surfaces, are sources of significant heating to the body, due to the associated temperature increase across the shock. Furthermore, the shock amplifies the turbulence, resulting in increased heat transfer towards the body [1, 5]. The structural damage to the X-15 hypersonic plane is a prominent example why accurate prediction of aerodynamic heating due to impinging shocks is crucial. A dummy engine was mounted underneath the vehicle during a test flight, which generated a shock wave that impinged on the mounting structure. The resulting heating exceeded expected values and nearly caused a loss of vehicle [6].

While the external flow affects the wall temperature significantly, the thermal state of the wall also affects the external flow. On a small scale, the temperature distribution in the boundary layer strongly depends on the thermal state of the wall. Since the wall-normal pressure gradient is negligible in boundary layers, the density is also directly affected. It has been shown that these small-scale effects also impact the structure of the external flow on a larger structure.
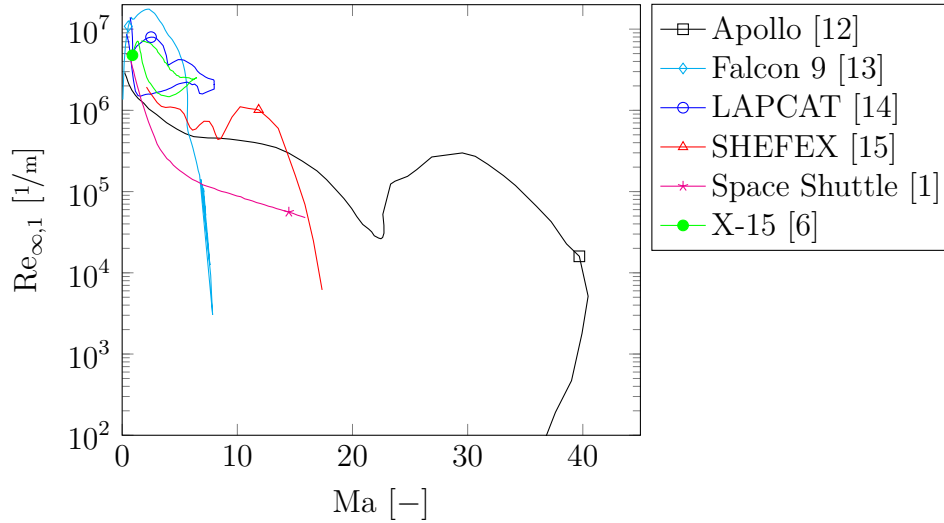
Figure 1.2: Flight envelope map for selected hypersonic flight programs

Brown et al. investigate separation at a laminar compression corner in hypersonic flow with theoretical triple-deck equations and numerical simulations [7]. They find that wall temperature affects separation bubble size, with a lower temperature moving the bubble further downstream. The results are confirmed by Exposito et al., who investigate wall temperature effects and nose bluntness for laminar separation on a blunted flat plate/compression corner [8]. They show that an increase of the ratio of wall temperature to stagnation temperature T_w/T_t results in an increase of the separation length. This may be connected to the thicker boundary layer at higher wall temperatures, which decreases the boundary layer stability. A similar effect is described by Brauckmann et al., who investigate the Space Shuttle trim anomaly experimentally and numerically [9]. They show that the effectiveness of the Space Shuttle flap increases with Reynolds number due to a thinner boundary layer, which increases the flap exposure to the external flow.

Based on these basic properties of aerodynamic heating in hypersonic flows, hypersonic flight programs from literature can be analyzed. Figure 1.2 shows the flight paths of some vehicles flying at hypersonic speeds in Mach number and unit Reynolds number space. The flight data was extracted from the given sources. Missing thermodynamic data was computed with the US 1976 standard atmosphere model [10], viscosity values were computed with Sutherland's model [11]. The most demanding, and therefore most relevant cases are the ones with high Mach numbers $Ma > 5$ and high unit Reynolds numbers $Re_1 > 10^6$. Based on figure 1.2, the most interesting conditions are LAPCAT and X-15. The X-15 was the first vehicle that achieved manned hypersonic flight in the atmosphere. LAPCAT was a research vehicle used to investigate the possibilities of hypersonic passenger flight, designed to cruise at $Ma = 8$ at an altitude of around $32\,km$. These are also especially interesting since they represent cases of civil hypersonic flight.

1.3 Numerical Treatment of Aerodynamic Heating

Historically, aerodynamic heating in hypersonic flows was computed using exact analytical solutions and empirical engineering relations. Methods with acceptable accuracy are available for the stagnation point heating, such as the one by Fay-Riddell [16]. Correlations for the heat flux distribution over the vehicle either require significant simplifications, or some numerical solution of the underlying governing equations [17]. When an estimation of the heating of more complicated vehicle shapes is required, these methods frequently fail to capture the underlying physics, and more complex methods must be used.

Another option for validating and testing hypersonic vehicles are experimental measurements. For high-enthalpy flows, shock tunnels and plasma wind tunnels are the most relevant test facilities. Shock tunnels may replicate velocity and Reynolds number of flight conditions, but are limited by very short measuring times in the order of milliseconds [18]. This reduces their usefulness for material heating experiments. Plasma wind tunnels on the other hand enable long experimental investigations in the order of minutes or hours and are able to reproduce the thermal state upstream of the vehicle in flight. However, they typically fail to reproduce the Mach and Reynolds numbers [19].

Flight tests allow an exact replication of the flight trajectory and its environmental conditions but due to their nature they are very expensive and time consuming. Instrumentation and reproducibility are additional challenges.

In this thesis, numerical fluid and fluid/structure interaction simulations are carried out. Compared to experiments and especially flight tests, they are a very cost-effective way of simulating hypersonic flight. Numerical simulations are also not limited by the operating conditions of experimental laboratories and can reproduce all parameters of any flight trajectory. Results of numerical simulations can also be reproduced exactly.

Numerical methods rely, however, on physical and chemical models and numerical methods to reproduce the physical behavior. For the success of a numerical simulation, it is crucial that the applied models and methods can represent the occurring physical phenomena properly. The thermal state of the wall in typical simulations of hypersonic flows, uses one of the following three assumptions:

- adiabatic wall: the wall-normal temperature gradient vanishes at the wall

- radiation-adiabatic wall: the conductive wall normal heat flux is in equilibrium with the divergent radiative heat flux

- cold isothermal wall: a constant wall temperature is set, usually walls are assumed cold $T_{\mathrm{W}} < T_{\mathrm{t},\infty}$

Neither of these represent the near-wall physics accurately. Using an adiabatic wall overpredicts the wall temperature significantly. The radiation-adiabatic assumption

improves this, but still neglects any heat flux towards the body. Both adiabatic results can be interpreted as the asymptotic result after an infinitely long flight of a vehicle with vanishing wall thickness.

Since the heat flux towards the body depends directly on the wall temperature, choosing an appropriate isothermal wall temperature is crucial. Along hypersonic vehicles in flight, the wall temperature can vary significantly, which makes choosing an appropriate wall temperature, or an appropriate wall temperature distribution difficult a priori. The assumption of a cold isothermal wall is usually only acceptable in short-duration experimental conditions, e.g, shock tunnels.

These basic thermal boundary conditions are insufficient because the aerodynamic heating of a body is inherently a coupled problem of the external fluid solution and the material heating response of the solid walls. This is referred to as the conjugate problem of convective heat transfer. The solution in the fluid and solid domains are computed in a coupled manner with an appropriate boundary condition between the two domains, which ensures conservation of energy.

Conjugate Heat Transfer (CHT) is routinely used in engineering domains, such as thermal treatment of materials, thermal processing of materials in industrial applications, design of heat exchangers, turbine blade cooling and more [20]. Numerical simulations of hypersonic vehicles often still rely on the thermal boundary conditions given above, but there are some examples in literature of CHT analysis for hypersonic flows.

Ferrero and D'Ambrosio employed a Finite-Volume Method (FVM) of the fluid and solid domains [21]. Coupling was achieved with a temperature boundary condition (Dirichlet) for the fluid and a heat flux condition for the solid (Neumann). They compared loose and tight coupling strategies to simulate the heating of some typical geometries for hypersonic applications. They found that the loose coupling may produce good agreement to experimental data, but is sensitive to the temperature threshold that is used to determine the coupling frequency.

Murty et al. conducted a CHT analysis of the heating process of multiple 2D vehicle shapes that consisted of multiple materials [22]. They used a commercial code with an iterative procedure to couple the two domains. Temperature-dependent solid material properties were used and have shown to impact the surface temperature distribution significantly.

Peetala used coupled and decoupled algorithms to study aerodynamic heating in hypersonic flow [23]. The investigated cases were 2D planar or axisymmetric and consisted of flat plates, cylinders, and a double wedge. The double wedge cases showed a noticeable variation of the separation bubble length with wall temperature between isothermal, adiabatic, and CHT cases.

Zhang et al. investigated the heating of a cylinder in $\mathrm{Ma}_\infty = 6.47$ flow [24]. They used the FVM for the fluid domain and the Finite-Element Method (FEM) for the solid region. The two domains were loosely coupled with a time-adaptive choice of the coupling intervals, which showed that the efficiency can be improved significantly by choosing the coupling frequency adaptively based on the temporal variation of the solid temperature.

Guo et al. [25] and Qin et al. [26] used a loosely coupled algorithm to investigate a spiked blunt body. They also used the FVM for the fluid and the FEM for the solid. Different geometries of the main body and the spike were simulated. The main finding was that the change in the temperature field with CHT walls also affected the pressure distribution. This resulted in about a 5% drag reduction with CHT.

Pogudalina et al. conducted a CHT analysis of a blunt steel sphere-cylinder with a copper sensor embedded in the stagnation region to determine the time lag of the sensor response during experiments [27]. The commercial solver Ansys Fluent was used, and no details were given about the coupling procedure. They experienced issues reproducing the experimental temperature signal since they neglected the thermal inertia of the sensor itself.

Reinert coupled a proprietary FEM thermal solver with the US3D fluid solver to investigate some more realistic geometries, including the HIFiRE and BOLT vehicles [28]. A loose coupling was used with non-coinciding meshes at the solid/fluid interface. The results show that the geometry of the vortex roll-up changes when CHT walls are used.

Zope et al. performed CHT simulations of a blunt cone over a flight trajectory with a loosely coupled algorithm [29]. Investigations include the coupling frequency of the solid/fluid interface and show significant efficiency gains by using a quasi-steady method, which may also decrease the accuracy of the solution when the coupling frequency is too low.

This overview of past investigations shows that CHT simulations are essential to accurately simulate vehicle temperatures in hypersonic flow. They also indicate that the structure of the flow away from the wall is influenced more strongly by the wall temperature than expected. For hypersonic flows this may mainly be due to the large difference between cold isothermal, adiabatic, and real CHT wall temperatures.

From the literature review it also appears that there is no consensus on the applied numerical methods for CHT simulations, since both FVM and FEM have been applied successfully. There is also a range of coupling techniques with different properties regarding efficiency and accuracy. The increased efficiency of loosely coupled methods may be outweighed by the loss of accuracy and the difficulty choosing an appropriate coupling frequency.

Most of the reviewed studies are limited to simple 2D and 2D axisymmetric problems with canonical geometries. There appears to be a lack of investigations of more complex and more realistic geometries.

1.4 Objectives and Outline

In this thesis, the development of an accurate method for CHT simulations is described. The method is intended to include all physical and chemical effects of heat transfer at the wall. A tightly coupled method is chosen since it offers the highest level of accuracy and algorithmic simplicity. The routines are implemented in the existing fluid dynamics code NSMB (Navier Stokes Multi Block). This removes the

need for interpolation of wall values between fluid and solid codes and produces the least amount of communication overhead.

The development focuses on applying and improving the physical and numerical methods to predict occurring effects accurately. Validation of the implementation is done with simple heat transfer and CHT problems. Investigations of hypersonic vehicle parts at operating conditions should give better insight into the heating in flight. Since it is important for mission planning, the analyses also show how the external flow and, therefore, the aerodynamic properties of a vehicle change when the wall temperature increases. Additionally, it is analyzed how local flow features, such as shock/boundary layer interaction, are affected by wall heating and the resulting change in boundary layer thickness.

This thesis is organized as follows: The basics of hypersonic flows and heat transfer are explained in chapter 2. Chapter 3 details the applied algorithmic and numerical methods. In chapter 4, the validation results of the implemented CHT method are shown. Chapter 5 shows results of CHT analysis of more realistic vehicle parts to analyze both the heating of the vehicle itself and the impact of the heated walls on the flow field. Finally, chapter 6 concludes this thesis and gives an overview of future research opportunities.

CHAPTER 2

Theory

The simulations in the following chapters are performed using Conjugate Heat Transfer analysis, which refers to the heat transfer between solid and fluids. Instances of conjugate heat transfer can be found in all applications, where a fluid is in contact with a solid. Some examples include:

- air-cooling of electrical components,

- internal cooling of turbine blades,

- aerodynamic heating in high-speed flow.

From a fluid mechanics point-of-view, conjugate heat transfer is relevant because some thermal boundary condition must be specified at solid walls. Typical choices are isothermal walls ($T_W = $ const) or adiabatic walls ($q_W = 0$), but real walls are usually neither isothermal nor adiabatic. Furthermore, engineers are often not interested in the flow around a part per se, but in the impact of the fluid on the part itself, e.g., the heating or cooling. With conjugate heat transfer simulations, wall temperatures and heating information are naturally available on the surface and inside the solid material.

There are generally three modes of heat transport: conduction, radiation, and convection. Conduction refers to the energy exchange between molecules through collisions and is relevant in any medium. Radiation describes the energy exchange via photons and can therefore even occur in vacuum and over long distances [30]. Convection refers to the energy transfer via motion of a medium. Even though it can also be understood as the combination of conduction and advection, it is usually listed as a mode of heat transfer due to its importance [31].

An illustration of conjugate heat transfer for hypersonic vehicles is shown in figure 2.1. At the interface between solid and fluid, four types of heat flux are in equilibrium: conduction in the fluid $q_{W,F}$, conduction in the solid $q_{W,S}$, radiation to/from the solid q_{rad}, and heat transport due to mass diffusion q_{diff}. The directions of the heat fluxes in figure 2.1 represent the typical processes in hypersonic flows. The hot surrounding fluid transfers heat to the colder solid body, while radiation transports energy away from the body and diffusion typically has a heating effect. The
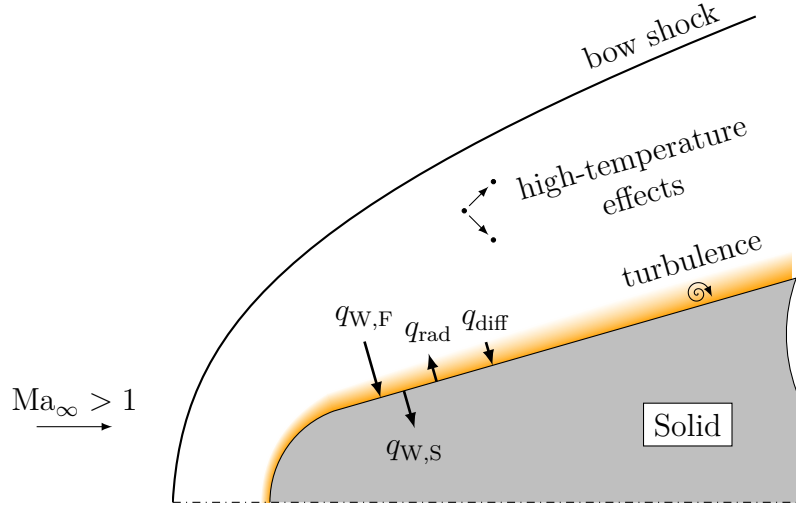
Figure 2.1: Conjugate heat transfer effects for hypersonic vehicles

figure also shows relevant physical and chemical processes that affect heat transfer in hypersonic flight: turbulence in the boundary layer and high-temperature effects behind the shock wave. In the following chapter, these effects are described in more detail.

The convective heat transfer to the wall can be divided into forced and natural convection. Natural convection occurs when the motion of the fluid is generated by density variations in a gravitational field, forced convection refers to processes where the motion of the fluid is caused by an external source. For the high-speed cases in this work, forced convection is expected to dominate [31] and gravity was neglected.

Due to the complexity of the problem, analytical solutions of conjugate heat transfer problems only exist for simple cases. Dorfman and Renner give an overview of analytical and numerical solutions of CHT problems [20]. For engineering applications, the convective heat flux is often computed using the heat transfer coefficient α:

$$q_{\text{convective}} = \alpha(T_{\text{W}} - T_{\infty}). \tag{2.1}$$

In non-dimensional form, the heat transfer can be expressed with the Nusselt number $\text{Nu} = \alpha L/\lambda$, which is a function of the Reynolds and Prandtl numbers. For simple cases, exact solutions of $\text{Nu} = f(\text{Re}, \text{Pr})$ can be found, more complex cases require empirical correlations that must be found experimentally or through numerical simulations [31]. In hypersonic flows, the aerodynamic heating of the gas requires more complex relations. The temperatures in the shock layer may be in the order of multiple thousand Kelvin, while the temperature of the wall is often significantly lower. Due to these large temperature variations, the density, and the laminar transport coefficients are not constant. The Nusselt number in hypersonic boundary layers is therefore also a function of the wall temperature $\text{Nu} = f(\text{Re}, \text{Pr}, T_{\text{W}})$ [32]. Finding engineering relations for that is difficult and conjugate heat transfer simulations are therefore required.

The heat flux at the solid/fluid interface is determined by the temperature gradient in the boundary layer, which is strongly affected by turbulence and the structure of the external flow. For an accurate representation of the heat transfer, an accurate representation of the turbulent boundary layer is therefore necessary. In section 2.3 an overview of turbulence modeling techniques is given, with an emphasis on the correct heat flux representation. Since the error of a numerical solution depends as much on the applied models as it does on their numerical implementation, an overview of the numerical methods is given in chapter 3.

2.1 Governing Equations

In the following section, the governing equations for the fluid and thermal solvers are presented. Note that the thermal response simulation is implemented in the same code, but because different solution methods are applied, the thermal solver is separately referenced here.

2.1.1 Fluid Solver

In the most general form, the motion of fluids can be described by the Boltzmann equation. It gives the statistical distribution of particles in six-dimensional position/momentum phase space. The solution of the Boltzmann equation is mathematically complex. Usually, stochastic methods such as the Direct Simulation Monte Carlo (DSMC) method are used. These methods, however, become exponentially more expensive for larger numbers of particles.

Most practical applications therefore use the Navier-Stokes equations instead. Based on the Chapman-Enskog theory [33], they represent a simplification of the Boltzmann equation that is valid for continuum flows, where the Knudsen number

$$\text{Kn} = \frac{\text{mean free path}}{\text{characteristic length}} \tag{2.2}$$

is much smaller than unity. A common threshold is $\text{Kn} < 0.03$ [2].

Technically, the term Navier-Stokes equations only refers to the conservation equations for momentum, but is commonly used for the set of conservation equations for mass, momentum, and energy. The Navier-Stokes equations are a system of nonlinear second-order partial differential equations that describe the motion of fluids [34]. Using tensor notation, the conservation of mass can be written as:

$$\frac{\partial}{\partial t}(\rho) + \frac{\partial}{\partial x_i}(\rho u_i) = 0, \tag{2.3}$$

the conservation equations for momentum are:

$$\frac{\partial}{\partial t}\left(\rho u_j\right) + \frac{\partial}{\partial x_i}\left(\rho u_i u_j + \delta_{ij} p\right) = \frac{\partial}{\partial x_i}\left(\tau_{ij}\right), \tag{2.4}$$

and the conservation of total energy is:

$$\frac{\partial}{\partial t}\left(\rho E\right) + \frac{\partial}{\partial x_i}\left(\rho u_i E + u_i p\right) = \frac{\partial}{\partial x_i}\left(u_j \tau_{ij}\right) - \frac{\partial}{\partial x_i}\left(q_i\right). \tag{2.5}$$

ρ is the fluid density, u_i are the velocity components, and p is the pressure. τ_{ij} refers to the components of the shear stress tensor and q_i are the components of the heat flux vector. E denotes the total energy per unit mass and is the sum of the internal energy and the kinetic energy:

$$E = e + e_{\text{kin}} = e + \frac{1}{2}u_i u_i. \tag{2.6}$$

δ_{ij} is the Kronecker delta, which is defined as:

$$\delta_{ij} = \begin{cases} 0 \text{ for } i \neq j, \\ 1 \text{ for } i = j. \end{cases} \tag{2.7}$$

Assuming the fluid is Newtonian, the shear stress tensor can be written as:

$$\tau_{ij} = \mu\left(\frac{\partial u_i}{\partial x_j} + \frac{\partial u_j}{\partial x_i}\right) + \delta_{ij}\zeta\frac{\partial u_k}{\partial x_k}, \tag{2.8}$$

$$= 2\mu\left(S_{ij} - \frac{1}{3}\frac{\partial u_i}{\partial x_j}\delta_{ij}\right) \tag{2.9}$$

where μ is the dynamic viscosity and S_{ij} is the strain rate tensor

$$S_{ij} = \frac{1}{2}\left(\frac{\partial u_i}{\partial x_j} + \frac{\partial u_j}{\partial x_i}\right). \tag{2.10}$$

For the bulk viscosity ζ, Stokes' hypothesis is used, which assumes $\zeta = -{}^2/_3\,\mu$. There is, however, some debate over the accuracy of this assumption [34].
The heat flux q_i can be modeled with Fourier's law, which postulates a linear relation between the heat flux vector and the temperature gradient:

$$q_i = -\lambda\frac{\partial T}{\partial x_i}, \tag{2.11}$$

where λ is the thermal conductivity.

2.1.2   Thermal Solver

The governing equation for the thermal solver is a simplification of the energy equation (2.5) for a medium at rest $u_i = 0$ and at constant pressure $p = \text{const}$:

$$\frac{\partial}{\partial t}\left(\rho E\right) = -\frac{\partial}{\partial x_i}\left(q_i\right) \tag{2.12}$$

For a non-moving body with constant specific heat capacity c, the total energy is

$$E = e + \underbrace{e_{\text{kin}}}_{=0} = cT. \tag{2.13}$$

With the definition of the thermal diffusivity $a = \lambda/(\rho c)$, the heat equation in three dimensions follows:

$$\frac{\partial T}{\partial t} - a\frac{\partial^2 T}{\partial x_i^2} = 0. \tag{2.14}$$

Equation (2.14) is only valid for materials with constant thermal conductivity and density. The more general energy equation (2.12) was therefore implemented, which requires the computation of the temperature from the energy after each timestep.

2.2 Fluid and Thermal Properties

2.2.1 Thermodynamic Closure

The five Navier-Stokes equations (2.3) to (2.5) contain seven unknowns: ρ, p, T, u_i, e. Two additional equations are therefore required to close the system of equations. In principle, closure could be achieved by two relations between any of the seven unknowns. For application in fluid dynamics, the equations are closed using a thermal equation of state and a caloric equation of state. For an ideal gas the thermal equation of state is

$$p = \rho R T, \tag{2.15}$$

where $R = \mathscr{R}/M$ is the specific gas constant. The heat capacity is constant for a perfect gas and the caloric equation of state is

$$e = c_v T, \tag{2.16}$$

with the specific heat capacity at constant specific volume c_v.

The assumption of a calorically perfect gas is only valid at moderate temperatures up to about $T \approx 500\,\text{K}$ [1]. The hypersonic flow conditions investigated in this work, often lie outside this temperature range. The assumption of a calorically perfect breaks down due to two processes: the excitation of additional vibrational and electronic degrees of freedom and chemical reactions. These high-temperature effects are also sometimes referred to as real-gas effects. Real-gas effects, however, more accurately refer to effects of non-vanishing intermolecular forces, such as Van-der-Waals forces, which require a different thermal equation of state.

The investigations in this work are limited to air as the fluid, the following explanations are therefore limited to monatomic and diatomic gases. Each atom is assumed to be a point mass, resulting in vanishing moments of inertia. The atoms in molecules are connected with atomic bonds that are massless, but due to distance between the atoms, some moments of inertia are non-zero.

Figure 2.2 shows the degrees of freedom of monatomic and diatomic gases. Due to the vanishing moments of inertia, monatomic gases only exhibit translational degrees

a) monatomic gas   **b)** diatomic gas
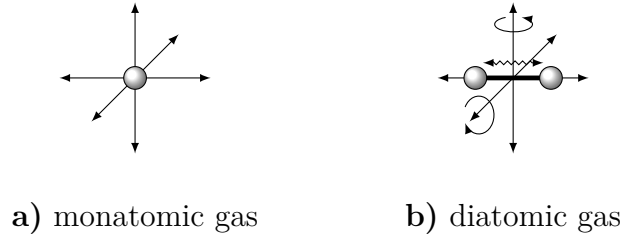
Figure 2.2: Internal degrees of freedom of atoms and molecules

of freedom, which means all internal energy is stored in linear motion along the three spacial axes. The ratio of specific heats is connected to the number of degrees of freedom f as:

$$\gamma = \frac{f+2}{f}, \tag{2.17}$$

which results in $\gamma_{\mathrm{monatomic}} = {}^{5}\!/_{3} = 1.\overline{6}$. Diatomic molecules can also store internal energy in two rotational degrees of freedom. Additionally, there are two vibrational degrees of freedom, because thermal energy is stored as kinetic and potential energy of the vibration. At moderate temperatures, translational and rotational degrees of freedom are fully excited, which gives $\gamma_{\mathrm{diatomic}} = {}^{7}\!/_{5} = 1.4$. At temperatures above $500\,\mathrm{K}$, vibrational excitation becomes relevant, increasing the degrees of freedom to seven and $\gamma_{\mathrm{diatomic},T\to\infty} = {}^{9}\!/_{7} = 1.\overline{285714}$. [2]

When more energy is transferred to a molecule AB by a partner M than its atomic bond can hold, the molecule dissociates:

$$\mathrm{AB + M} \rightleftharpoons \mathrm{A + B + M}. \tag{2.18}$$

For air, this process is relevant for the oxygen O_2, nitrogen N_2, and nitric oxide NO molecules. The partner molecule M can be any of the other particles in the gas. It does not participate in the reaction and is only required for the transfer of energy. The forward reaction, i.e., the dissociation of a molecule into atoms is endothermic. The energy required for endothermic reactions is removed from the surrounding medium, which decreases the temperature.

As the number of particles (atoms + molecules) changes due to dissociation and recombination, the molar mass of the mixture M_{mix} and the specific gas constant of the mixture R_{mix} change. The relevant conditions for the simulations in this study do not warrant the inclusion of actual real-gas effects (intermolecular forces), so the fluid can be treated as a mixture of thermally perfect gases:

$$p = \rho R_{\mathrm{mix}} T \tag{2.19}$$

$$e = \sum_s Y_s e_s(T). \tag{2.20}$$

$Y_s = {}^{\rho_s}\!/_{\rho}$ refers to the mass fraction of species s.

Any thermodynamic system will strive to minimize its Gibbs free energy, which is defined as

$$g = e + \underbrace{\frac{p}{\rho}}_{h} - Ts. \tag{2.21}$$

The system is in equilibrium when g is minimal. When the system is subject to changes in the environmental conditions, it adjusts accordingly to reach equilibrium again. This process is known as Le Chatelier's principle [35]. Given enough time, any system will reach its equilibrium state, during this time, it is in non-equilibrium. The Damköhler number allows for the distinction between multiple regimes:

$$\mathrm{Da} = \frac{T_{\text{flow}}}{T_{\text{reaction}}} = \frac{k_{\text{reaction}}}{k_{\text{flow}}} = \frac{k_{\text{reaction}}L}{u_{\text{flow}}} \begin{cases} = 0 \text{ in frozen conditions} \\ \approx 1 \text{ in non-equilibrium} \\ \to \infty \text{ in equilibrium} \end{cases} \tag{2.22}$$

where k_{reaction} is the reaction rate and k_{flow} is the characteristic temporal rate of the flow. T_{reaction} and T_{flow} are the respective timescales.

When $\mathrm{Da} = 0$, the reaction is slow compared to the flow and the composition is constant. When $\mathrm{Da} \approx 1$, the timescale of the reaction is similar to the timescale of the flow, the fluid is in non-equilibrium. The thermodynamic state therefore depends on the environmental conditions and the time. The evolution of the composition is described by a set of additional mass conservation equations for the species s:

$$\frac{\partial \rho Y_s}{\partial t} + \frac{\partial}{\partial x_i}(\rho Y_s u_i) + \frac{\partial}{\partial x_i}\left(-\rho D_{s,\text{mix}}\frac{\partial Y_s}{\partial x_i}\right) = S_s, \tag{2.23}$$

where $D_{s,\text{mix}}$ is the diffusion coefficient of species s in the mixture and S_s the respective source term. The source term can be written as

$$S_s = M_s \sum_m \nu_s^m \left[k_{\text{f},m} \prod_{s,\text{reactants}} \left(\frac{\rho Y_s}{M_s}\right)^{-\nu_s^m} - k_{\text{b},m} \prod_{s,\text{products}} \left(\frac{\rho Y_s}{M_s}\right)^{\nu_s^m} \right], \tag{2.24}$$

where ν_s^m is the stoichiometric coefficient of species s in reaction m, note that the coefficients of reactants are negative. $k_{\text{f},m}$ and $k_{\text{b},m}$ are the forward and backward reaction rate coefficients of reaction m, which can, e.g., be computed with Arrhenius relations.

Simulations with chemical non-equilibrium are numerically more expensive because they require the solution of one additional transport equation for each participating species. Additionally, some reaction rates in the source terms are typically large, which makes the species conservation equations numerically stiff and limits the maximum timestep size [2]. In addition to chemical non-equilibrium, gases can also be in thermal non-equilibrium when the internal energy is not distributed equally between the degrees of freedom. Because the timescale to reach thermal equilibrium is much smaller than for chemical equilibrium, at altitudes below 60 km it is justified to assume thermal equilibrium [2, 36].

When Da $\to \infty$ chemical reactions are significantly faster than the flow processes and the fluid can be assumed to be in equilibrium at every point. In equilibrium the thermodynamic state of the fluid can be defined using any two independent thermodynamic state variables, e.g., density and internal energy, or pressure and temperature [2]. The validity of the equilibrium assumption is limited to regions without large mean flow gradients where the characteristic length L is large. For the investigated hypersonic flows at moderate Mach numbers, the assumption is sufficiently accurate except in the direct vicinity of strong shock waves [36].

Because the equilibrium composition is uniquely defined by two thermodynamic state variables, it can be computed efficiently. One option is to use tabulated data that is interpolated during the simulation, e.g., [37]. The computation is fast and no knowledge of the chemical processes is needed, but it requires extensive datasets in the two-dimensional space of thermodynamic input variables. The equilibrium composition can also be computed from tabulated equilibrium constants for the individual dissociation reactions, which are functions of temperature. For a chemical reaction m

$$\nu_1 A_1 + \nu_2 A_2 + ... = ... + \nu_{N_s-1} A_{N_s-1} + \nu_{N_s} A_{N_s} \tag{2.25}$$

with the participating species s and stoichiometric coefficients ν_s^m, the equilibrium constant based on concentrations $C_s = {n_s}/{V} = {\rho Y_s}/{M_s}$ can be written as

$$K_{m,C}(T) = \prod_s C_s^{\nu_s^m}. \tag{2.26}$$

Note that the stoichiometric coefficients of reactants, again, are negative. The simulations in this work were conducted using the data by Park [38], which uses forth-order polynomials:

$$K_C(T) = \exp\left(a_1 + a_2 Z + a_3 Z^2 + a_4 Z^3 + a_5 Z^4\right) \tag{2.27}$$

with $Z = {10\,000\,\mathrm{K}}/{T}$. This gives one equation for each of the dissociation reactions. Two conservation equations for the mass fractions of O and N atoms close the system of equations. Based on the mass fractions, the internal energy can be computed:

$$e = \sum_s Y_s h_s(T) - \frac{p}{\rho}. \tag{2.28}$$

With the specific enthalpy of species s

$$h_s = c_{p,s} T + e_s^{\mathrm{vib}} + h_{f,s}^0, \tag{2.29}$$

where the vibrational energies e_s^{vib} vanish for atoms and the heat of formation is zero for O_2 and N_2. Due to the dependence of the equilibrium constant on the temperature, the equilibrium state must be found iteratively. This method is computationally more expensive and requires knowledge of the underlying physics. However, the required datasets are simpler and smaller, since one polynomial expression for the equilibrium constant for each reaction is sufficient.

The importance of high-temperature effects for hypersonic flows can be appreciated from a small example. The stagnation point temperature in air as a calorically perfect gas for a vehicle flying at Ma = 7 at an altitude of 30 km would be

$T_{\text{stag}} = 2447\,\text{K}$. For the same condition, the equilibrium condition using Parks equilibrium constants described above is $T_{\text{stag}} = 2162\,\text{K}$. In some cases, this reduction of the surface temperature in equilibrium flows compared to perfect gases is what makes hypersonic flight possible in the first place, since it relaxes the requirements regarding the heat-resistance of the vehicle.

2.2.2 Transport Coefficients

For reacting hypersonic flows, viscosity, thermal conductivity and the species diffusion coefficients are relevant. The simplest approximation for the transport coefficients is a constant value. Since these viscous processes are temperature dependent, this assumption breaks down for high-speed flows, where the temperature varies significantly in the flow field. For the viscosity μ, Sutherland's model can be used instead [11], which gives the viscosity of a gas as a function of temperature.

Since the viscosity function of each gas is different, the viscosity of a mixture is affected by its composition. For reacting hypersonic flows, Sutherland's model loses its validity in regions where the gas composition changes significantly. Equilibrium gases can therefore be treated by more complex models that take the composition into account, such as Blottner's model [39]. The viscosity of each participating species can be computed as a function of temperature. Based on the species mass fractions, the mixture viscosity can then be found. Alternatively, the transport properties of equilibrium gases can be calculated from tabulated values.

The thermal conductivity λ can be calculated assuming a constant Prandtl number $\text{Pr} = {c_p \mu}/{\lambda}$ and the diffusion coefficient D from a constant Lewis number, which for this thesis is defined as $\text{Le} = {D c_p \rho}/{\lambda}$ in accordance with [1, 2, 20], even tough the reciprocal definition can be found in literature as well [30, 31].

2.2.3 High-Temperature Material Properties

Due to the high heating rates of high-speed flows, surface temperatures of vehicles in such conditions can increase dramatically from the ambient temperature. While constant material properties, such as thermal conductivity and thermal diffusivity, are acceptable for many applications, they can be a significant source of error for high-speed cases. An extensive overview of the material properties of many alloys can be found in Touloukian et al. [40] and in [41]. Material properties are typically determined experimentally and are therefore only available at discrete temperatures. A polynomial fit can be used to get continuous functions of literature data for the thermal diffusivity, heat capacity, and thermal conductivity.

For a property ϕ, where discrete values $\phi_i = \phi(T_i)$ can be found in literature, a polynomial fit of the type

$$\phi(T) = \sum_{k=0}^{N} a_k T^k \tag{2.30}$$

is sought. The method of least-squares is used to find the coefficients a_k for a given set of input values ϕ_i. A detailed description is given by Bevington et al. [42]. The

chosen order of the polynomial should match the input data, because the fit lacks
resolution when the order is too low, and it oscillates when the order is too high.
Fifth-order polynomials with six coefficients were used in the present work.

2.3   Turbulence Modeling

As stated in chapter 1, turbulence must be accounted for in many hypersonic flows.
The transition from laminar flow to turbulence is not part of this thesis, all flows are
treated as fully laminar or fully turbulent.

2.3.1   The Nature of Turbulence

Turbulence has a large impact on the properties of the flow and is therefore important
for aerodynamics. It is characterized by chaotic, unsteady small-scale fluctuations
superimposed on the large-scale motion of the fluid. Since the motion of turbulent
flows in the continuous regime is described exactly by the Navier-Stokes equations,
the small-scale fluctuations are not *random*, but their motion appears *chaotic* due to
the nonlinearity of the governing equations. Compared to laminar flow, where stream-
lines are smooth and parallel, streamlines in turbulent flows show three-dimensional
fluctuations. [43]

Whether a flow is in the laminar or turbulent regime, is determined by the
Reynolds number

$$\text{Re} = \frac{\rho U L}{\mu} = \frac{\text{inertial forces}}{\text{viscous forces}}. \tag{2.31}$$

For any type of flow, a critical Reynolds number Re_{crit} can be found, so that the flow
is turbulent for $\text{Re} > \text{Re}_{\text{crit}}$. The choice of the characteristic length L depends on the
type of problem.

Turbulent fluctuations increase the transport of momentum and energy. While
momentum in laminar shear layers is only transported laterally via viscous effects,
slower fluid elements are mixed with faster fluid elements due to their fluctuations
when the flow is turbulent. This small scale mixing results in large scale transport of
mean momentum [44]. Similarly, turbulence also affects the transport of energy and
species concentrations, which makes it very important in combustion processes.

The increased momentum transport changes the boundary layer velocity profile,
which become steeper near the wall. This results in higher skin friction compared to
laminar flows [45]. It also makes turbulent boundary layers more resistant against
separation, and if separation occurs, the separation length is shorter [46]. Similarly,
the increased energy transport in the boundary layer results in a steeper tempera-
ture gradient at the wall, which increases the wall heat load [46]. This is especially
important for the investigated hypersonic flows, where wall heat load is often the
major design limitation. Turbulence remains one of the unsolved problems in com-
putational fluid dynamics because so far no universal model has been found that
accurately describes the turbulent motion in all cases.

One of the major characteristics of turbulence is the existence of a large range of length scales. Energy is introduced into the largest eddies as macroscopic unsteadiness and is then transferred to successively smaller eddies until it dissipates at the smallest scales. It is the large scales that contain the majority of the kinetic energy, however their properties are also very problem-dependent. The motion of the small scales, on the other hand, is universal, it does not depend on the problem setup. [43]

2.3.2 High-Order Modeling Approaches

As stated above, turbulence is described by the Navier-Stokes equations, and it can therefore be simulated without the need for any models. This approach is referred to as Direct Numerical Simulation (DNS). To accurately capture the turbulent flow, all relevant length scales must be resolved. The characteristic length of the smallest turbulent scales is

$$\eta = \left(\frac{\nu^3}{\epsilon}\right)^{\frac{1}{4}} \tag{2.32}$$

which is referred to as Kolmogorov length scale [43]. ϵ is the dissipation rate of turbulence kinetic energy. An important observation is the scaling of the Kolmogorov length scale with the Reynolds number [43]:

$$\frac{L}{\eta} \sim \text{Re}^{\frac{3}{4}}. \tag{2.33}$$

To resolve all turbulent eddies, a grid with $\Delta x \approx \eta$ is required. The number of cells to accurately capture all turbulent scales in one spacial direction is $N \propto L/\eta \sim \text{Re}^{3/4}$ Due to stability limits of the applied numerical algorithm (Courant-Friedrichs-Lewy condition) the maximum timestep is

$$\Delta t_{\max} \propto \frac{\Delta x}{U} \tag{2.34}$$

So, the number of timesteps required to simulate the relevant macroscopic time t_{sim} is

$$N_t = \frac{t_{\text{sim}}}{\Delta t_{\max}} \propto \frac{t_{\text{sim}} U}{\Delta x} \propto \frac{LU}{U \Delta x} = \frac{L}{\Delta x} \sim \text{Re}^{\frac{3}{4}}. \tag{2.35}$$

The total computational effort therefore scales with $N^3 N_t \sim \text{Re}^3$. For problems with technical relevance, where Re is typically large, this becomes prohibitively expensive.

The computational effort is lower for a Large Eddy Simulation (LES). Based on the observation that small turbulent scales are universal, i.e., they do not depend on the external geometry, it seems reasonable that a turbulence model that only treats the smallest scales could perform well. For that, the field variables are filtered over the cell volume, which is mathematically expressed as a convolution with the filter kernel G [43]:

$$\hat{\phi}(\boldsymbol{x}) = \int_V G(\boldsymbol{\xi} - \boldsymbol{x}) \phi(\boldsymbol{x}) \, d\boldsymbol{\xi}. \tag{2.36}$$

This results in a decomposition of the field variables into the filtered part and a high-frequency component $\phi = \hat{\phi} + \phi'''$. By first inserting the decomposed field variables into the Navier-Stokes equations (2.3) to (2.5) and then applying the filtering operation to the resulting equations, the governing equations for the large scale motion are derived.

Since the filtering operation cannot be inverted, the filtered LES equations contain unclosed terms [47]. Closure is achieved by means of a subgrid scale model, which relates the unknown terms to known filtered quantities. As the smallest scales are now treated by the subgrid scale model, the grid requirements are relaxed compared to DNS. This allows LES simulations of more realistic problems. It retains the fundamental unsteadiness and three-dimensionality of the large scales and only applies the model to the small universal scales that can more easily be represented by a model. However, LES simulations of real-world problems are still very computationally expensive as they still require a time-accurate three-dimensional solution. Solutions to engineering problems are often found in an iterative process, which necessitates faster simulation methods. Furthermore, integrated, time-averaged quantities such as lift and drag are often more relevant than transient solutions of the entire turbulent field.

2.3.3   RANS Turbulence Modeling

Due to the inherent unsteadiness, steady state solutions of turbulent flows do not exist. It is therefore useful to apply a statistical description of turbulent flows, since the time average of many problems reaches a steady state. The Reynolds-Averaged Navier-Stokes (RANS) approach is therefore often a natural fit and was used for the turbulent simulations in this thesis. Similarly to the LES decomposition, the Reynolds averaging is defined as

$$\overline{\phi} = \lim_{\tau \to \infty} \frac{1}{\tau} \int_{t_0}^{t_0+\tau} \phi \, \mathrm{d}t. \tag{2.37}$$

This allows the decomposition of a field variable into a mean and a fluctuating part: $\phi = \overline{\phi} + \phi'$. While LES and RANS equations are structurally similar, they are conceptually different: LES represents a filter in space, while RANS represents an average in time. Based on that, the density-weighted Favre-average $\tilde{\phi}$ is defined:

$$\tilde{\phi} = \frac{\overline{\rho\phi}}{\overline{\rho}}, \tag{2.38}$$

with the decomposition $\phi = \tilde{\phi} + \phi''$. By inserting the decomposition into the Navier-Stokes equations (2.3) to (2.5) and averaging the resulting equations, the RANS equations can be derived. In practice, for compressible flows a combination of Reynolds averaging for the density and pressure, and Favre averaging for the velocity and energy is used, which results in the smallest number of unclosed terms. The following set of conservation equations for mean mass, mean momentum, and mean energy are obtained [48]:

$$\frac{\partial}{\partial t}\overline{\rho} + \frac{\partial}{\partial x_i}\overline{\rho}\tilde{u}_i = 0 \tag{2.39}$$

$$\frac{\partial}{\partial t}\overline{\rho}\tilde{u}_j + \frac{\partial}{\partial x_i}\left(\overline{\rho}\tilde{u}_i\tilde{u}_j + \delta_{ij}\overline{p}\right) = \frac{\partial}{\partial x_i}\left(\overline{\tau}_{ji} - \overline{\rho u_j'' u_i''}\right) \tag{2.40}$$

$$\frac{\partial}{\partial t}\overline{\rho}\tilde{E} + \frac{\partial}{\partial x_i}\tilde{u}_i(\overline{\rho}\tilde{E} + \overline{p}) = \frac{\partial}{\partial x_i}\left(\tilde{u}_k\overline{\tau}_{ki} - q_i - \underbrace{\overline{\rho u_i'' h''}}_{A} - \underbrace{\tilde{u}_k\overline{\rho u_i'' u_k''}}_{B} - \underbrace{\overline{\tau_{ik} u_k''}}_{C} - \underbrace{\overline{\rho u_i'' 1/2 u_k'' u_k''}}_{D}\right) \tag{2.41}$$

Note that the mean total energy contains the turbulence kinetic energy (TKE) $k = 1/2\overline{u_i'' u_i''}$:

$$\tilde{E} = \tilde{e} + \frac{\tilde{u}_i\tilde{u}_i}{2} + \frac{\overline{u_i'' u_i''}}{2}. \tag{2.42}$$

While the Favre-averaged continuity equation (2.39) is structurally identical to the continuity equation of the Navier-Stokes equations (2.3), the momentum and energy equations contain unclosed terms. These arise because information is lost in the averaging procedure, similar to how filtering in the LES framework is non-reversible. The term $\overline{\rho u_i'' u_j''}$ is the Reynolds Stress Tensor (RST) based on the observation that its structure is similar to the laminar shear stress tensor. With similar phenomenological argumentation, the four terms in the viscous energy flux on the RHS of eq. (2.41) are referred to as turbulent heat flux (A), turbulent work (B), molecular diffusion of turbulence (C), and turbulent transport of TKE (D) [48]. Note that the mean molecular shear stress tensor $\overline{\tau}_{ij}$ also contains unclosed terms, which are usually approximated as:

$$\overline{\tau}_{ij} = \overline{\mu\left(\frac{\partial u_i}{\partial x_j} + \frac{\partial u_j}{\partial x_i}\right) + \delta_{ij}\zeta\frac{\partial u_k}{\partial x_k}}, \tag{2.43}$$

$$\approx 2\overline{\mu}\left(\tilde{S}_{ij} - \frac{1}{3}\frac{\partial\tilde{u}_i}{\partial x_j}\delta_{ij}\right), \tag{2.44}$$

where $\tilde{S}_{ij}$ is the Favre-averaged mean strain rate tensor.

Closure for the Reynolds Stress Tensor

The RANS equations (2.39) to (2.41) are exact extensions of the Navier-Stokes equations for all cases where a decomposition of the field variables into a mean (constant) and a fluctuating part is allowed, i.e., all cases without mean flow unsteadiness. This constraint can be relaxed under the condition that the timescale of turbulence τ is much smaller than the timescale of the mean flow, which allows for slow mean flow unsteadiness. This approach is referred to as Unsteady RANS (URANS) and is often used in practical applications, even though it lacks a rigorous separation of turbulent and mean flow timescales [48]. Since the equations cannot be closed purely with

mathematical operations, additional assumptions must be made. The most common assumption is the Boussinesq hypothesis which linearly relates the turbulent stresses to the mean strain rate [44, 48]:

$$\overline{-\rho u_i'' u_j''} = 2\mu_{\mathrm{T}} \left(\tilde{S}_{ij} - \frac{1}{3} \frac{\partial \tilde{u}_k}{\partial x_k} \delta_{ij} \right) - \frac{2}{3} \overline{\rho} k \delta_{ij}. \tag{2.45}$$

Models that use this assumption are referred to as (linear) Eddy Viscosity Models (EVM).

The assumption stems from a phenomenological observation rather than a mathematical derivation. Molecular transport of momentum, i.e., viscous shear stress is a result of the microscopic random molecular motion in fluids that mixes fluid elements with different momentum in shear layers [48]. If turbulence is understood as a macroscopic random motion of fluid elements, an analogy to viscous stresses can be made, and the Reynolds stress tensor is therefore modeled closely after its laminar counterpart, see eq. (2.9).

Algebraic Models:
In the simplest form of RANS models, the eddy viscosity is directly related to the mean flow. The relation can more intuitively be defined by the mixing length proposed by Prandtl, which can be understood as the characteristic size of the eddies. Well known examples of algebraic models include the Cebeci-Smith model [49] and the Baldwin-Lomax model [50]. Universally accurate relations for the mixing length, however, most likely will not be found.

One-Equation Models:
For one-equation models, as the name suggests, one additional transport equation for a turbulent variable is introduced. The most popular of these models is the Spalart-Allmaras model [51], which solves a transport equation for the parameter $\tilde{\nu}$, from which the eddy viscosity follows as $\mu_{\mathrm{T}} = \overline{\rho} \tilde{\nu} f_{v1}$, with the damping function f_{v1}. The variable $\tilde{\nu}$ does not have physical relevance, so the transport equation is constructed from empiricism. Since the eddy viscosity is not a locally defined quantity, the model includes history effects that describe the evolution of turbulence along streamlines.

Two-Equation Models:
Defining a turbulent eddy with one parameter is inevitably incomplete, even in isotropic turbulence. For two-equation models, two additional transport equations are therefore added, which allows to fully characterize isotropic eddies, e.g., with a length and time-scale. Typically, equations for the turbulence kinetic energy k and the dissipation rate ϵ, specific dissipation rate ω, or timescale τ are solved. The eddy viscosity can then be found from $\mu_T \sim \overline{\rho} k^2/\epsilon \sim \overline{\rho} k/\omega \sim \overline{\rho} k\tau$. The exact transport equation for the turbulence kinetic energy can be derived from the RANS equations: [48]

$$\begin{aligned}
\frac{\partial}{\partial t}(\overline{\rho} k) + \frac{\partial}{\partial x_i}(\overline{\rho} \tilde{u}_i k) = &-\overline{\rho u_i'' u_j''} \frac{\partial \tilde{u}_i}{\partial x_j} - \overline{\rho} \epsilon + \frac{\partial}{\partial x_j} \left(\overline{\tau_{ji} u_i''} - \overline{\rho u_j'' 1/2 u_i'' u_i''} - \overline{p' u_j''} \right) \\
&- \overline{u_i''} \frac{\partial \overline{p}}{\partial x_i} + \overline{p' \frac{\partial u_i''}{\partial x_i}}
\end{aligned} \tag{2.46}$$

The terms on the right-hand side are production, dissipation, molecular diffusion, turbulent transport, pressure diffusion, pressure work, and pressure dilatation [48]. Given a relation for the RST, the production term can be computed directly. The dissipation term is usually closed using the second transported turbulent property, in case of the $k - \omega$ model, $\epsilon = \frac{9}{100}\overline{\rho}k\omega$ with the transport equation [48]:

$$
\begin{aligned}
\frac{\partial}{\partial t}(\overline{\rho}\omega) + \frac{\partial}{\partial x_i}(\overline{\rho}\tilde{u}_i\omega) = &-\alpha\frac{\omega}{k}\overline{\rho u_i'' u_j''}\frac{\partial \tilde{u}_i}{x_j} - \beta\overline{\rho}\omega^2 + \sigma_d\frac{\overline{\rho}}{\omega}\frac{\partial k}{\partial x_i}\frac{\partial \omega}{\partial x_i} \\
&+ \frac{\partial}{\partial x_i}\left[\left(\mu + \sigma\frac{\overline{\rho}k}{\omega}\right)\frac{\partial \omega}{\partial x_i}\right].
\end{aligned}
$$ (2.47)

This equation contains multiple closure coefficients, see [48] for details. Similar transport equations are the foundation for the $k - \epsilon$ [52] and $k - \tau$ [53] frameworks.

The remaining terms of eq. (2.46) all describe some type of viscous or turbulent transport and are thus typically closed using a gradient diffusion type term proportional to the Laplace operator of the TKE: $\propto \partial^2 k/\partial x_i^2$ [48].

One of the main problems with the Boussinesq hypothesis is that it characterizes turbulence with the scalar quantity μ_T, while in reality the Reynolds stress tensor has six independent components (since it is symmetric) without any a-priori relation between them. In some cases, the magnitude of the turbulent fluctuations (TKE) may be correct, but the alignment of the Reynolds stresses is not. In the Boussinesq assumption, for example, the mean anisotropy of the Reynolds stresses

$$
a_{ij} = \frac{\overline{\rho u_i'' u_j''}}{2\overline{\rho}k} - \frac{1}{3}\delta_{ij}
$$ (2.48)

is directly proportional to the mean strain rate. Experiments show that this results in fundamentally incorrect behavior in cases where geometrically induced mean strain is instantaneously removed [44, 54]. While molecular viscosity is a local fluid property, which only depends on the current state of the fluid, e.g., its temperature, the turbulent viscosity depends also on the flow history [48]. Despite its deficiencies, many RANS turbulence models use the Boussinesq assumption and produce acceptable results for a large range of flow types.

The simplest extension of the Boussinesq assumption is to replace the linear relation between the Reynolds stresses and the strain rate with a non-linear relation. Abe et al. compute the Reynolds stresses from a non-linear function of the mean strain rate and mean vorticity

$$
\Omega_{ij} = \frac{1}{2}\left(\frac{\partial \tilde{u}_i}{\partial x_j} - \frac{\partial \tilde{u}_j}{\partial x_i}\right),
$$ (2.49)

which includes terms up to the second order [55]. These higher-order correlations give more degrees of freedom but require more closure coefficients. Since the non-linear relations are not necessarily based on physical reasoning, careful calibration is required. Explicit Algebraic Reynolds Stress Models (EARSM), such as the model

by Wallin and Johansson [56] find similar non-linear relations for the RSM based on simplifications of the Reynolds Stress transport equations.

Reynolds Stress Models:
A natural extension of the problem is the addition of stress transport equations, which are derived from the Navier-Stokes equations and describe the evolution of the Reynolds stresses exactly. The exact form of the equations is for example given in [48]. The stress transport equations are six independent equations for the six unique components of the Reynolds stress tensor. Due to the way they are derived, Reynolds stress models are often referred to as second-moment closure models. Examples of Reynolds stress models include the Speziale-Sarkar-Gatski model [57] and the Launder-Reece-Rodi model [58].

By using the exact transport equation for the RST, all turbulent effects are naturally included in the simulation. Unfortunately, the equations also contain more unclosed terms including more complex triple correlations, see Wilcox [48] for more details. Obtaining closure approximations for these higher-order terms is non-trivial because phenomenological analogies are difficult to find. Reynolds stress models also require the solution of six additional transport equations for the RST, which must be accompanied by a scale-determining equation, such as ϵ or ω, so the additional computational effort is significant. Furthermore, the coupling between the Reynolds stress equations and the mean flow equations can impact the numerical stability [44].

Closure for the Turbulent Heat Flux

The closure for the turbulent heat flux $\overline{\rho u_i'' h''}$ is, similar to the closure for the RST, based on phenomenological observations. Analogous to how the turbulent eddies increase momentum transfer, they also increase energy transfer. The Reynolds analogy [59] then forms the basis of the most widely used closure method. It states that momentum and energy transport are alike. Similar to the turbulent momentum transport, which is proportional to the mean velocity gradient, the turbulent heat flux is proportional to the mean energy, or temperature, gradient. This is correct in laminar flows and the proportionality is assumed to hold in turbulent flows as well. From this assumption follows the gradient diffusion hypothesis which states that the scalar flux vector is proportional to the mean scalar gradient [44].

The models that apply this assumption are referred to as Eddy Diffusivity Models (EDMs) and use the following relation for the turbulent heat flux:

$$\overline{\rho u_i'' h''} = -\lambda_\mathrm{T} \frac{\partial \tilde{T}}{\partial x_i}. \tag{2.50}$$

The proportionality parameter λ_T is the eddy diffusivity and is usually related to the eddy viscosity with the turbulent Prandtl number

$$\mathrm{Pr_T} = \frac{\mu_\mathrm{T} c_p}{\lambda_\mathrm{T}}. \tag{2.51}$$

The turbulent Prandtl number is in the order of unity in many flows [60], but can also differ significantly [61]. Nevertheless, most CFD codes frequently apply a constant

turbulent Prandtl number: $\mathrm{Pr_T} = \mathrm{const.} = 0.9$. Species diffusion processes are described by a similar term that can be closed using a constant turbulent Schmidt number $\mathrm{Sc_T} = \mu_\mathrm{T}/\rho D_\mathrm{T}$.

The eddy diffusivity approach can easily be implemented in existing CFD codes by replacing the molecular conductivity by the total conductivity $\lambda = \lambda_\mathrm{viscous} + \lambda_\mathrm{T}$. However, due to the simplicity of the EDM approach, some problems arise. Firstly, the assumption that mean scalar gradient and flux vector are aligned is often not correct. See for example the measurements by Tavoularis and Corrosin [62], where the measured turbulent heat flux was strongly misaligned with the mean temperature gradient. Similarly, observations of turbulent heat flux in the direction of the mean temperature gradient, referred to as countergradient heat flux, can be found in Schumann [63] and Paranthoën et al. [64].

In addition to these issues with the alignment of the turbulent heat flux, investigations have shown that the magnitude of the heat flux vector is often incorrectly represented by EDMs. The validity of these models is based on Morkovin's hypothesis, which states that compressibility affects turbulence only through variations of the mean density, not the density and temperature fluctuations [65]. This assumption loses its validity in high-speed flows where temperature fluctuations must be taken into account [66].

The simplest extension of EDMs is the use of a variable turbulent Prandtl number. Empirical algebraic equations for the turbulent Prandtl number in turbulent pipe and channel flows were for example published by Kays [61] and Abe and Antonia [67]. A more sophisticated approach was proposed by Roy et al. [68]. Based on the observation that the turbulent Prandtl number is not constant in shock/boundary layer interactions, which leads to an overprediction of the turbulent heat flux by EDMs. They propose a model that includes an additional transport equation for the shock function $\psi \in [0, 1]$, which is unity everywhere except in the proximity of shock waves:

$$\frac{\partial}{\partial t}\overline{\rho}\psi + \frac{\partial}{\partial x_i}(\overline{\rho}\tilde{u}_i\psi) = \overline{\rho}\psi\tilde{S}_{ii} - \overline{\rho}(\psi - \psi_0)\frac{\sqrt{\tilde{u}_i\tilde{u}_i}}{L_\epsilon}, \tag{2.52}$$

with $L_\epsilon = \sqrt{k}/\omega$. This transport equation is constructed so that ψ decreases quickly across a shock but returns to its undisturbed value slowly downstream, which appears to capture the physics of shock/turbulence interaction well. The turbulent Prandtl number is computed from ψ:

$$\mathrm{Pr_T} = \frac{3}{4}\frac{\zeta}{1 + b_1\left(\left(\frac{1}{\psi} - 1\right)\right)}, \tag{2.53}$$

with

$$\zeta = 1 + \left(\frac{0.89}{0.75} - 1\right)\exp\left(\chi\left(1 - \frac{1}{\psi}\right)\right) \tag{2.54}$$

and

$$b_1 = 0.4 + 0.6\left(\frac{6\psi - 1}{5\psi}\right)^{5.2} \tag{2.55}$$

χ is a tunable model parameter. The model was implemented in NSMB and improves the wall heat flux prediction for Shock/Turbulent Boundary Layer Interaction (STBLI) cases, with a minor impact on computational efficiency and stability.

These approaches still rely on the eddy diffusivity assumption and the underlying assumption that turbulent energy transport is parallel to the mean temperature gradient. As an alternative, authors have proposed formulations for the turbulent heat flux based on the exact transport equation for the turbulent energy flux, similar to the derivation of EARSMs. Examples include the models by Rogers et al. [69] and Müller et al. [70].

CHAPTER 3

Methods

All simulations in this thesis were done with the NSMB CFD (Computational Fluid Dynamics) solver, which was extended with the CHT functionality. The code was originally developed by EPFL Lausanne [71, 72] and is now utilized and advanced by a consortium of multiple European research facilities [73].

The development of the solver focused on hypersonic and reentry vehicles early on [74] and is still used for these applications [75–77]. Other physical domains can also be handled, recent extensions to NSMB include, e.g., subsonic icing simulations on aircraft structures [78], basic turbulence research [79], and investigations of rotating detonation engines [80]. Details of the code and more of its methods can be found in the NSMB documentation [81]. In the following chapter, the methods relevant for the investigated hypersonic flows and conjugate heat transfer simulations are presented.

3.1 Finite-Volume Method

Except for some canonical problems, exact algebraic solutions of the Navier-Stokes equations and heat equation are unknown. Approximate solutions are therefore required, which can be found even for complex geometries. The three main approximative approaches are the Finite-Difference Method (FDM), the Finite-Element Method (FEM), and the Finite-Volume Method (FVM). While their formulation appears different, they all represent special cases of the Method of weighted residuals [82, 83].

All these methods can be applied to solve fluid mechanics and heat transfer problems. Which method is best suited depends on the particular problem. The FDM is numerically efficient and can be extended easily to higher-order in space, but requires a coordinate transformation for arbitrary meshes and care must be taken to ensure global conservation [84]. The FEM allows high spacial accuracy without the need for large stencils, but it can become unstable for solutions with discontinuities, and it is inherently implicit which makes it computationally expensive [83]. The FVM is inherently conservative, and it can handle complex geometries with unstructured meshes. Since it uses the integral form of the governing equations, the solution may also be discontinuous [34]. The extension beyond second-order accuracy in space, however, is not as straightforward as for the FDM [85].

The FVM is a natural fit for fluid mechanics problems and is therefore used in many commercial and scientific CFD codes, such as NSMB. The computation of a solution in cell-centered FVM codes usually involves the following steps:

1. Divide the entire domain into non-overlapping cells. In general, the cells can have any shape, polygons (2D) and polyhedrons (3D) are typically used. When quadrilaterals or hexahedra are used, the cells can be stored in a structured manner, which allows direct access of cell neighbors. Note that there are also methods that allow cell overlap, such as the chimera method [86], but special attention must be paid to the interpolation in overlapping regions to maintain the conservative properties of the FVM.

2. Express the governing equations in integral form for each cell.

3. Extrapolate the state vector, or flux vector to the cell faces: The state vector is stored in the cell centers, so the values at the cell faces must be computed first. On domain boundaries, the values must be chosen such that the physical boundary conditions are satisfied.

4. Numerically integrate the fluxes over the cell faces. This reduces the integral over the cell surface to a sum over its faces. Different methods for numerical quadrature may be used. The midpoint rule, which is second-order accurate in space, is often applied.

5. Compute the temporal derivative of the state vector.

6. Advance the solution in time, both implicit and explicit methods can be applied.

The starting point for the method is the symbolic form of any governing equations, such as the RANS equations. This equation is now integrated over an arbitrary control volume V with surface S and then Gauss' theorem is applied [87], which gives the following integral form:

$$\int_V \frac{\partial \boldsymbol{W}}{\partial t} \, \mathrm{d}V + \oint_S \boldsymbol{F}_i n_i \, \mathrm{d}S - \oint_S \boldsymbol{F}_{\mathrm{v},i} n_i \, \mathrm{d}S = \int_V \boldsymbol{S} \mathrm{d}V, \tag{3.1}$$

where $\boldsymbol{W}$ is the state vector, $\boldsymbol{F}_i$ are the x_i-components of the inviscid flux vector and $\boldsymbol{F}_{\mathrm{v},i}$ are their viscous counterparts. $\boldsymbol{S}$ is the vector of volumetric source terms and n_i are the components of the cell face unit normal vectors.

By interpreting the state vector $\boldsymbol{W}$ as the average state vector in the control volume V, the volume integral can be replaced. Similarly, the surface integrals are replaced by the aforementioned quadrature. Figure 3.1 shows a section of a structured 2D cell-centered finite-volume mesh, the third dimension was omitted for the sake of simplicity. The state vector $\boldsymbol{W}$ is stored for the center of each cell, while coordinates are stored for the intersections of grid lines.

Boundary conditions can either be enforced by specifying $\boldsymbol{W}$ or $\boldsymbol{F}_i$ along the domain boundaries, or by introducing ghost cells around the domain and filling them
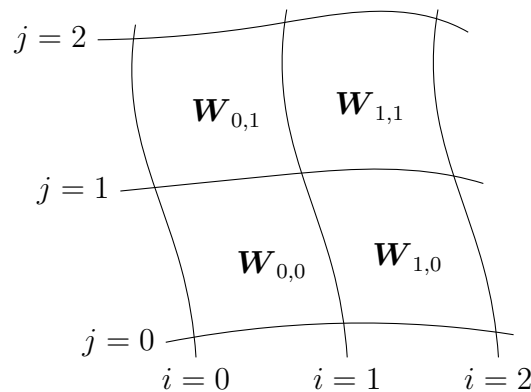
Figure 3.1: Mesh for a 2D cell-centered finite-volume method

appropriately. With the first method, the boundaries of the domain must be treated separately. By appropriately specifying $\boldsymbol{W}$ in the ghost cells, the desired boundary condition can be achieved without altering the numerical method. Ghost cells are used for the boundary conditions in NSMB.

Based on their type, different boundary conditions can be distinguished. A Dirichlet boundary condition specifies the value of the solution at the boundary. In the CHT domain this is for example used for isothermal parts, where a constant temperature is specified. A Neumann boundary condition on the other hand specifies the gradient of the solution at the boundary. In the CHT simulation, this is used for constant heat flux boundaries, where $\boldsymbol{q} = -\lambda \nabla T$ is specified. Finally, at Robin boundary conditions, some functional relation between the value of the solution and its gradient are specified. In the CHT simulations, this occurs at the solid/fluid interface when convex radiation is included.

NSMB uses a block-structured solver. The grid may consist of multiple blocks, for which the data is organized in multidimensional arrays and cells can uniquely be accessed by their i, j, k indices along grid lines. Cell neighbor values are directly available without the need for a connectivity matrix, resulting in simpler code and faster performance. On the other hand, it also reduces the flexibility, since only quadrilateral (2D) and hexahedral (3D) cells can be used. Between blocks, values are exchanged between timesteps. Adjacent blocks may be oriented arbitrarily, which gives the required flexibility to simulate complex geometries.

As stated above, the finite-volume method is a natural fit for fluid mechanics applications due to its conservative form. The integral form of the governing equations is particularly useful for flows with discontinuities like shock waves and therefore lends itself to the application for hypersonic flows.

The FEM is often the preferred method for thermal solvers, due to its high spacial accuracy and the lack of discontinuities in solutions of the heat equation. As shown by Reinert [28], the FVM for heat conduction problems shows a higher mesh dependency. He used tetrahedral grids in the solid domain, which resulted in noticeable mesh effects in the finite-volume solution, which were not visible with FEM. By using hexahedral grids, mesh effects are typically reduced, so the FVM can produce

adequate solutions. Furthermore, using the FVM for the thermal solver simplifies the implementation of the algorithm, since existing data structures and routines can be used.

3.1.1   Spacial Discretization of Inviscid Fluxes

For the cell-centered FVM, the inter-cell fluxes must first be determined from adjacent cell values. The simplest method for calculating the cell face flux is a central scheme, where the flux can either be averaged directly or computed from the averaged state vector. For the face between cells i, j, k and $i + 1, j, k$ this gives

$$\boldsymbol{F}_{i+1/2,j,k} = \frac{1}{2} \left(\boldsymbol{F}_{i+1,j,k} + \boldsymbol{F}_{i,j,k} \right), \qquad (3.2)$$

or

$$\boldsymbol{F}_{i+1/2,j,k} = \boldsymbol{F} \left(\boldsymbol{W}_{i+1/2,j,k} \right) = \boldsymbol{F} \left(\frac{1}{2} \left[\boldsymbol{W}_{i+1,j,k} + \boldsymbol{W}_{i,j,k} \right] \right). \qquad (3.3)$$

Due to the nonlinearity of the convective flux, these forms are not equivalent.

In non-smooth flows, i.e., flows with discontinuities, central schemes produce spurious oscillations that require the addition of artificial dissipation. The explicit addition of numerical dissipation was initially introduced by von Neumann [88], the implementation in NSMB follows the method by Swanson and Turkel [89].

Instead of averaging between adjacent cells, flux-vector splitting and flux-difference splitting represent approaches that leverage the physical propagation direction of information to better approximate the inter-cell flux. For flux-vector splitting, the flux is considered a superposition of forward- and backward-propagating particle streams [90]. For flux-difference splitting, the flux is found as the solution of the local Riemann problem [91].

The governing equations in a 1D reference frame normal to the cell face may be written in the form

$$\frac{\partial \boldsymbol{W}}{\partial t} + \frac{\partial \boldsymbol{F} \left(\boldsymbol{W} \right)}{\partial x} = 0. \qquad (3.4)$$

General solutions of the local Riemann problem contain left- or right-running compression waves, expansion waves, and contact waves. For the integration of the governing equation in time, we are interested in $\boldsymbol{F}(x = 0, t > 0)$, when the interface is placed at $x = 0$ at time $t = 0$. Figure 3.2 shows the wave pattern of a Riemann problem with one left- and one right-running wave. By integrating eq. (3.4) over the closed domain ABCD, the state vector $\boldsymbol{W}(x = 0, t = \Delta t)$ can be found, and by integrating over AEFD or BCFE, the inter-cell flux can be determined.

Cases with three waves, two pressure waves and one contact discontinuity, can be treated analogously. Since the left and right wave speeds S_{L} and S_{R} depend on the state vector between the waves, the solution must be found iteratively [92]. For approximate Riemann solvers such as the HLLE (Harten, Lax, van Leer, Einfeldt) [93, 94] and HLLC (Harten, Lax, van Leer, Contact) [95], a priori assumptions for the wave speeds are made, and the solution can be found explicitly.
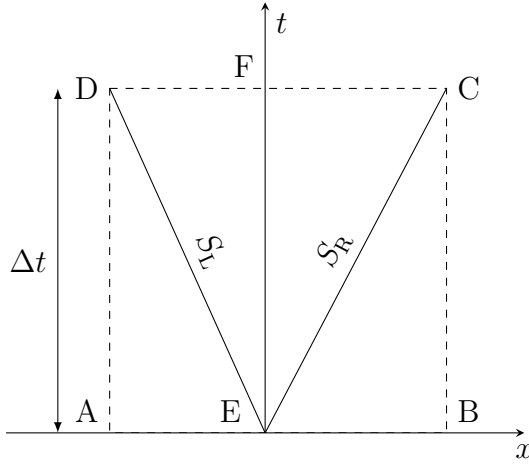
Figure 3.2: Wave patterns for a Riemann problem with one left- and one right-running wave

For the inviscid part of the flux vector in turbulent RANS simulations, the same schemes that were developed for the Euler equations are used. An extension of the HLLE Riemann solver, which is designed to overcome issues with RANS models in Shock/Turbulence Interaction (STI) cases numerically, has been published and described in more detail [96, 97], so only a brief overview is given here. The scheme is referred to as HLLESU (HLLE Shock Unsteadiness). RANS models typically overpredict the production of turbulence across shocks due to the large velocity gradients near strong waves [96]. This seems partly related to the excessively steep mean flow gradients across shocks that RANS models produce [98]. A more appropriate numerical treatment of the inter-cell flux could limit the mean velocity gradient and therefore reduce the turbulence amplification.

The discrete waves in figure 3.2 transform to continuous fans in Reynolds-averaged turbulent solutions, see figure 3.3. Schemes developed for inviscid flows neglect this and may therefore be partly to blame for the poor performance of RANS models in STI cases. In the original paper [96], the derivation of the inter-cell flux and state vector is described in detail, so the concept is only briefly outlined here. The variance of the left and right wave speeds $\Delta S_{\mathrm{L}} = S_{\mathrm{L,max}} - S_{\mathrm{L,min}}$ and $\Delta S_{\mathrm{R}} = S_{\mathrm{R,max}} - S_{\mathrm{R,min}}$ is related to the left and right turbulence kinetic energy. In [96], $\Delta S \propto \sqrt{2/3k}$ is proposed, so the wave speed variance is proportional to the magnitude of the velocity fluctuations.

Similar to the inviscid case, the integration over the closed domains in space-time can be performed. Inside the fans (lines DD' and CC'), linear distributions of the state vector are assumed. The resulting expression of the inter-cell flux depends only on the limiting wave speeds and the left and right state and flux vectors. The scheme has shown to add numerical dissipation to the inter-cell flux by increasing the wave speeds artificially [97]. The shock/boundary layer interaction case in [97], however, shows that excessive numerical dissipation leads to an overprediction of the surface heat flux compared to experiments.
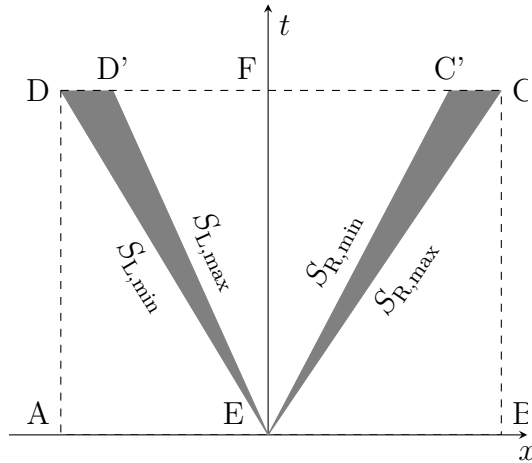
Figure 3.3: Wave patterns of a Reynolds-averaged turbulent Riemann problem

The flux-difference and flux-vector splitting methods use $\boldsymbol{W}$ on the left and right of the cell face to find the inter-cell flux. When the values in the adjacent cell centers are used, the schemes are first-order accurate in space. To increase the spacial accuracy, extrapolation to the cell sides with MUSCL (Monotonic Upstream-centered Scheme for Conservation Laws) [99], or ENO (Essentially Non-Oscillatory) [100] type schemes is used before applying the flux-splitting.

The MUSCL scheme with second-order accuracy in space is used for the simulations in this thesis, which can be used with a range of limiter functions. A comparison of the popular limiters by van Albada [101], van Leer [102], and Venkatakrishnan [103], and the minmod function is presented in section 5.1.1. Since they are used as the local switch between first- and second-order discretization, the limiter functions have a large impact on the stability, convergence, and accuracy of the spacial scheme. They remove spurious oscillations by locally switching to first-order discretization where the gradient of the state vector is zero, i.e., in local extrema. The inherent reduction to first-order accuracy at real extrema is a defect of this method. Due to their specific form, some limiters hinder convergence in regions where the flow is nearly constant [103]. Limiter functions such as the modified version by van Albada and the one by Venkatakrishnan aim to solve this.

3.1.2   Spacial Discretization of Viscous Fluxes

The viscous fluxes in the RANS equations require the computation of gradients for the shear stresses and the heat flux. Two options are available for calculating the gradient of a scalar field variable ϕ: the Peyret-Taylor method [104] (which is often referred to as Green-Gauss method), and the path integral method by Wesseling et al. [105].

The Peyret-Taylor method makes use of the divergence theorem. For any control
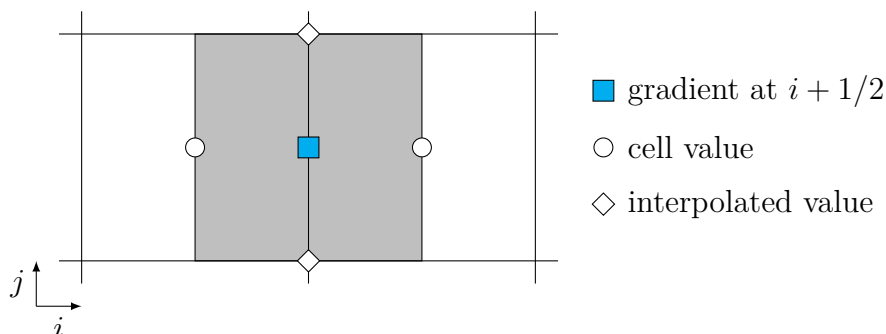
Figure 3.4: Gradient calculation for cell i at face $i + 1/2$ with the Peyret-Taylor method; The shifted control volume is shown in gray.

volume V the volume-averaged gradient of field variable ϕ is

$$\overline{\nabla\phi} = \frac{1}{V} \int_V \nabla\phi \; \mathrm{d}V. \tag{3.5}$$

Using Gauss' theorem, we can write:

$$\overline{\nabla\phi} = \frac{1}{V} \oint_S \boldsymbol{n}\phi \; \mathrm{d}S. \tag{3.6}$$

The surface integral can then be approximated by the sum over the cell faces:

$$\overline{\nabla\phi} \approx \frac{1}{V} \sum_s \boldsymbol{n}_s \phi_s A_s. \tag{3.7}$$

In the finite-volume framework, the gradients on the cell faces are required. To compute these, a shifted control volume, centered on the cell face, is constructed. See figure 3.4 for the approach in two dimensions. Applying eq. (3.7) on this shifted volume gives an approximation of the gradient on the cell face. The required values on the faces of the shifted volume are either known directly as cell-center values (circles) or must be interpolated from adjacent cells (diamonds).

Figure 3.5 shows a schematic for the gradient calculation with Wesseling's path integral method. The variation between the cell values can be written by integrating the gradient along the dashed lines:

$$\phi_D - \phi_C = \int_{\boldsymbol{x}_C}^{\boldsymbol{x}_D} \nabla\phi \; \mathrm{d}\boldsymbol{x} \approx \nabla\phi \cdot (\boldsymbol{x}_D - \boldsymbol{x}_C) , \tag{3.8}$$

$$\phi_E - \phi_A + \phi_F - \phi_B = \int_{\boldsymbol{x}_A}^{\boldsymbol{x}_E} \nabla\phi \; \mathrm{d}\boldsymbol{x} + \int_{\boldsymbol{x}_B}^{\boldsymbol{x}_F} \nabla\phi \; \mathrm{d}\boldsymbol{x}$$
$$\approx \nabla\phi \cdot ((\boldsymbol{x}_E - \boldsymbol{x}_A) + (\boldsymbol{x}_F - \boldsymbol{x}_B)) . \tag{3.9}$$

These two equations (three in three dimensions) can be solved for the components of gradient $\nabla\phi$. The solution of the system of equations is done once before the simulation, which allows an efficient computation of the gradient with a simple matrix multiplication.
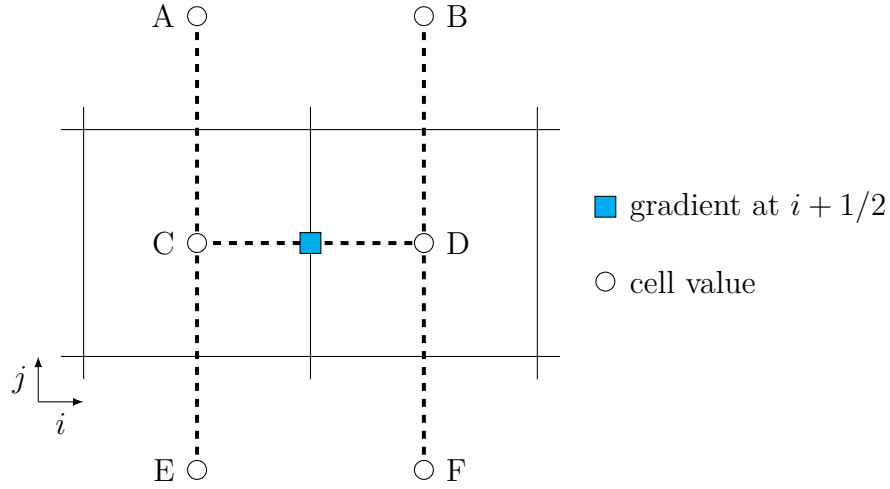
Figure 3.5: Gradient calculation with Wesseling's path integral method for cell i at face $i + 1/2$

Note that these gradient calculation methods can be used to compute gradients at cell faces, but also in cell centers by choosing the integration domains accordingly. Cell center gradients of the velocity components are required for the turbulent source terms and cell face gradients are needed for the heat flux and the shear stress tensor in the viscous flux. The velocity gradient tensor can be calculated by applying the methods above to the velocity components u_i.

The Peyret-Taylor method requires the mesh to be orthogonal and uniform to be second-order accurate in space. Where the mesh does not meet these criteria, the accuracy reduces to first-order. The Wesseling method, on the other hand, only uses the position of cell center values and is therefore largely independent of the mesh quality. Due to that, it retains its second-order accuracy everywhere at the cost of reduced stability.

3.2 Temporal Discretization

Since the blocks in NSMB can either contain only fluid, or only solid cells, different temporal discretization methods can be used for the fluid and solid domain. Explicit and implicit time integration methods can be distinguished. In explicit methods the state vector at the next time increment is only a function of previous time increments

$$\boldsymbol{W}^{n+1} = f\left(\boldsymbol{W}^n, \boldsymbol{W}^{n-1}, \boldsymbol{W}^{n-2}, ...\right), \tag{3.10}$$

in implicit methods the state vector at the next time increment is also function of itself

$$\boldsymbol{W}^{n+1} = f\left(\boldsymbol{W}^{n+1}, \boldsymbol{W}^n, \boldsymbol{W}^{n-1}, \boldsymbol{W}^{n-2}, ...\right). \tag{3.11}$$

Implicit methods require more computational effort to solve for the next time increment but allow for a larger timestep to be taken since they are unconditionally

stable. This can reduce the overall computational cost to find a solution. Explicit schemes on the other hand are much simpler to implement, and it can be easier to find a numerical setup that converges reliably.

For steady state fluid blocks, an implicit time scheme is used. The governing equations (3.1) discretized in space can be written in the following symbolic form:

$$V\frac{\partial \boldsymbol{W}}{\partial t} + \boldsymbol{R}(\boldsymbol{W}) = 0 \tag{3.12}$$

with the state vector $\boldsymbol{W}$ and the residual function $\boldsymbol{R}$, which contains the fluxes and source terms. An implicit scheme can be constructed by linearizing eq. (3.12) about timestep n:

$$\left[\frac{V}{\Delta t}\mathbf{I} + \left(\frac{\partial \boldsymbol{R}}{\partial \boldsymbol{W}}\right)^n\right]\left(\boldsymbol{W}^{n+1} - \boldsymbol{W}^n\right) = -\boldsymbol{R}(\boldsymbol{W}^n), \tag{3.13}$$

where $\mathbf{I}$ is the identity matrix. Note that the Jacobian matrix $\partial \boldsymbol{R}/\partial \boldsymbol{W}$ only affects the stability, not the accuracy of steady state solution. A reasonable approximation is therefore sufficient.

Equation (3.13) is a linear system of equations of the type $\mathbf{A}\boldsymbol{x} = \boldsymbol{b}$ and can be solved for the state vector at the next time increment $\boldsymbol{W}^{n+1}$. Since $\mathbf{A}$ is a large, sparse matrix, the computational effort and storage requirements for its inversion prohibit an exact solution and an iterative method must be used. The LU-SGS method implemented in NSMB [106] has shown stable convergence towards steady state even for large timesteps. The implicit iteration is performed for each block separately with exchange of block connectivity boundary conditions between iterations, which allows the utilization of parallel computing architectures. Because of that, however, the convergence compared to a fully implicit method is reduced, especially when the computational domain is partitioned into a large number of small blocks.

When running time-accurate simulations with an implicit method, an exact solution of eq. (3.13) is necessary, which is computationally expensive. Hence, dual time-stepping methods can be used, where a derivative of the state vector in pseudo time is added to the governing equations [107]. The solution at the next time increment in physical time is equivalent to a steady state solution in pseudo time, convergence acceleration techniques, such as local time-stepping and multigrid can therefore be used. Flow problems with strong shocks often fail to converge reliably, which requires a reduction of the size of the physical timestep or an increase in the number of pseudo timesteps. Because of that, an explicit time scheme is used for unsteady simulations, which avoids the need for the costly inner time-stepping loop. Three-stage or five-stage Runge-Kutta schemes are available for fluids in NSMB.

Since solid materials respond slowly compared to fluids, explicit time schemes are adequate for conjugate heat transfer simulations. The solid blocks are therefore integrated in time using an explicit four-stage Runge-Kutta scheme [108], which is fourth-order accurate in time. We define the residual function f as

$$f(T) := \frac{\partial(\rho E)}{\partial t} = \frac{1}{V}\sum_s \boldsymbol{n}_s \cdot \boldsymbol{q}_s A_s = -\frac{1}{V}\sum_s \boldsymbol{n}_s \cdot \nabla T_s \lambda_s A_s, \tag{3.14}$$

from which the intermediate solutions k_i

$$k_i = f(T^n + \alpha_i \Delta t k_{i-1}) \text{ for } i = 1...4, \qquad (3.15)$$

can be computed. The solution at the next time increment can then be found:

$$(\rho E)^{n+1} = (\rho E)^n + \Delta t \frac{1}{6}(k_1 + 2k_2 + 2k_3 + k_4). \qquad (3.16)$$

The parameters α_i are $\alpha_1 = 0$, $\alpha_2 = 1/2$, $\alpha_3 = 1/2$, $\alpha_4 = 1$. In addition to the Runge-Kutta scheme, an explicit first-order Euler method was also implemented, but is not used in the simulations in this thesis due to more stringent stability constraints.

3.3 Parallel Implementation

As stated above, NSMB uses block-structured meshes and boundary conditions are applied with ghost cells. The approach is very flexible and allows for the generation of structured meshes even for complex geometries. Prior to the simulation, the grid in each block can be split up further to better utilize parallel computing architectures. These blocks can be distributed between processors, and allow for parallel, non-synchronous updates of the state vector and application of local boundary conditions. After each iteration, cell values are sent to adjacent blocks where necessary, and block-connectivity boundary conditions are filled.

The implemented conjugate heat transfer algorithm is fully integrated into the parallel multi block approach of NSMB. Solid parts of the domain are treated as separate blocks, that can also be split further. The solid/fluid interface is implemented as a special version of a regular block-connectivity boundary condition.

3.4 Bow Shock Adaptation

The numerical treatment of solutions with shock waves requires special attention. Unlike earlier shock-fitting approaches [109], modern solvers mostly use shock-capturing methods. Near discontinuities, additional dissipative terms are added to the governing equations, which smear them over a distance in the order of the cell size. The additional terms can be explicit through artificial viscosity [88], or implicit through total-variation diminishing (TVD) schemes [110].

While shock-capturing methods can produce solutions on all meshes, it is still useful to adapt the mesh to strong shock waves. The first argument for shock adaptation is the fact that shock waves inherently introduce a first-order error to the solution. This stems from the uncertainty of the exact shock location, which scales with the local mesh size [111]. Reducing the grid size around shocks can therefore improve the accuracy of the solution. The second argument is one of numerical stability. Misalignment of the shock and the grid lines gives rise to spurious oscillations [112]. These can be reduced by improving the shock alignment and refining the shock region.

Mesh adaptation techniques generally employ a combination of two strategies: refinement and redistribution. For refinement, nodes are added to the grid where required; for redistribution, the topology of the mesh stays the same but mesh nodes are moved inside the domain. Unstructured grids can be refined with relative ease by dividing cells where necessary and updating the connectivity matrix. Because NSMB uses block structured meshes, these same methods cannot be applied without complex remeshing. Alternative approaches must be taken. One possibility is the algorithm by Berger and Colella [113], where topologically rectangular blocks of cells are grouped into new grids that can be refined by integer factors. Each of the grids is functionally equivalent to the blocks in NSMB, so the same procedure for transferring information and integrating in time could be applied. However, the implementation of this algorithm still requires significant changes to the code.

The applied mesh adaptation algorithm only moves grid points inside the domain. It is an improved version of the method that was already implemented in NSMB, which redistributes the grid points on lines normal to the inlet and can therefore only adapt the mesh to the outer bow shock layer. While more general approaches, such as the one by Ameur and Lani [114], can adapt the grid to complex shock geometries without topological constraints, the algorithm is expensive for large meshes and the mesh quality can deteriorate locally near strong gradients.

The mesh adaptation is performed in the following steps:

1. Find the location along grid lines normal to the inlet where the local Mach number falls below a specified threshold and store the minimum index for each block

2. Find the minimum index of all blocks on all processors.

3. Find the position of the shock with the criterion from the first step and compute the distance to the inlet.

4. Optionally smooth the shock distance per block using Bézier curves.

5. Redistribute cells.

The redistribution of the cells is done by splitting the distance to the inlet into four sections. At the side opposite to the inlet a given number of cells are not changed to ensure consistent wall spacing. On either side of the shock, a small constant spacing is used for a number of cells. Between the wall layer and the shock layer, cells are distributed using a choice of second-, fifth-, or seventh-order polynomial, which enforces a continuous transition of the grid spacing between the sections. The higher-order methods also enforce a vanishing growth rate of the spacing at the ends. The remaining spacing between the freestream and the shock layer is filled with an exponential function.

3.5 Conjugate Heat Transfer Approach

3.5.1 Coupling Procedure With Fluid Solver

As mentioned in the introduction, conjugate heat transfer simulation methods can be distinguished based on how tightly the fluid- and thermal-solver are coupled. For the loosely coupled approach, different solvers are often used for the fluid and solid domains and the coupling is achieved through exchange of boundary values. Due to the slow thermal response of solid materials compared to fluids, fluid simulations with a constant wall temperature are often carried out. The resulting wall heat flux is then used as a Neumann boundary condition for an unsteady heat transfer simulation in the solid. When the coupling interval is reached, the solid surface temperature is transferred and used as a Dirichlet boundary condition in the fluid. The simulation of the fluid domain can be unsteady [25], or steady state when the fluid timescale is significantly smaller than the solid timescale [28].

When fluid and solid domains are loosely coupled, the heat equation in solid domains is often discretized with the FEM, while the FVM is used for the fluid domain. The mesh in either domain can be optimized for the respective physical process. The main drawback of the method is a loss of accuracy when fluid and solid domains are not coupled after each timestep. When the coupling is performed frequently, the exchange of boundary values can result in a significant time penalty, especially when external files are used for the transfer of boundary conditions.

For the tightly coupled approach, both solid and fluid domains are solved with the same software and boundary conditions can be transferred directly between the domains. Time-accurate simulations are straightforward to conduct by using the same global timestep for all domains and applying the coupling boundary condition after each step. While the finite-volume method is not the classical choice for heat conduction problems, its major advantage, the global and local conservation of energy, is very beneficial for fluid and solid problems alike.

In this thesis, the tightly coupled approach was chosen. Figure 3.6 shows the implemented procedure of the CHT coupling in NSMB. In the multi block framework of NSMB, individual blocks can be treated as solid, so the heat equation is solved. A single mesh is generated using ICEM CFD, which includes the fluid and solid domains. Grid lines normal to the interface are continuous, which allows a direct one-to-one mapping. After the fluid and solid blocks are initialized, local boundary conditions and block-connectivity boundary conditions are filled, and both domains are advanced in time. For steady state solutions, local time-stepping is used to accelerate the convergence, for unsteady simulations, a global timestep is used.

At solid/fluid interfaces, the coupling boundary condition (CHT BC) is filled. A new boundary condition with the internal number (BC537) was introduced in NSMB for that. It ensures continuous interface temperature and interface heat flux in the solid and fluid. From the energy balance of the interface surface (see figure 3.7), we find

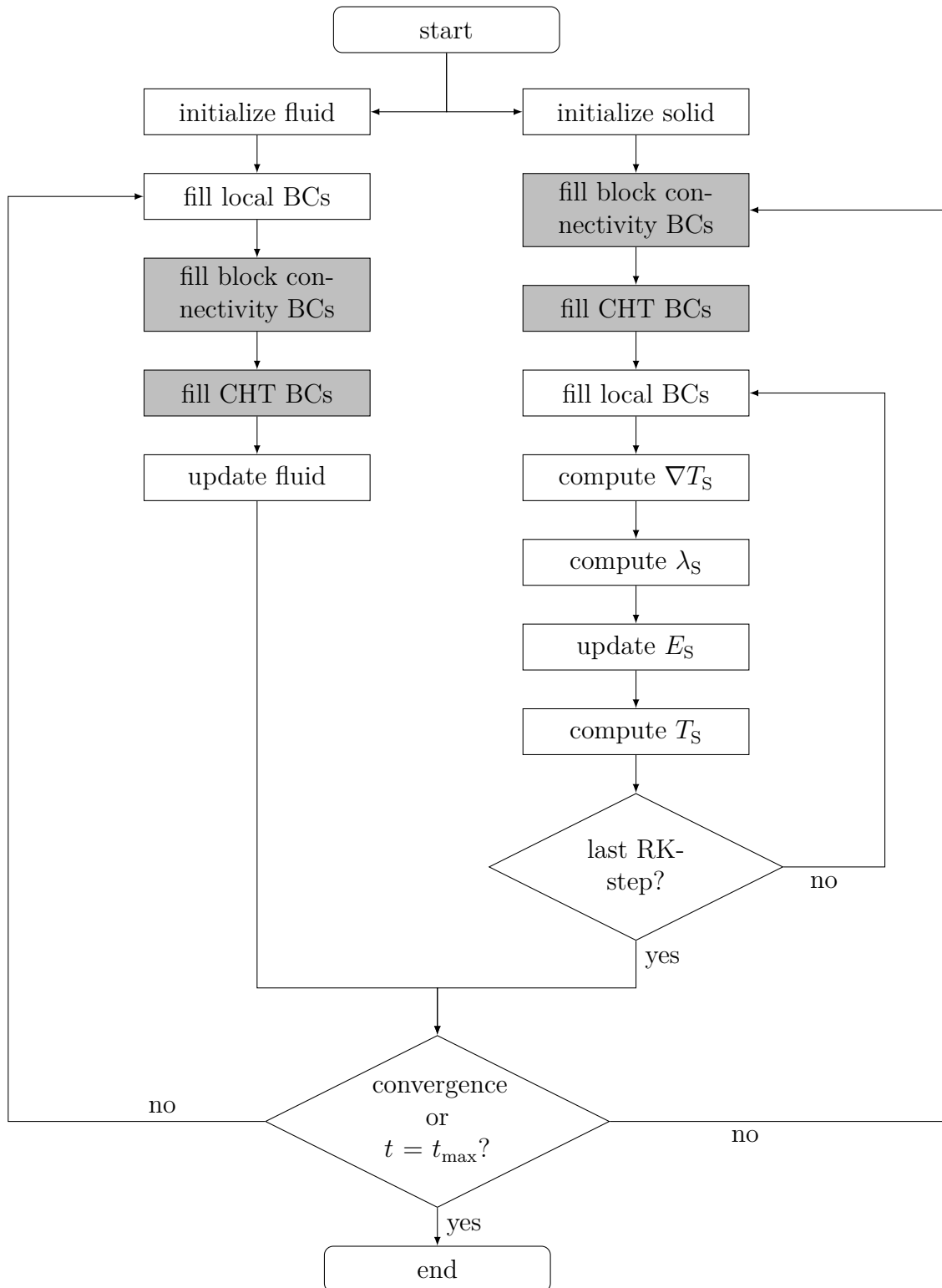$$q_{\text{tot}} = q_{\text{fluid}} + q_{\text{solid}} + q_{\text{rad}} + q_{\text{diff}} = 0, \tag{3.17}$$

Figure 3.6: Conjugate heat transfer coupling procedure in the multi block solver: The processes involving communication between blocks are highlighted in gray.
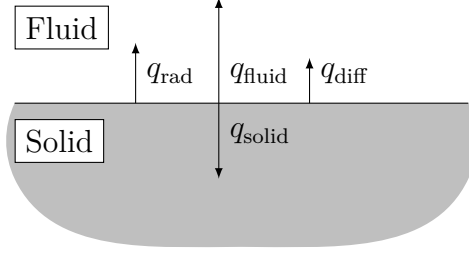
Figure 3.7: Heat fluxes for the conjugate heat transfer problem

when all heat fluxes are defined so that they are orthogonal to and point away from the interface.

q_{fluid} and q_{solid} refer to the respective conduction heat fluxes, q_{rad} is the divergent radiative heat flux and q_{diff} is the heat flux due to mass diffusion. Although it is relevant for high-speed flows with chemical reactions [21], the mass diffusion heat flux is often neglected [22, 24–26, 28]. Using Fourier's law for the conduction heat fluxes, the Stefan-Boltzmann law for the radiative term, and Fick's law for the mass diffusion, we find

$$
\begin{aligned}
q_{\text{tot}} = & -\lambda_{\text{F,W}} \left(\frac{\partial T}{\partial x_{\text{n}}} \right)_{\text{F,W}} - \lambda_{\text{S,W}} \left(\frac{\partial T}{\partial x_{\text{n}}} \right)_{\text{S,W}} \\
& + \sigma \epsilon T_{\text{W}}^4 - \rho_{\text{W}} \sum_s h_{s,\text{W}} D_{s,\text{W}} \left(\frac{\partial Y_s}{\partial x_{\text{n}}} \right)_{\text{F,W}} = 0,
\end{aligned}
\tag{3.18}
$$

where $h_{s,\text{W}}$ and $D_{s,\text{W}}$ are the enthalpy and the diffusion coefficient of species s at the wall and x_{n} is the wall normal coordinate. In addition to the energy balance, the temperature must be continuous across the interface, so $T_{\text{W,F}} = T_{\text{W,S}} = T_{\text{W}}$. Note that only an outgoing radiative heat flux is included in eq. (3.18), which is only valid for convex geometries and when the gas is transparent. For the chosen cases, this assumption is acceptable. Non-convex radiative effects can be included in NSMB with the GETHRA module (GEneral THermal RAdiation) [115], but due to computational limitations was not considered in the CHT method. Note that no turbulent eddy diffusivity must be added to the fluid heat conductivity $\lambda_{\text{F,W}}$ and the diffusion coefficients $D_{s\text{W}}$ since all turbulent fluctuations vanish at solid walls.

For a numerical implementation of eq. (3.18), the derivatives are replaced by finite-difference approximations. Using a first-order approximation, this gives

$$
\begin{aligned}
q_{\text{tot}} = & -\lambda_{\text{W,F}} \frac{T_{\text{F}} - T_{\text{W}}}{\Delta x_{\text{n,1,F}}} - \lambda_{\text{W,S}} \frac{T_{\text{S}} - T_{\text{W}}}{\Delta x_{\text{n,1,S}}} \\
& + \sigma \epsilon T_{\text{W}}^4 - \rho_{\text{W}} \sum_s h_{s,\text{W}} D_{s,\text{W}} \frac{Y_{s,\text{F}} - Y_{s,\text{W}}}{\Delta x_{\text{n,1,F}}} = 0.
\end{aligned}
\tag{3.19}
$$

T_{F} and T_{S} are the temperature of the first cell in the fluid and solid domains, respectively, and T_{W} refers to the interface temperature and $Y_{s,\text{W}}$ are the species mass fractions at the wall. $\Delta x_{\text{n,1}}$ is the wall normal distance of the first cell center.

Equation (3.19) can be solved for the interface temperature. Due to the nonlinear radiative term, the temperature dependency of the transport properties and the composition Y_s at the wall, an iterative solution is necessary. The Newton-Raphson method was chosen in the implementation, which typically converges in a couple of iterations:

$$T_{\mathrm{W}}^{n+1} = T_{\mathrm{W}}^{n} + \frac{q_{\mathrm{tot}}(T_{\mathrm{W}}^{n})}{q_{\mathrm{tot}}'(T_{\mathrm{W}}^{n})}, \tag{3.20}$$

with

$$q_{\mathrm{tot}}'(T_{\mathrm{W}}^{n}) = \frac{\mathrm{d}q_{\mathrm{tot}}}{\mathrm{d}T_{\mathrm{W}}}. \tag{3.21}$$

This derivative can be approximated as

$$q_{\mathrm{tot}}'(T_{\mathrm{W}}) \approx \frac{\lambda_{\mathrm{W,F}}}{\Delta x_{\mathrm{n,1,F}}} + \frac{\lambda_{\mathrm{W,S}}}{\Delta x_{\mathrm{n,1,S}}} + 4\sigma\epsilon T_{\mathrm{W}}^{3} \tag{3.22}$$

for the first-order method. Since q_{tot}' does not affect the accuracy of the solution, the simplified approximation above is sufficient, which neglects the temperature dependency of the heat conductivities and mass fractions. These are only updated between Newton-Raphson iterations.

For the diffusion heat flux, the gas composition at the interface $Y_{s,\mathrm{W}}$ is required. The current implementation is limited to equilibrium flows, for which the wall composition can be computed from two thermodynamic variables. Since the thermal state of the interface is unknown prior to solving (3.18), it must be found iteratively. Assuming a vanishing wall-normal pressure gradient, the interface pressure is prescribed. From the pressure and an initial guess for the interface temperature, the density and internal energy at the interface are computed. This step must be performed iteratively due to the way the equilibrium composition is computed in NSMB. The composition at the interface can then be calculated from the equilibrium state. Now, a new interface temperature can be computed with eq. (3.20). Once the interface temperature is determined, the ghost cell temperatures in the solid and fluid domain are filled by linear extrapolation:

$$T_{\mathrm{ghostcell}} = 2T_{\mathrm{W}} - T_{\mathrm{F/S}} \tag{3.23}$$

The internal energy of the fluid is computed, and the state vector is filled accordingly.

In an effort to improve the accuracy near the solid/fluid interface for large temperature gradients, it is also possible to use a second-order approximation for the gradients in the interface boundary condition. Since non-unity growth rates are typically used near the interface, a finite-difference approximation for non-uniform meshes is required. In this work a simplification of the more general compact finite-difference stencils described by Gamet et al. [116] is used. The scheme uses the wall normal coordinate of the wall point and the two points next to it $x_{\mathrm{W}} = x_{\mathrm{n,0}}$, $x_{\mathrm{n,1}}$, $x_{\mathrm{n,2}}$, with the respective spacings h_1 and h_2 ($h_i = x_{\mathrm{n,i}} - x_{\mathrm{n,i-1}}$). Based on the spacings, the

following parameters are defined:

$$A_1 = \frac{h_1 + h_2}{h_1 h_2}, \tag{3.24}$$

$$A_2 = -\frac{h_1}{h_2(h_1 + h_2)}, \tag{3.25}$$

$$A_3 = -\frac{2h_1 + h_2}{h_1(h_1 + h_2)}. \tag{3.26}$$

The gradient of any scalar at the interface can then be expressed as:

$$\frac{\partial \phi}{\partial x_{\mathrm{n}}}(x_{\mathrm{n},0}) = A_1 \phi(x_{\mathrm{n},1}) + A_2 \phi(x_{\mathrm{n},2}) + A_3 \phi(x_{\mathrm{n},0}). \tag{3.27}$$

This single-sided finite-difference expression is second-order accurate in space and reduces to the standard first-order finite-difference for uniform spacing ($h_1 = h_2$) and a linear distribution of ϕ. It provides a more accurate approximation for cases with strong curvature, i.e., $\left| \partial^2 \phi / \partial x_{\mathrm{n}}^2 \right| \gg 1$. The derivatives in (3.18) can then be replaced by these finite-difference terms:

$$\begin{aligned}
q_{\mathrm{tot}} = & -\lambda_{\mathrm{F,W}} \left(A_{1,\mathrm{F}} T_{\mathrm{F}} + A_{2,\mathrm{F}} T_{\mathrm{F},2} + A_{3,\mathrm{F}} T_{\mathrm{W}} \right) \\
& -\lambda_{\mathrm{S,W}} \left(A_{1,\mathrm{S}} T_{\mathrm{S}} + A_{2,\mathrm{S}} T_{\mathrm{S},2} + A_{3,\mathrm{S}} T_{\mathrm{W}} \right) \\
& + \sigma \epsilon T_{\mathrm{W}}^4 \\
& - \rho_{\mathrm{W}} \sum_s h_{s,\mathrm{W}} D_{s,\mathrm{W}} \left(A_{1,\mathrm{F}} Y_{s,\mathrm{F}} + A_{2,\mathrm{F}} Y_{s,\mathrm{F},2} + A_{3,\mathrm{F}} Y_{s,\mathrm{W}} \right) = 0. \tag{3.28}
\end{aligned}$$

$T_{\mathrm{F},2}$ and $T_{\mathrm{S},2}$ are the cell temperatures in the second cell away from the solid/fluid interface in the fluid and solid domain, respectively. $Y_{s,\mathrm{F}}$ and $Y_{s,\mathrm{F},2}$ are the mass fractions of species s in the first and second cell.

The equation is also solved with the Newton-Raphson method, where the functional derivative is

$$q'_{\mathrm{tot}} \approx -\lambda_{\mathrm{W,F}} A_{3,\mathrm{F}} - \lambda_{W,S} A_{3,\mathrm{S}} + 4\sigma \epsilon T_{\mathrm{W}}^3. \tag{3.29}$$

Due to the single-sided first- and second-order finite-differences in the coupling conditions above, a continuous mesh spacing is not required across the interface. Since the thermal conductivity is typically much larger in the solid, the temperature gradient is much smaller than in the fluid boundary layer. Significantly larger cells may therefore be used in the solid domain.

The implemented method also includes the option to simulate a composite material. The coupling between two different solids follows the same idea given in eq. (3.18). By neglecting diffusion and radiative heat fluxes, the interface temperature between two solids with different heat conductivity can be found analogously.

3.5.2   Other Boundary Conditions for the Solid Solver

In addition to the solid/fluid interface boundary condition, solid blocks can also have adiabatic and isothermal sides, and they may be in contact to other solid domains. For the adiabatic solid wall (internal identifier BC580) the wall normal temperature gradient must vanish:

$$T_{\text{ghost cell}} = T_{\text{S}}. \tag{3.30}$$

At isothermal walls, the temperature is directly found from extrapolating the specified temperature:

$$T_{\text{ghost cell}} = 2T_{\text{isothermal}} - T_{\text{S}}. \tag{3.31}$$

At constant heat flux boundary conditions, a positive heat flux is defined towards the solid. The ghost cells can then be filled:

$$q = \frac{\lambda_{\text{W}}}{|\boldsymbol{x}_{\text{ghost cell}} - \boldsymbol{x}_{\text{S}}|}(T_{\text{ghost cell}} - T_{\text{S}}) \tag{3.32}$$

$$\rightarrow T_{\text{ghost cell}} = \frac{q(|\boldsymbol{x}_{\text{ghost cell}} - \boldsymbol{x}_{\text{S}}|)}{\lambda_{\text{W}}} + T_{\text{S}}, \tag{3.33}$$

with $\lambda_{\text{W}} = {}^{1}\!/_{2}(\lambda_{\text{S}} + \lambda_{\text{ghost cell}})$. When a temperature-dependent heat conductivity is used, eq. (3.33) must be solved iteratively, the Newton-Raphson method is used again. The boundary condition type for the isothermal and constant heat flux conditions is BC581. At block connectivity boundaries between two solid blocks of the same material, the temperature can directly be transferred. The gradient calculation methods described in section 3.1.2 require appropriate treatment of block edges and corners. Linear extrapolation from the inside of the block is applied for both.

3.5.3   Timescale Problem in High-Speed Flows

It is a well-known issue of coupled conjugate heat transfer simulations that there is a significant disparity between the solid and fluid timescales [21, 117, 118], which results in excessive simulation times. The maximum timestep size in fluid simulations with explicit time schemes is limited by the CFL (Courant-Friedrichs-Lewy) condition CFL ≤ 1, where

$$\text{CFL}_{\text{fluid}} = \frac{(|u| + c)\Delta t}{\Delta x}. \tag{3.34}$$

Δx is the local cell size and c is the speed of sound. The maximum possible timestep size is small, since $|u| + c$ is large and Δx is small near boundary layers. Since the fluid reacts quickly to external constraints, however, the required simulated time to steady state is short. Solid materials, on the other hand, react orders of magnitude more slowly, which requires a much longer timespan to be simulated. Since they react so slowly, however, the maximum possible timestep, determined by the CFL number for diffusion processes

$$\text{CFL}_{\text{solid}} = \frac{2a\Delta t}{\Delta x^2}, \tag{3.35}$$

is also much larger.

Solutions to both fluid-only and solid-only problems can be found relatively quickly, since the ratio of simulated time to timestep size, i.e., the required number of iterations, is similar. When running time-accurate CHT simulations, the entire domain must use the same timestep. In most cases the small cells in the boundary layer of the fluid domain limit the maximum possible timestep, while the slow response of the solid material requires a long simulated time. This results in an excessive number of timesteps and large computational effort. The timescale problem is not limited to high-speed flows, but it is especially relevant here, since the high fluid velocity requires very small timesteps.

Multiple approaches have been proposed in literature to deal with this issue. Where temperature variations are small, an uncoupled approach might be acceptable. First, a steady state fluid simulation with isothermal walls is done and the heat transfer coefficient $\alpha = q_\mathrm{W}/(T_\mathrm{W}-T_\mathrm{ref})$ is computed. This is used to apply a Neumann boundary condition for an unsteady solid simulation. While this approach is fast, it assumes that $\alpha \neq \alpha(T_\mathrm{W})$, which is generally not true [119].
More accuracy can be achieved, with a loosely coupled approach. It is similar to the uncoupled method, but the fluid solution and the respective heat transfer coefficient are updated periodically, as the wall temperature changes. Zope et al. [29] use this approach and compare it to their subcycling method, which uses different timesteps for fluid and solid to achieve a speedup. Koren et al. apply a similar method [118]. Zhang et al. [24] use a loosely coupled approach in which the coupling frequency is chosen adaptively based on the rate of change of the interface temperature. These methods can speed up simulation times significantly, but the coupling frequency must be chosen carefully to ensure accuracy.

For problems where the type of the solution is known a priori, efficient quasi-steady methods may be constructed, e.g., for oscillating heat loads. For these types of conditions, the solution can be written as a harmonic series. The unsteady problem in real time can then be transformed into a steady state problem in pseudo-time; a solution is found efficiently [117]. While it is very efficient, the approach only works for problems with solutions that are sinusoidal in time.

Since the basis of the numerical difficulties is the large disparity of timescales, the issue can be alleviated by equalizing the timescales. The ET (equalizing timescales) method was proposed by Diefenthal et al. [119] and was used for analyzing the heating of turbomachinery components. In this approach, the specific heat of the solid material is artificially decreased by a factor $c_\mathrm{ET} > 1$:

$$c'_\mathrm{S} = \frac{c_\mathrm{S}}{c_\mathrm{ET}}. \tag{3.36}$$

This results in a scaling of the thermal diffusivity

$$a'_\mathrm{S} = a_\mathrm{S}c_\mathrm{ET}, \tag{3.37}$$

which ultimately speeds up the material response, since

$$\frac{\partial T}{\partial t} = a'\frac{\partial^2 T}{\partial x_i^2}. \tag{3.38}$$

Assuming that the heat transfer coefficient α does not depend on c_{ET}, the Fourier number

$$\mathrm{Fo} = \frac{a_{\mathrm{S}} t}{L^2} \tag{3.39}$$

and Biot number

$$\mathrm{Bi} = \frac{\alpha L}{\lambda_{\mathrm{S}}} \tag{3.40}$$

are independent of c_{ET}. The heat transfer problem, once scaled back to physical time by c_{ET} is therefore mathematically similar to the original problem. Speeding up the solid response should be valid, as long as the timescales of fluid and solid are not equalized completely. Steady state solutions are governed by $\partial^2 T / \partial x_i^2 = 0$ and are therefore independent of the material properties and the scaling parameter. [119]

The ET method can achieve a significant speedup since c_{ET} in the order of 10^3 can be used. Since an increase of a decreases the maximum possible timestep, see eq. (3.35), solid cells may become limiting for the global timestep. The maximum usable c_{ET} is therefore restricted. The method is straightforward to implement in existing thermal solvers and since it keeps the tight coupling between solid and fluid it should be more accurate than loosely coupled approaches. Compared to quasi-steady approaches, however, the computational effort is still significantly higher.

CHAPTER 4

Validation

Since the conjugate heat transfer methodology was newly implemented in NSMB, a thorough validation is required. As stated in chapter 2, conjugate heat transfer is a complex phenomenon, that involves multiple physical processes in the fluid and solid domain, all of which must be modeled accurately. This makes the validation of the method complicated, because uncertainties in all applied models can have a large impact on the heat transfer to the solid. In the relevant hypersonic flows this problem is intensified since the surface heating depends heavily on the thermophysical gas properties and turbulence, the accurate representation of which is non-trivial.

The validation methodology in the following chapter is therefore limited to three simple cases of heat transfer in solids with analytical solutions or data from literature, and two coupled cases, for which there is reasonable confidence in the required models. Once the method is validated for these simple cases, its performance for high-speed flows should be equally satisfying. For all validation cases, the gradients were computed with Wesseling's path integral method, and the first-order interface method was used for the coupled cases. The four-stage Runge-Kutta scheme was used for temporal discretization of the solid domain.

4.1 Steady State Heat Conduction With Analytical Solution

The steady state heat equation for an axisymmetric problem can be written in polar coordinates [30]:

$$\frac{\partial^2 T}{\partial r^2} + \frac{1}{r}\frac{\partial T}{\partial r} = 0.$$ (4.1)

The general solution to that is
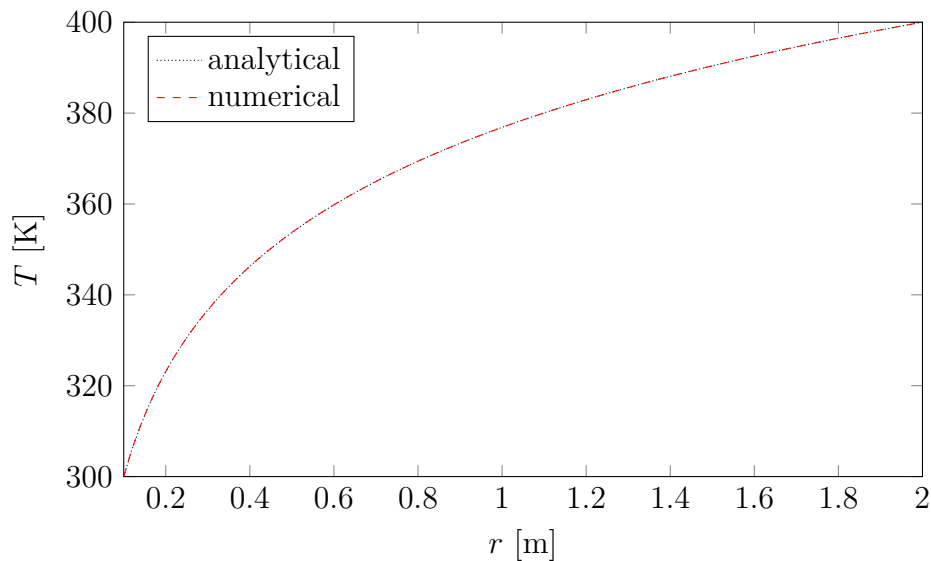
$$T(r) = a\ln(r) + b.$$ (4.2)

Figure 4.1: Radial temperature distribution in the steady state cylinder shell

For a cylinder shell with given temperatures $T(r_1) = T_1$ and $T(r_2) = T_2$, the parameters a and b can be found:

$$a = \frac{T_1 - T_2}{\ln(r_1) - \ln(r_2)}, \tag{4.3}$$

$$b = T_1 - a\ln(r_1). \tag{4.4}$$

A simulation on a cylinder shell with $T_1 = 300$ K at $r_1 = 0.1$ m and $T_2 = 400$ K at $r_2 = 2$ m was conducted, the comparison to the analytical solution is shown in figure 4.1. A 2° wedge with 500 uniform cells in radial direction was used. The agreement between the analytical and numerical solutions is excellent. This shows that the gradient calculation is sufficiently accurate to capture even small variations between the size of adjacent cells.

4.2   2D Unsteady Heat Conduction Problem

To validate the accuracy of the implemented algorithm for two-dimensional heating problems, the composite solid block case proposed by Liu [120] and investigated by Ferrero et al. [21] is computed. The rectangular block has a width of $w = 0.9$ m and a height of $h = 0.3$ m and consists of a bronze block (0.3 m $< x <$ 0.6 m) sandwiched between two copper blocks (see figure 4.2). The properties of the two materials are given in table 4.1. The domain was discretized using a uniform cell distribution with 150 cells horizontally and 49 cells vertically. The domain is initialized with a temperature of $T_0 = 300$ K, a constant heat flux of $q = 9000$ $^{W}/_{m^2}$ is applied to the lower edge at $y = 0$ m, all other edges are held at a constant temperature of $T = 400$ K.

material	a [m²/s]	c [J/kgK]	λ [W/mK]
copper	1.167×10^{-4}	384.91	401
bronze	8.820×10^{-6}	340.0	26

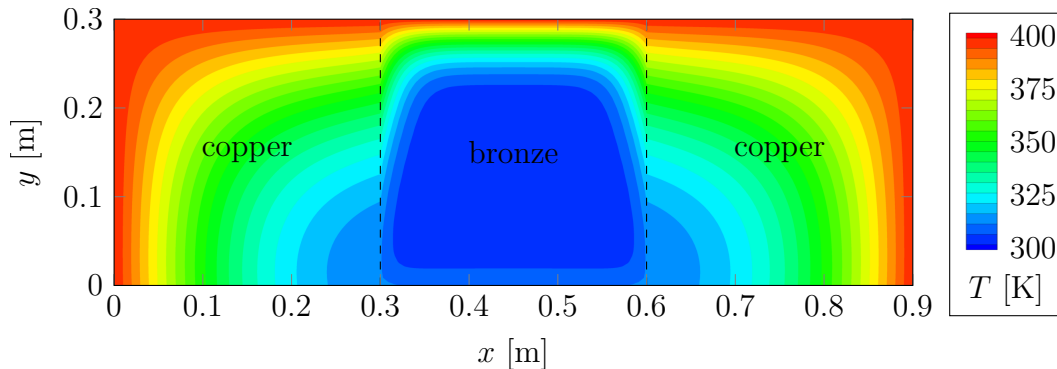Table 4.1: Material properties for the two-dimensional unsteady conduction case, taken from [21]

Figure 4.2: Temperature distribution for the unsteady two-dimensional conduction validation case by Liu [120] at $t = 80$ s after initialization

The temperature distribution $t = 80$ s after initialization in figure 4.2 shows good qualitative agreement with the results by Liu [120] and Ferrero et al. [21]. Quantitatively, the results also agree well with the literature data by Ferrero et al. [21], see figure 4.3. Note that the literature data was extracted from a contour plot that uses a banded colormap. This results in the discontinuities in the extracted temperature lines.

4.3   Unsteady Heating of Semi-Infinite Slab

To validate the transient heating response of the implementation, the heating of a semi-infinite 1-dimensional slab is simulated and compared to an analytical solution. The initial temperature of the slab is $T_0 = 300$ K, then a constant heat flux of $q = 1 \times 10^5$ W/m² is applied to the upper surface. The lower surface is isothermal at $T = 300$ K. The slab was created as a block of width $w = 100$ mm with a height of h. The mesh in wall normal direction consisted of 80 cells, with a finer resolution at the heat flux boundary. The material is aluminum: $a = 9.88 \times 10^{-5}$ m²/s, $\lambda = 237$ W/mK, and $c = 888$ J/kgK.

For an infinite slab like this, an analytical solution to the temperature distribution can be found [30]:

$$T(x,t) = T_0 + \frac{2q\sqrt{\frac{at}{\pi}}}{\lambda} \exp\left(-\frac{x^2}{4at}\right) - \frac{qx}{\lambda}\left(1 - \mathrm{erf}\left(\frac{x}{2\sqrt{at}}\right)\right), \qquad (4.5)$$
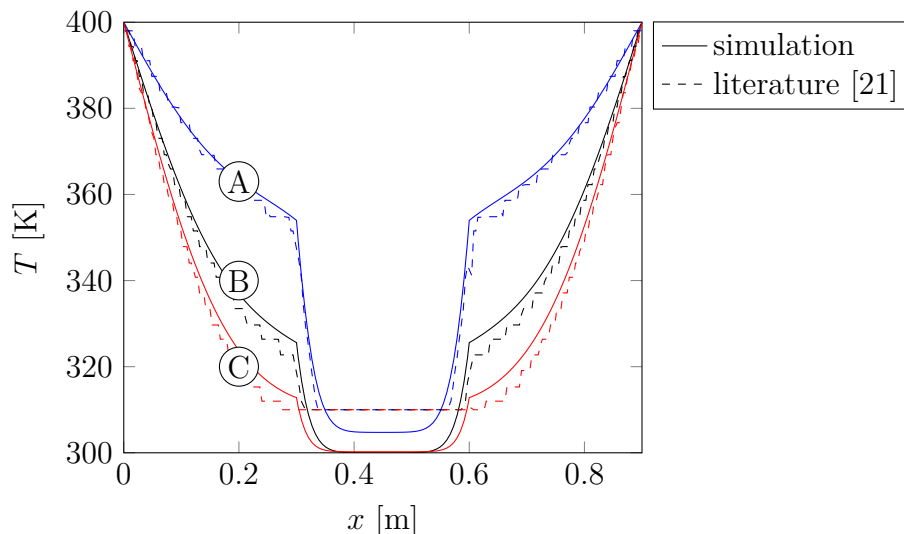
Figure 4.3: Temperature distribution along horizontal lines for the two-dimensional conduction case. A: $y = 0.75h$, B: $y = 0.5h$, C: $0.25h$

where erf is the Gauss error function:

$$\mathrm{erf}(y) = \frac{2}{\sqrt{\pi}} \int_0^y \exp(-t^2) \, \mathrm{d}t. \tag{4.6}$$

Figure 4.4 shows the evolution of the surface temperature on the infinite slab over time. All results are in very good agreement, the numerical results approach the analytical solution as the height h is increased. This indicates that the implemented temporal discretization is time-accurate.

4.4   Steady State Flat Plate CHT Problem

To finally test the implementation of the coupled fluid/solid simulation approach, the laminar flat plate boundary layer case by Montomoli et al. [121] was used. Figure 4.5 shows the domain, which consists of a $100\,\mathrm{mm}$ thick and $400\,\mathrm{mm}$ long flat plate. The flow over the plate is laminar at $\mathrm{Ma}_\infty = 0.13$, with a total temperature of $T_{\mathrm{t},\infty} = 1400\,\mathrm{K}$ and a static pressure of $p_\infty = 101\,350\,\mathrm{Pa}$. The plate has a thermal conductivity of $\lambda_\mathrm{S} = 4\,\mathrm{W/mK}$ and its lower surface is isothermal at $T = 600\,\mathrm{K}$. The fluid is air, Sutherland's law [11] is used for the viscosity and the thermal conductivity is computed using a constant Prandtl number of $\mathrm{Pr} = 0.72$.

The case was used for validation purposes by Montomoli et al. [121], and it also has an analytical solution that was derived by Luikov [122]. He assumed a linear temperature distribution in y-direction of the plate, and used Blasius' solution for the velocity distribution in incompressible flat plate boundary layers [123].

Figure 4.6 shows the normalized temperature distribution in the laminar boundary layer for the literature data [121], the theoretical distribution [122] and the current numerical results. The agreement between the results is satisfactory. Close to
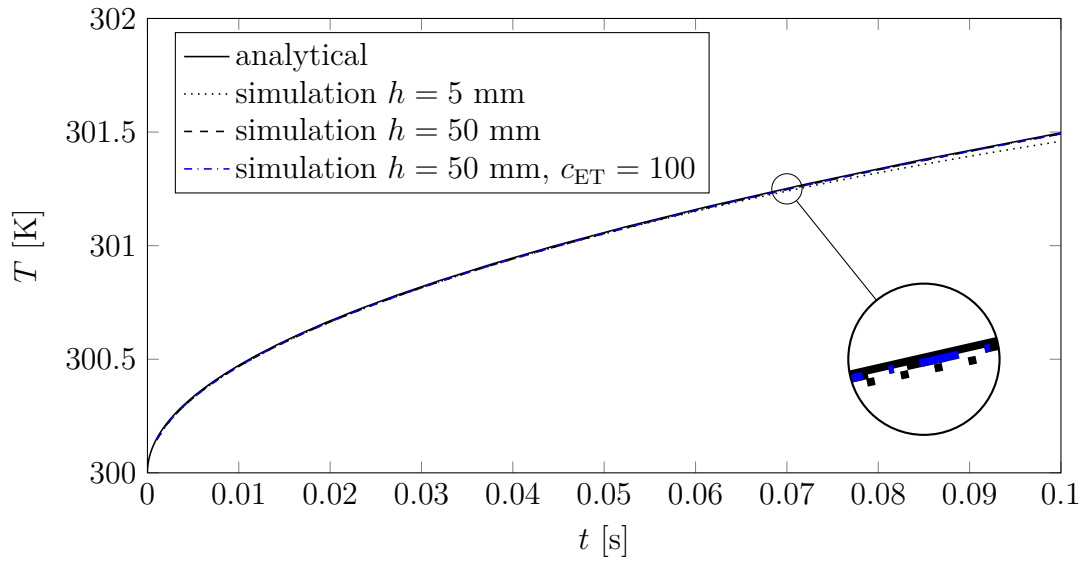
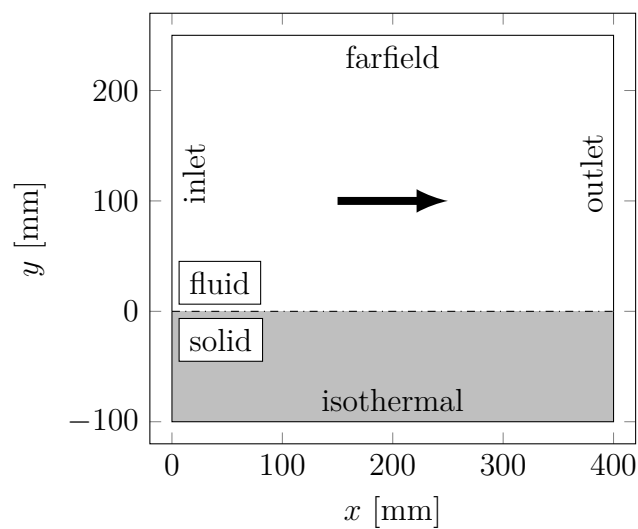Figure 4.4: Evolution of the surface temperature of the infinite slab

Figure 4.5: Laminar flat plate boundary layer case by Montomoli et al. [121]
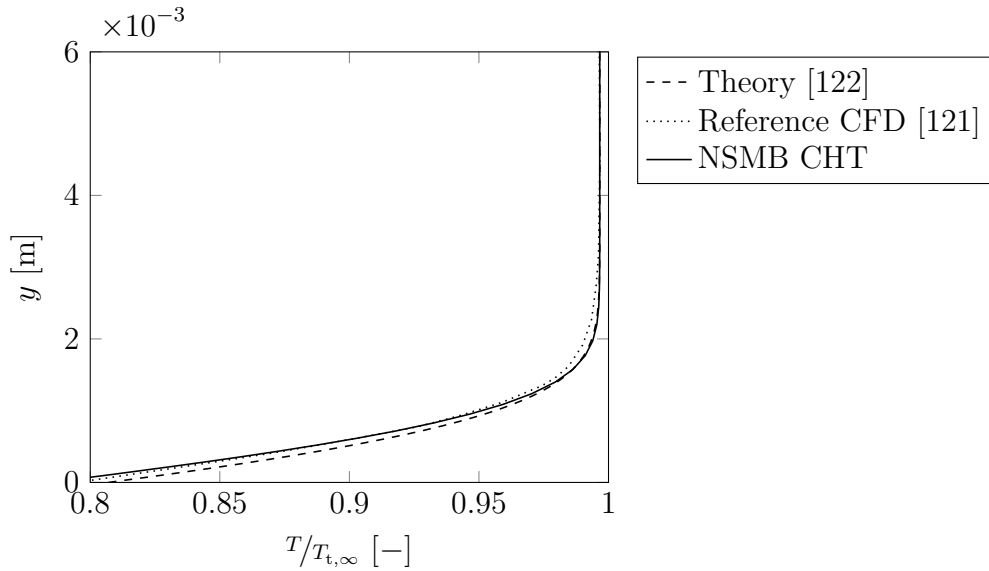
Figure 4.6: Temperature distribution in the boundary layer of the flat plate case by Montomoli et al. at $x = 80\,\mathrm{mm}$ normalized with total temperature in the freestream $T_{\mathrm{t},\infty} = 1400\,\mathrm{K}$

the wall the NSMB results match the data by Montomoli well, at the edge of the boundary layer, they are more similar to the theory. The fluid viscosity and thermal conductivity are not specified in [121], which might be an explanation for their slightly thicker boundary layer.

4.5 Timescale Equalization

To test the validity of the ET method, the heating of a cold copper cylinder with a diameter of $1\,\mathrm{m}$ in $\mathrm{Ma}_\infty = 0.3$ flow with $T_\infty = 288.15\,\mathrm{K}$ was investigated using a range of timescale equalization factors c_{ET}. The material properties of the copper cylinder can be found in table 4.1. A steady state simulation of the fluid domain with a constant wall temperature of $T_{\mathrm{W}} = 100\,\mathrm{K}$ was used to initialize the domain for the unsteady CHT simulation. The initial temperature of the cylinder was also set to $100\,\mathrm{K}$ and simulations were conducted for a maximum of $60\,\mathrm{s}$ in real time.

Figure 4.7 shows the temperature distribution in and around the cylinder at a real time of $60\,\mathrm{s}$ after initialization. The plot only shows a small section of the domain, which is also cylindrical with a radius of 10 cylinder diameters.

The heat Q that is absorbed by the solid material during the simulation from state 1 to state 2 is equal to the change of its internal energy:

$$Q_{\mathrm{in}} = \int e_2 \; \mathrm{d}m - \int e_1 \; \mathrm{d}m = \int_V \rho \int_{T_{\mathrm{ref}}}^{T_2} c \; \mathrm{d}T \; \mathrm{d}V - \int_V \rho \int_{T_{\mathrm{ref}}}^{T_1} c \; \mathrm{d}T \; \mathrm{d}V. \qquad (4.7)$$
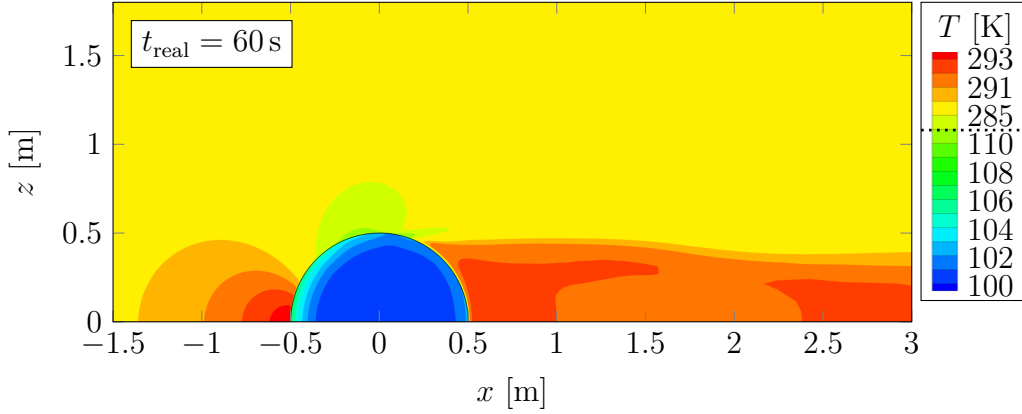
Figure 4.7: Temperature contour around a cylinder in $\text{Ma}_\infty = 0.3$ flow, note the non-linear colormap.

c_{ET} [−]	Q_{in} [J]	Q_{surf} [J]	rel. difference [%]	t_{real} [s]	t_{sim} [s]
1	26 615.73	26 615.82	0.00034	6	6
10	263 993.82	263 976.74	−0.0065	60	6
100	263 897.13	263 880.28	−0.0064	60	0.6
20 000	257 535.39	258 329.68	0.3	60	0.003

Table 4.2: Global energy conservation of the cylinder CHT case

When the material density and specific heat are constant, this simplifies to

$$Q_{\text{in}} = \rho c \int_V (T_2 - T_1) \, \mathrm{d}V. \tag{4.8}$$

The heat can also be computed from the heat flow across its surface

$$Q_{\text{surf}} = \int_{t_1}^{t_2} \oint_S q \, \mathrm{d}S \tag{4.9}$$

For a conservative algorithm, these two quantities must be equal. Table 4.2 shows the agreement of the two values for different timescale equalization factors c_{ET}. To reduce the computational effort, the case with $c_{\text{ET}} = 1$ was not simulated for $t_{\text{real}} = 60\,\text{s}$. The simulated time that effectively passed for the fluid is t_{sim}. At $c_{\text{ET}} = 20\,000$, the minimum timestep in the solid is similar to the minimum timestep in the fluid. The stability is now limited by the solid domain and a further increase of c_{ET} does not speed up the simulation.

The agreement between internal heat increase and surface heat flow is very good for $c_{\text{ET}} \leq 100$, the heating also compares well between these cases. The $c_{\text{ET}} = 20\,000$ case still agrees reasonably well with the other cases given the significant speedup that can be achieved. When accelerating the solid response with the ET method, the solution may start do deviate from the real physical behavior once the assumption that the solid changes much more slowly than the fluid is no longer fulfilled. To judge
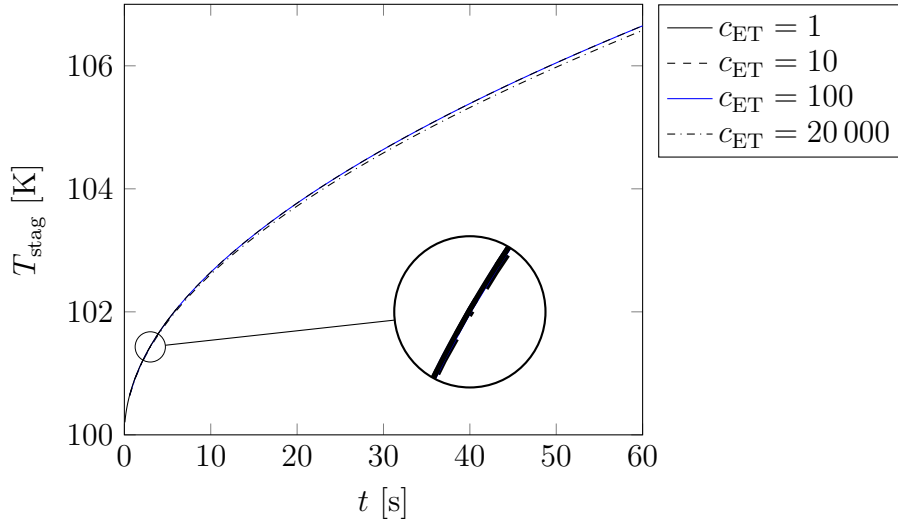
Figure 4.8: Stagnation point temperature for the copper cylinder in Ma $= 0.3$ flow for different timescale equalization factors c_{ET}

that, the number of flow cycles past the diameter of the cylinder of $1\,\mathrm{m}$ during the simulation time t_{sim} is analyzed. In real time the fluid passes the cylinder 6124 times in $60\,\mathrm{s}$. This reduces to 0.3 times for $c_{ET} = 20\,000$, at which point the validity of the assumption that the solid and fluid timescales can be separated must be questioned. Nevertheless, the agreement between internal heating and surface heat transfer does not degrade significantly for higher c_{ET}.

This can also be seen in figure 4.8, which shows the stagnation point temperature over time after rescaling. For $c_{ET} \leq 100$, the evolution of the stagnation temperature is essentially unaffected. Even $c_{ET} = 20\,000$, for which the assumption of timescale separation is no longer valid, gives an acceptable result, especially given the reduction in computational effort. These results agree well with the findings of Maffulli et al. who show that large values of c_{ET} can be used for cases with asymptotic heating [124].

CHAPTER 5

Results

In the previous chapters, the fundamental processes involved in hypersonic simulations were presented along with the methods required to perform numerical simulations. Since aerodynamic heating problems are multiphysics problems, any simulation that hopes to accurately represent a physical process must use suitable methods in multiple domains. Most importantly, simulations must be run on an adequate mesh, with accurate and stable numerics, and with accurate models of the underlying physical and chemical processes.

In the following chapter the importance of these three aspects are outlined for simpler cases. Advancements in methods and modeling are presented. Finally, the methods are applied to realistic cases of critical heating in hypersonic flow.

5.1 Aspects of Modeling and Numerics

5.1.1 Numerics

Flux limiters

The choice of flux limiter has shown to have a big impact on the stability and accuracy of the solution. Two cases were investigated with a range of different limiters to gauge their performance. First, the sphere-cylinder case by Esfahanian et al. [125] is presented. It consists of laminar flow at $\mathrm{Ma}_\infty = 2.94$ around a blunt sphere-cylinder body. A nose radius of $r_\mathrm{n} = 10\,\mathrm{mm}$ was chosen in the present simulations. The remaining freestream conditions were $T_\infty = 293\,\mathrm{K}$ and $\mathrm{Re}_{\infty,r_\mathrm{n}} = 2.2 \times 10^5$. The fluid was treated as a perfect gas with $\gamma = 1.4$ and $R = 287\,\mathrm{J/kg\,K}$ and the HLLC scheme [95] was used for the inviscid fluxes. Unless otherwise noted, a second-order in space MUSCL scheme [99] was used.

Figure 5.1 shows the convergence of the density residual and the adiabatic wall temperature along the body coordinate s for the sphere cylinder case for different limiters. The L2-norm of the volume-weighted density residual is used to judge
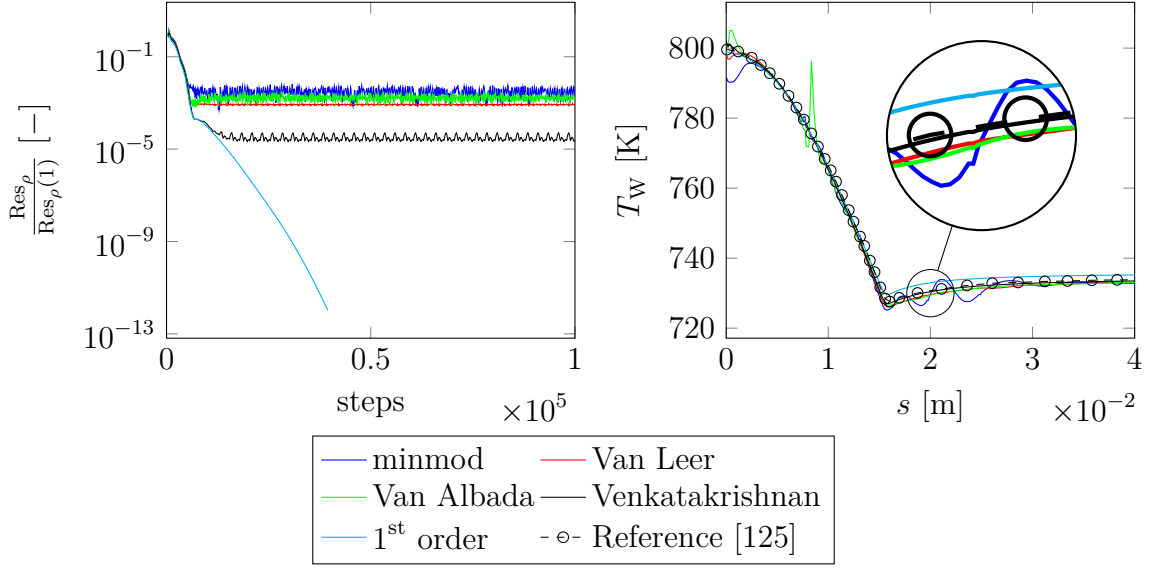
Figure 5.1: Convergence and adiabatic wall temperature for the sphere cylinder case by Esfahanian et al. [125] for different limiters

convergence:

$$\mathrm{Res}_\rho = \sqrt{\sum_n \left(\frac{\partial \rho}{\partial t}\right)_n^2 V_n}. \tag{5.1}$$

n is used as the cell index and V_n are the cell volumes. The value $\partial \rho / \partial t$ is equal to the sum of all fluxes in the continuity equation.

Except for the first-order solution, simulations with all limiters fail to converge due to persisting oscillations in the solution. Only the Venkatakrishnan limiter [103] produces somewhat acceptable convergence. These oscillations are produced where the shock is not properly aligned with the mesh and the mesh resolution is insufficient.

The oscillations propagate to the wall, which can be seen in the adiabatic wall temperature distribution. Along the surface coordinate s, the stagnation point is located at $s = 0\,\mathrm{m}$ and the end of the spherical nose section is found at $s \approx 0.0157\,\mathrm{m}$. Especially the minmod limiter and the modified Van Albada limiter [101] perform poorly and deviate significantly from the literature data. The first-order solution, even though it converges very well, is excessively dissipative, which results in an increased wall temperature. The Venkatakrishnan limiter produces a close agreement to the literature results. It is clear that second-order solutions require a better resolution near the shock to converge properly and produce accurate results.

Mesh adaptation

As the data above suggests, spacial discretization of order higher than one requires additional care for strong shock waves. The automatic mesh adaptation described in section 3.4 can help optimize the mesh and reduce numerical errors. First, the mesh adaptation aligns the grid lines with the bow shock, which means that the mesh
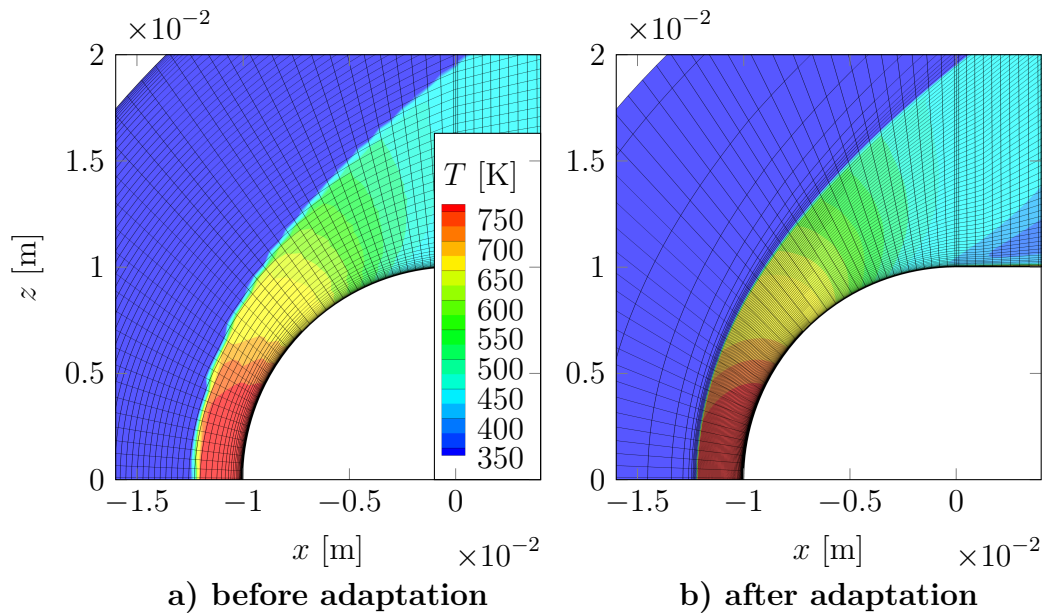
Figure 5.2: Mesh adaptation for the sphere-cylinder case. The van Leer limiter was used to generate the results. Every second grid line is shown.

direction along the shock wave can be discretized fully second-order. Secondly, it refines the grid in the vicinity of the shock wave, which reduces the thickness of the shock wave and the corresponding region of first-order discretization. To show the improvements, the same sphere-cylinder case was run with mesh adaptations after 20 000, 40 000, and 60 000 iterations.

Figure 5.2 shows the mesh before and after the adaptation. For clarity, every other grid line was omitted. The temperature field in a) shows non-physical oscillations downstream of the shock. After the mesh adaptation, the temperature contours are smooth and the bow shock standoff distance is reduced from 2.5 mm before adaptation to 2.25 mm after adaptation.

Figure 5.3 shows the convergence and adiabatic wall temperature distribution for the sphere-cylinder on adapted meshes for the different limiters. The minmod limiter and the modified van Albada limiter still fail to converge even after multiple mesh adaptations. The Venkatakrishnan limiter shows the best convergence even after the first adaptation. The van Leer limiter shows good convergence after the first and third adaptation but produces a residual stall after the second. Its performance appears to be very dependent on the mesh. The likely cause is small misalignment of the shock with the grid after the second adaptation. Along grid lines parallel to the shock, the solution is nearly constant, which is a known source of convergence problems of many limiters [103].

On the right of figure 5.3, the adiabatic wall temperature distribution is shown in comparison to numerical results by Esfahanian et al. [125]. The wall temperature with the Van Albada and minmod limiter, still show oscillations, but at lower amplitude. The van Leer and the Venkatakrishnan limiter produce a smooth temperature
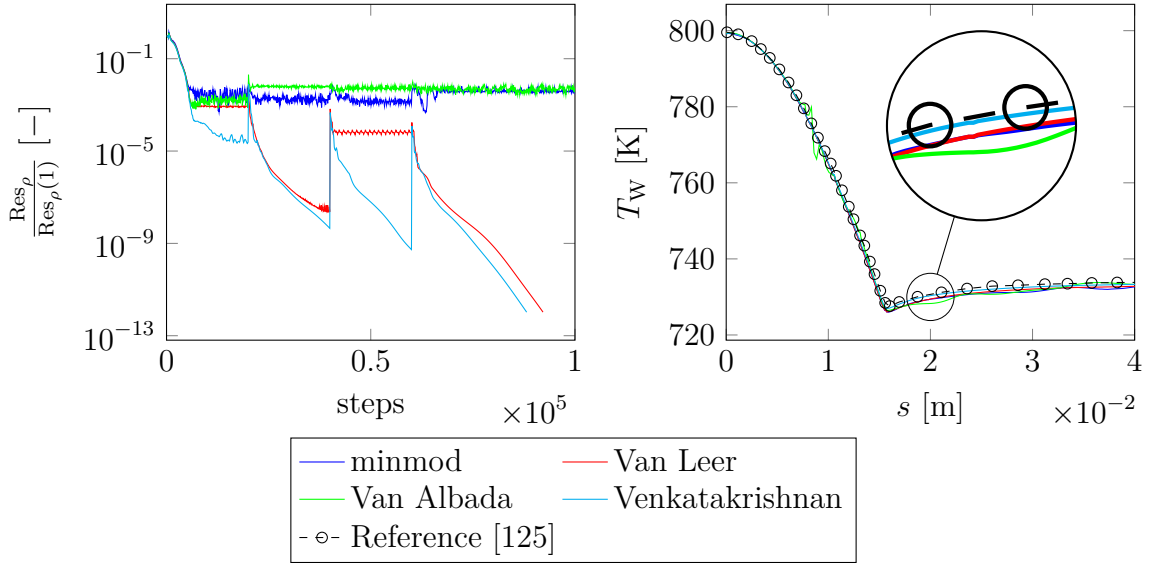
Figure 5.3: Convergence and adiabatic wall temperature for the sphere cylinder case by Esfahanian et al. [125] when mesh adaptation is applied.

contour, the latter matches the literature results best.

5.1.2 Turbulence Modeling

Turbulent Heat Flux Model

As described in section 2.3, simple eddy diffusivity models fall short in reproducing the heat flux in shock boundary layer interactions. The performance of one particular turbulent heat flux model, the one by Roy, Pathak, and Sinha [68], was evaluated. In the following sections, the model is referred to as RPS model. The model still relies on a scalar turbulent conductivity, but it uses a variable turbulent Prandtl number that is calculated from a transported shock function.

To validate the implementation of the model and test its suitability for the cases in this thesis, the Shock/Turbulent Boundary Layer Interaction (STBLI) case by Schülein [126] was investigated. It consists of an oblique shock wave impinging on a turbulent flat plate boundary layer. Figure 5.4 shows the geometry of the STBLI case, the position of the $10°$ shock generator is chosen in a way that the shock impinges $0.35\,\mathrm{m}$ from the leading edge of the plate. The Ma $= 5$ freestream has a total temperature of $T_{\mathrm{t},\infty} = 410\,\mathrm{K}$ and total pressure of $p_{\mathrm{t},\infty} = 2.12 \times 10^{6}\,\mathrm{Pa}$. The medium is air ($\gamma = 1.4$, $R = 287\,\mathrm{J/kg\,K}$, perfect gas) and the isothermal wall has a temperature of $T_{\mathrm{W}} = 300\,\mathrm{K}$.

Figure 5.5 shows the wall heat flux distribution for this case. Compared to the experimental data, the shortcomings of current turbulence models that use the eddy diffusivity approach are obvious. While the heating upstream of the interaction region ($x < 0.35\,\mathrm{m}$) is predicted within the margin of error of the experiment, excessive wall heat flux is observed downstream of the shock. With the RPS model, the turbulent
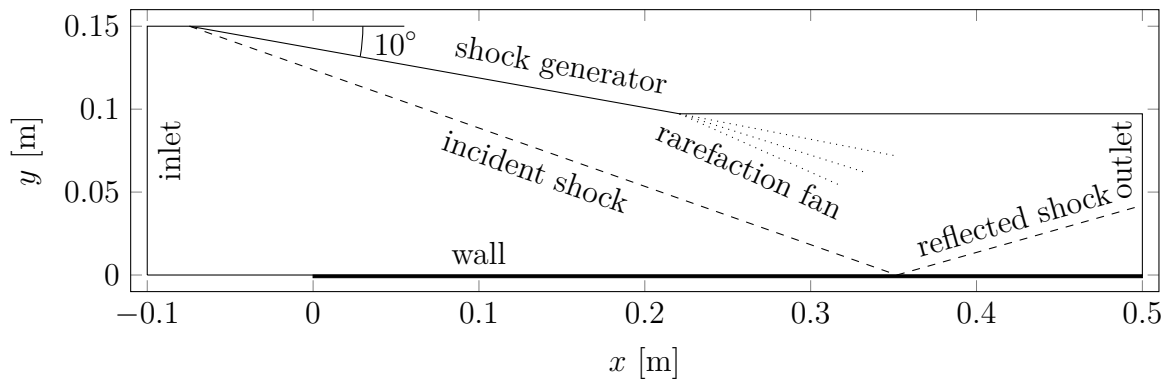
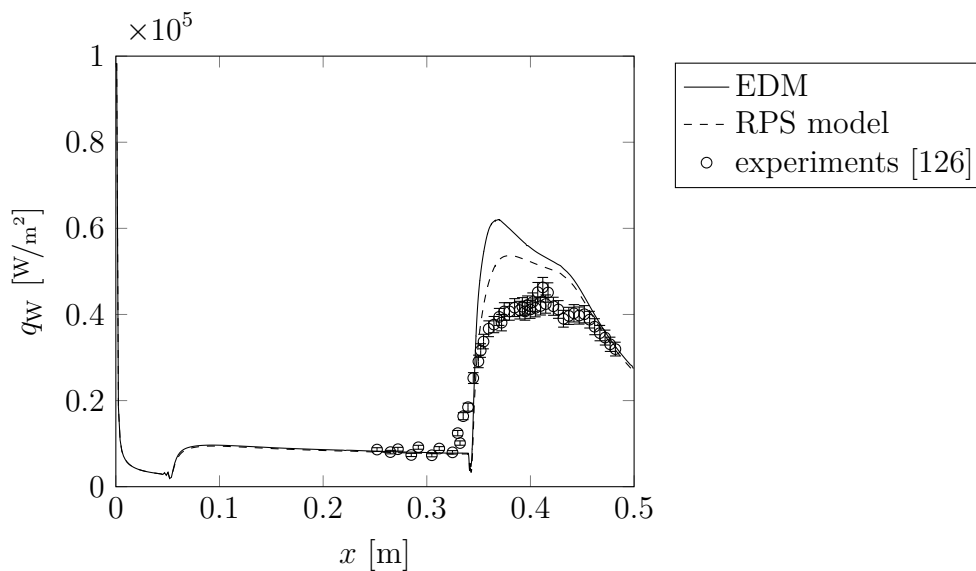Figure 5.4: Domain of the STBLI case by Schülein [126] (from [97])

Figure 5.5: Wall heat flux for the STBLI case by Schülein [126] for the eddy diffusivity model and the RPS model

Prandtl number is decreased in the vicinity of the shock wave, which results in an increased eddy diffusivity. Evidently, the added turbulent heat flux further away from the wall distributes the heat more evenly, which decreases the temperature close to the wall and results in a lower surface heat flux. The results compare reasonably well with the numerical data by Roy et al. [68], who used the RPS model with a $k - \omega$ model that was modified for shock/turbulence interaction.

Ma$_\infty$ [$-$]	grid	cell height fluid [m]	cell height solid [m]	y^+ [$-$]
0.13	1	4×10^{-5}	4×10^{-5}	0.5
	2	1×10^{-4}	1×10^{-4}	1.3
	3	2×10^{-4}	2×10^{-4}	2.5
	4	1×10^{-3}	1×10^{-3}	15.1
5	1	2×10^{-6}	2.6×10^{-3}	0.13
	2	2×10^{-5}	2.6×10^{-3}	1.32
	3	2×10^{-4}	2.6×10^{-3}	13.33

Table 5.1: Grid properties for testing the order of the interface scheme in the flat plate test case

5.2 Conjugate Heat Transfer Methodology

5.2.1 Spacial Order of the Interface

As noted in section 3.5.1 a first- and second-order finite-difference approximation can be used in the CHT coupling boundary condition. To test the two numerical schemes, flat plate boundary layer cases were used. The incompressible conditions, that were used as a validation case in section 4.4, and a Ma$_\infty = 5$ condition with the same total temperature of $T_\mathrm{t} = 1400\,\mathrm{K}$ were chosen. For the Ma$_\infty = 5$ case, the length of the plate was increased to $1\,\mathrm{m}$. Since the second-order scheme can reproduce non-linear distributions more accurately, one would expect a more noticeable difference between first-order and second-order interface boundary conditions when the grid near the interface is coarse. Different grid spacings in wall normal direction were generated, whilst the number of cells and the resolution along the plate remained unchanged. Table 5.1 shows the relevant details about the different grids, note that the y^+ values were calculated from results using the first-order scheme. For the incompressible case, the boundary layer is well-resolved with grid 1 and grid 2, grid 3 gives an acceptable resolution, and grid 4 is significantly under-resolved. Grid 1 was also used for the validation in Section 4.4. Grids with a similar range of y^+ values were also generated for the hypersonic conditions. Near the nose of the plate, the axial spacing was reduced to resolve the weak compression wave due to viscous interaction.

Figure 5.6 shows the temperature profiles near the solid/fluid interface for the incompressible case $x = 80\,\mathrm{mm}$ downstream of the leading edge. On all grids, the second-order method produces a higher interface temperature. As expected, the differences between first- and second-order gradients are most noticeable on the coarsest grid. On grid 1, first- and second-order schemes produce essentially the same interface temperature with only a 0.05% difference between results. On grid 4, the difference between interface temperatures is significantly higher at 3.5%. As the grid resolution is decreased, the interface temperature increases. The boundary layer is visibly
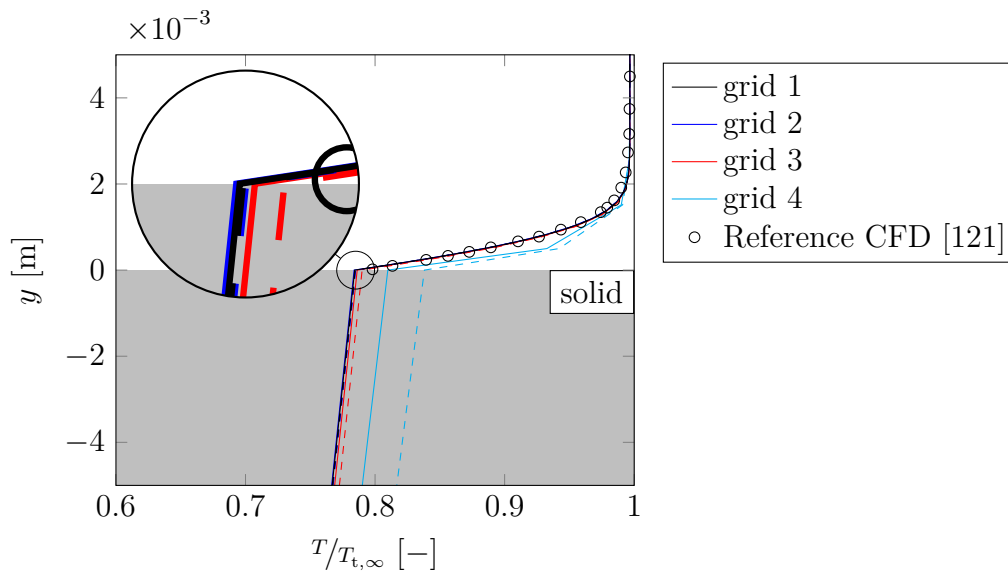
Figure 5.6: Influence of order of the numerical scheme of the interface for the flat plate case by Montomoli et al. [121] on different grids; First-order is shown in solid lines, second-order is shown in dashed lines

under-resolved with grid 4. Grid 1 and grid 2 produce very similar interface temperature which indicates grid convergence and shows that a non-dimensional wall distance of $y^+ \approx 1$ is sufficient.

The higher interface temperature with the second-order method is a result of the non-linear boundary layer temperature profile. Only the second-order method is sensitive to this non-linearity since it uses a three point stencil. The increasing difference between first- and second-order methods indicates that the non-linearity in the temperature distribution near the wall becomes more pronounced as the mesh resolution decreases. When the first cells are small enough, they are located entirely in the viscous sublayer [123], so first- and second-order gradient methods converge.

Interestingly, both first- and second-order methods overpredict the gradient on the coarser grids. Increasing the wall spacing places the first cells further into the hot external fluid, increasing their temperature and therefore the heat flux towards the wall. The second-order method amplifies this effect even more, which results in the higher interface temperature.

The external flow in typical hypersonic heating cases has a low static temperature but a high total temperature. Unlike the previous case, the temperature therefore has a maximum in the boundary layer. To test whether the choice of interface scheme affects these cases differently, the boundary layer simulation is performed at a hypersonic freestream velocity. Due to the relatively low total temperature, the gas is assumed to be calorically perfect also for the hypersonic case.

Similar to the incompressible case, the second-order boundary interface method produces a higher heat flux and therefore a higher interface temperature on all grids, see figure 5.7. A location $0.5\,\mathrm{m}$ downstream of the leading edge was used for extrac-
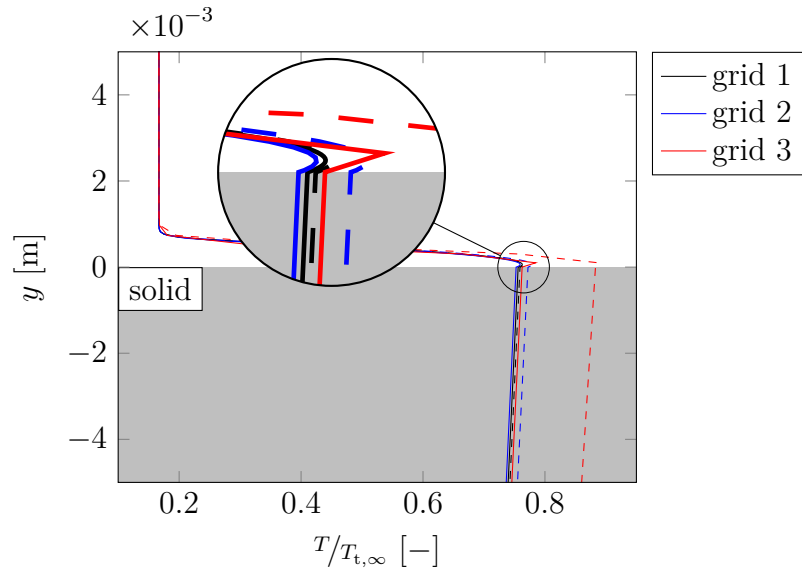
Figure 5.7: Influence of order of the numerical scheme of the interface for the flat plate case at hypersonic conditions; First-order is shown in solid lines, second-order is shown in dashed lines

tion. With the first-order scheme, interface temperature on grid 1 and grid 2 are similar, and the grid can be considered converged at $y^+ \approx 1$. With the second-order method, the difference between the results on grid 1 and 2 are significantly larger and only grid 1 seems to produce an accurate result. In general, the second-order methods is more sensitive to the mesh. While the variation of the interface temperature is 1.3% between grid 1 and grid 3 with the first-order method, it is 16.3% with the second-order method.

The initial expectation was that the second-order method would be more accurate and more robust on coarser grids. The flat plate cases show that it does not deliver in this respect and the first-order method is preferred. The likely reason is that the temperature distribution is linear in the viscous sublayer. On any grid with $y^+ > 1$, the first cell is outside the viscous sublayer and the physics of boundary layers are not reproduced accurately. Using the second-order method cannot fix this lack of resolution.

To test the two schemes in a case with non-linear temperature distribution in the viscous sublayer, a curved body is simulated. Here, the second-order method should improve the grid convergence. A hollow sphere in hypersonic flow at $\mathrm{Ma}_\infty = 7$ was chosen. Figure 5.8 shows the domain and temperature distribution for a steady state CHT simulation. Sea-level conditions were used for the freestream: $p_\infty = 101\,325\,\mathrm{Pa}$ and $T_\infty = 273.15\,\mathrm{K}$. Laminar flow was assumed for simplicity reasons. The sphere has a $5\,\mathrm{mm}$ outer radius and a $2\,\mathrm{mm}$ inner radius, its inner wall was isothermal at $T_{\mathrm{W_{inner}}} = T_\infty = 273.15\,\mathrm{K}$. Park's equilibrium model [38] was used for thermodynamic closure. For the material of the sphere, a generic heat-resistant steel was used with $\lambda = 15\,\mathrm{W/m\,K}$, $c = 469\,\mathrm{J/kg\,K}$, and $a = 4 \times 10^{-6}\,\mathrm{m^2/s}$. Sutherland's model [11] was used
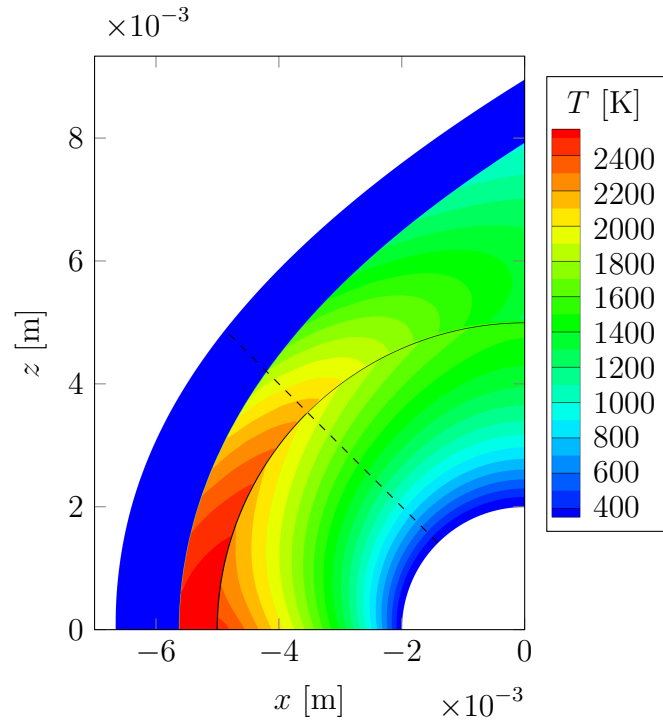
Figure 5.8: Domain of the CHT case of a hollow sphere in Ma = 7 flow; the edge of the solid domain is shown as a black line, the radial line used for extracting the data in figure 5.9 is shown as a dashed line

for the fluid viscosity.

Four different grids were generated, their properties are given in table 5.2. The same number of cells was used for all of them with 100 nodes in wall normal direction in the fluid and 50 nodes in the solid. A uniform distribution with 200 nodes was used along the body. The boundary layer was intentionally under-resolved with grid 4 to test the robustness of the methods.

Figure 5.9 shows the temperature distribution along the $45°$ radial line shown in figure 5.8. Note that the flow is supersonic outside the boundary layer along this line. The temperature was normalized with the total temperature in the freestream $T_{t,\infty} = 2950.02\,\mathrm{K}$. Similar to the flat plate case, the first-order method is much less grid-dependent, even on the under-resolved grid 4 acceptable accuracy is achieved.

grid	cell height fluid [m]	y^+ $[-]$
1	1×10^{-7}	0.38
2	2×10^{-7}	0.77
3	1×10^{-6}	3.84
4	5×10^{-6}	19.18

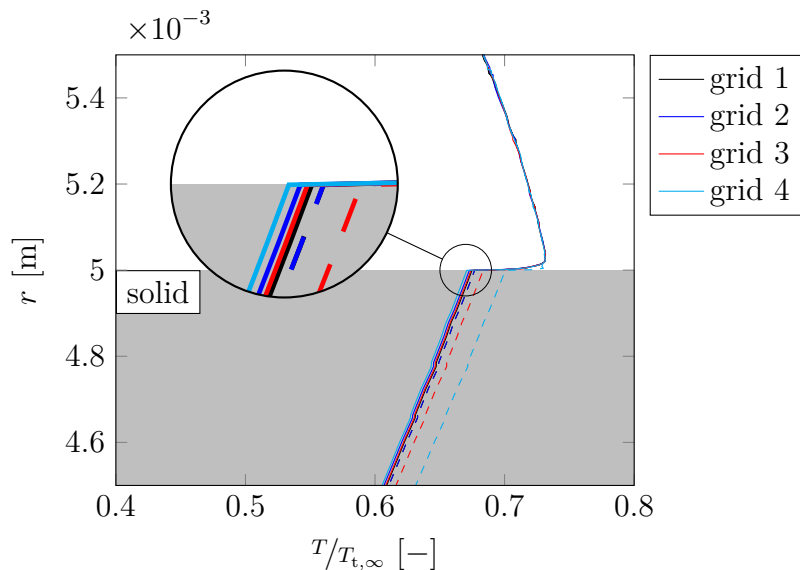Table 5.2: Grid properties for the hollow sphere CHT case

Figure 5.9: Normalized temperature distribution along a 45° radial line for the hollow sphere CHT case; First-order is shown in solid lines, second-order is shown in dashed lines

Comparing grids 1 and 2 shows that grid convergence is not quite reached for the given grids. This is likely due to the curvature in the temperature distribution in the boundary layer, which the first-order method cannot resolve accurately.

The second-order method again shows to be much less stable for coarser grids. Especially the solution on grid 4 is very inaccurate. Unlike with the first-order method, grid convergence is reached at grid 2. Refining the wall more does not change the temperature distribution noticeably. This highlights the advantage of the second-order method, which is able to predict the heat flux accurately, even for curved temperature distributions near the wall.

Overall, both the first- and second-order method can produce accurate results given appropriate grid resolution. Since the second-order method produces more severe errors when the applied grid is too coarse, the first-order method and its greater stability are preferred. The gains with respect to accuracy with the second-order interface method are minor in comparison to the errors on coarse grids.

5.2.2   Diffusive Wall Heat Flux

To test the importance of including heat transfer due to species diffusion, the composition of the wall heat flux at steady state for the hollow sphere case is analyzed. The first-order method for the interface was applied and the finest grid (grid 1) was used. Figure 5.10 a) shows the distribution of the wall heat flux along the surface coordinate s. The total heat flux and its components, the conductive part in the fluid and the part due to species diffusion are also shown separately. In this particular case, the diffusion heat flux is only relevant near the stagnation point, where
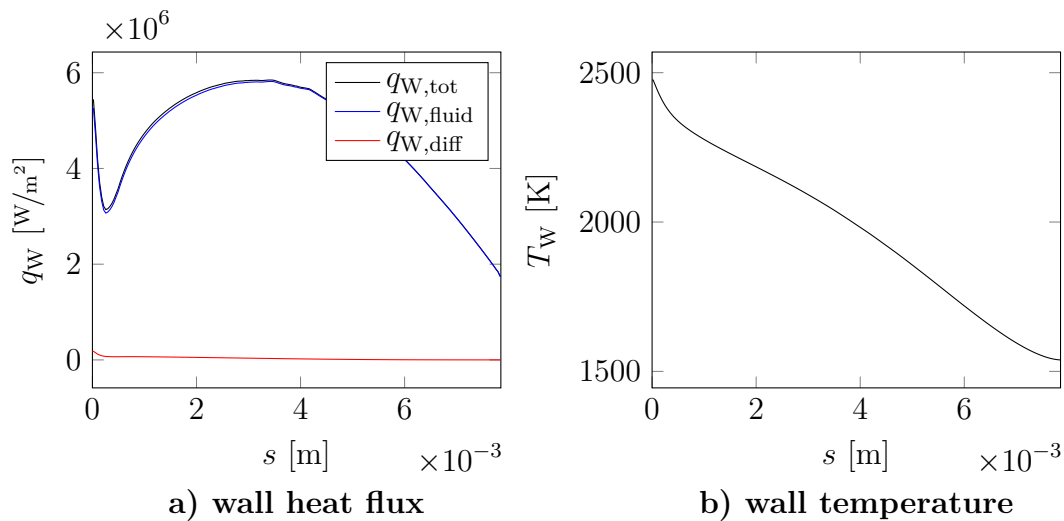
Figure 5.10: Heat flux and temperature distribution along the hollow sphere

$q_{W,diff}/q_{W,fluid} \approx 3.5\%$. The ratio then drops rapidly, see figure 5.11. This is partly due to the moderate temperatures at $Ma_\infty = 7$ and partly due to the applied equilibrium model. As noted in section 2.2.1, in an equilibrium model, chemical reactions are assumed to be significantly faster than the flow processes, which reduces species concentration gradients.

Interestingly, the heat flux distribution in figure 5.10 a) is qualitatively different compared to a typical isothermal body [32]. For comparison, the wall heat flux distributions using CHT walls and isothermal walls with $T_W = 273.15\,\mathrm{K}$ along the sphere is shown in figure 5.12. Due to the increased surface temperature, the absolute value of the heat flux is much lower in the CHT case. While both wall models have a secondary local heat flux maximum due to turbulence onset, the relative magnitude of the second maximum compared to the stagnation point heat flux is significantly higher in the CHT case. The maximum is also shifted downstream: in the isothermal case, it is located $1\,\mathrm{mm}$ from the stagnation point, in the CHT case it is around $3.3\,\mathrm{mm}$ from the stagnation point.

The temperature distribution in figure 5.10 b) also does not correlate with the adiabatic wall temperature distribution over a spherical nose [125]. The wall heat flux distribution in the CHT simulation is not similar to the isothermal case, and similarly the wall temperature distribution is not similar to the adiabatic case. Both distributions are distinctly different in the CHT result due to the non-uniform heating of the solid and solid heat flux in circumferential direction.
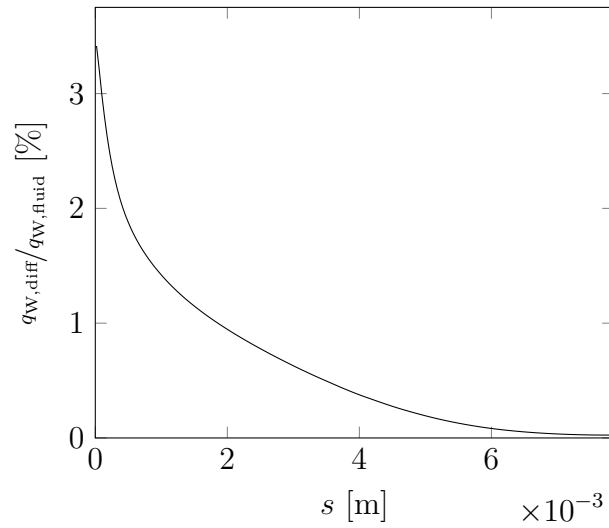
Figure 5.11: Ratio of the heat flux due to species diffusion to the conductive heat flux for the hollow sphere CHT case
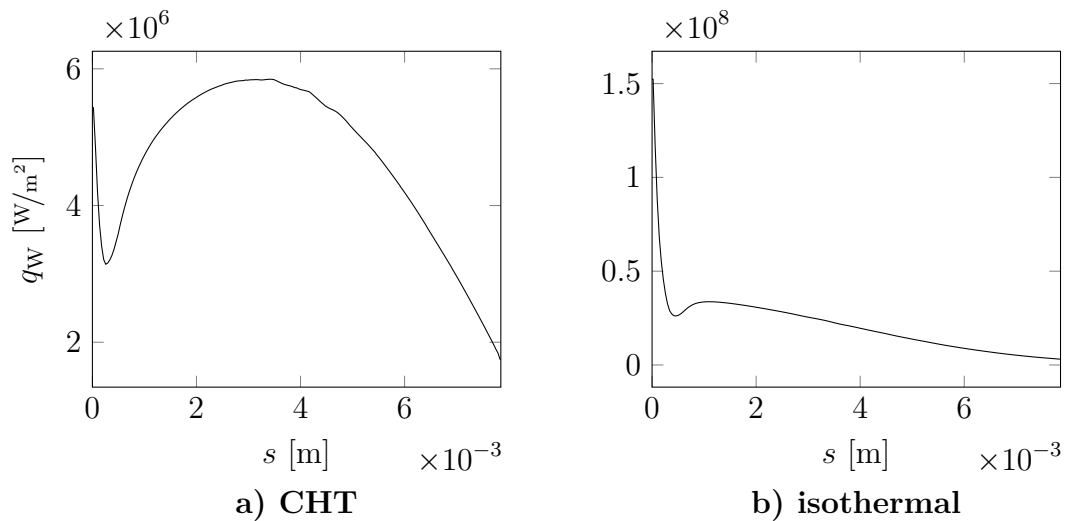

Figure 5.12: Comparison of the wall heat flux along the hypersonic sphere body using a CHT wall or an isothermal wall with $T_\mathrm{W} = 273.15\,\mathrm{K}$

5.3 STBLI-Induced Heating

Neither of the turbulent heat flux models was able to reproduce the experimental data by Schülein in section 5.1.2. The experimental heat flux data by Schülein [126] was measured with their 'thin-skin technique'. A thin, well isolated layer of a material with high thermal conductivity is placed on the wall. When spacial temperature variation can be neglected, the energy balance of the layer simplifies to

$$q_{\mathrm{W}} = \rho c h \frac{\mathrm{d}T_{\mathrm{W}}}{\mathrm{d}t}, \tag{5.2}$$

where h is the height of the solid layer. Schülein [126] used a nickel layer with $h = 0.2\,\mathrm{mm}$, $\rho = 8900\,\mathrm{kg/m^3}$, and $c = 458\,\mathrm{J/kg\,K}$. The thermal conductivity of $\lambda = 94\,\mathrm{W/m\,K}$ was taken from [41].

Using eq. (5.2) and the duration of the measurement of $130\,\mathrm{ms}$, a maximum temperature increase of $7.38\,\mathrm{K}$ in the interaction region is found for the experimental heat flux data. Given that the maximum temperature in the flow field is just over $330\,\mathrm{K}$ a surface temperature increase of this magnitude could affect the wall heat flux significantly.

An unsteady coupled simulation of the STBLI case with the thin nickel layer was conducted. The domain was initialized with a steady state result with a constant wall temperature of $T_{\mathrm{W}} = 300\,\mathrm{K}$. The nickel layer was initially at the same temperature.

Figure 5.13 shows the evolution of the surface temperature for the coupled simulation. Over the course of the experimental measuring time of $130\,\mathrm{ms}$, a maximum temperature increase of just under $8\,\mathrm{K}$ is observed in the interaction region, which matches the theoretically expected value well. The main heating areas are the tip of the plate ($x = 0\,\mathrm{m}$) and the interaction region $x > 0.34\,\mathrm{m}$, while the plate upstream of the impinging shock experiences only minor heating. Due to the increasing wall temperature, the wall heat flux decreases.

The evolution of the wall temperature and wall heat flux over time is shown in figure 5.14. The temperature increase in plot a) is approximately linear in time. Due to the high heat flux, the temperature increases fastest in the interaction region and at the tip of the plate. The wall heat flux plot b) confirms the expectation that the surface heating changes quite noticeably during the experimental measuring time. To evaluate the accuracy of the numerical method, the average relative deviation from the experimental data [126] was computed:

$$\overline{\Delta q_{\mathrm{W}}} = \frac{1}{x_{\max} - x_{\min}} \int_{x_{\min}}^{x_{\max}} \frac{\left| q_{\mathrm{W,num}} - q_{\mathrm{W,exp}} \right|}{q_{\mathrm{W,exp}}}\,\mathrm{d}x, \tag{5.3}$$

where $x_{\min}$ is the start of the interaction region at $0.34\,\mathrm{m}$ and $x_{\max}$ is the end of the domain at $0.5\,\mathrm{m}$. To compute the deviation, the experimental data was interpolated onto the numerical grid, a linear distribution was assumed between the discrete experimental values. At the start of the CHT simulation, the deviation is $\overline{\Delta q_{\mathrm{W}}} = 19.1\%$, which reduces to $\overline{\Delta q_{\mathrm{W}}} = 10.4\%$ at the end of the CHT simulation ($t = 130\,\mathrm{ms}$).
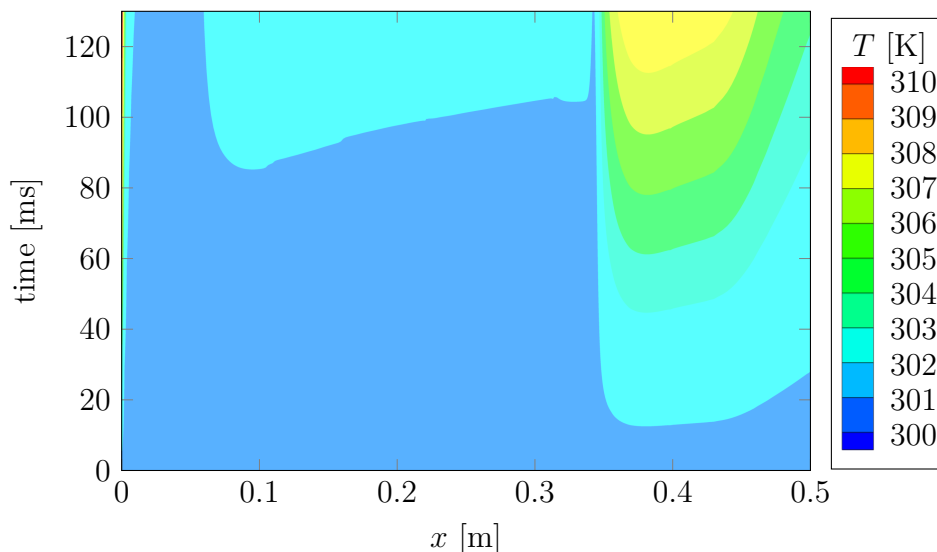
Figure 5.13: Evolution of the surface temperature in the STBLI case by Schülein [126]; numerical simulation of their thin-skin technique

Overall the agreement to the experimental data is much better after 130 ms with especially good agreement in the second half of the interaction region $x > 0.41$ m.

The overprediction of the wall heat flux in the numerical results seems to be partly due to the way the experimental data were measured and reported, which neglect the influence of the increasing wall temperature on the surface heat flux. Schülein [126] states that the experimental measuring time of 130 ms was chosen because the surface temperature increase was linear, e.g., $\mathrm{d}T_{\mathrm{w}}/\mathrm{d}t = $ const, which, according to the author, gives a constant heat flux. The numerical findings in figure 5.14 show that, as the surface temperature varies in time, the wall heat flux decreases considerably.

These results highlight the necessity of CHT simulations even for the reproduction short-duration experiments. Numerical models that are able to reproduce the experimental data exactly would underpredict the occurring heat flux in the more realistic CHT case. It should be noted, however, that the thin-skin approximation in eq. (5.2) relies on the assumption of adiabatic walls on all sides of the nickel plate except for the fluid-facing one. Realistically, heat flux to the sides and especially towards the bottom would affect the measurements. Since no detailed information about the mounting of the nickel plate is given in [126], a more accurate numerical model could not be used The numerical results show the limits of the thin-skin technique for heat flux prediction, which overpredicts the heat flux due to the changing wall temperature.

5.4 Aerodynamic Heating of a Generic Flap

As mentioned in the introduction and shown in this chapter, there exists a mutual influence between the thermal state of the wall and the external flow. This becomes
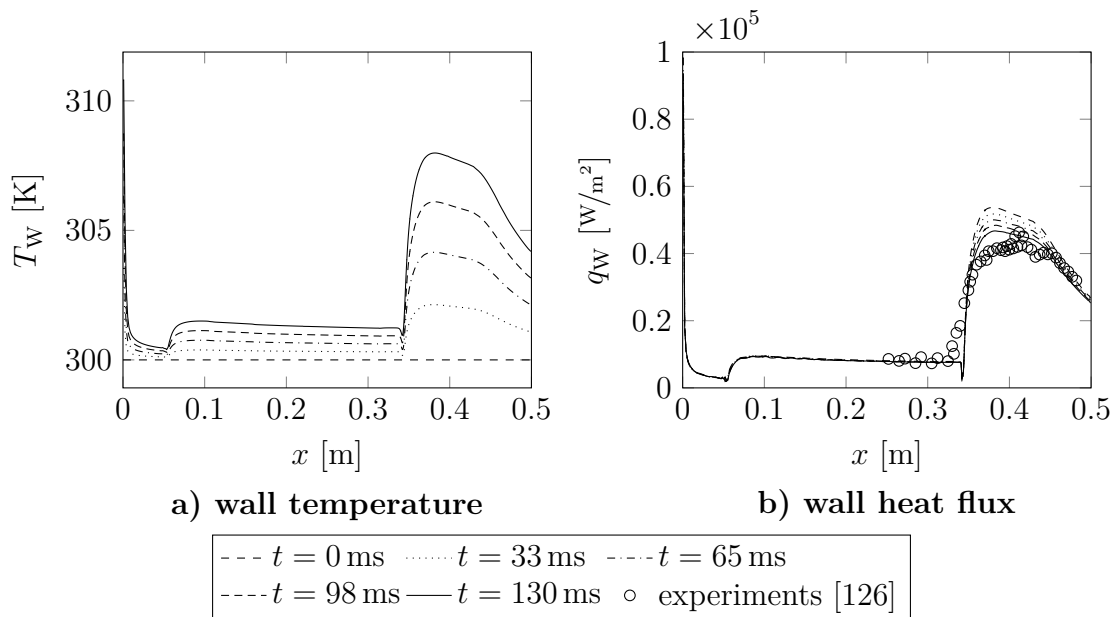
Figure 5.14: Wall data of the CHT simulation of the STBLI case by Schülein [126]

especially important in regions with high heat load, where the surface temperature is expected to change strongly. In addition to the ability to withstand the heat load, it is also crucial for sustained hypersonic flight that aerodynamic control surfaces remain effective during flight.

As a final test case, a generic flap-type control surface is analyzed with the CHT method. It includes all the relevant physical phenomena (shock/boundary layer interaction, high-temperature effects, diffusion heat flux) and poses one of the more challenging problems of high-speed flight. Figure 5.15 shows the geometry of the 2D version of the generic flap case. It consists of a blunt nose, followed by a 150 mm flat plate section. The flap itself has a length of 50 mm and a variable angle of $\alpha = 20, 25, 30°$. Three different nose radii were compared: $r_n = 1, 2, 5$ mm. The thickness of the forebody was chosen as $r_n/2$ and varied with the nose radius.

This case is similar to the flap investigated by Exposito et al. [8]. Some changes were made, however, to make it more relevant as a test case for a realistic control surface. In their setup, the forebody has a relatively short length of 80 mm, with a 100 mm ramp. Firstly, this is not representative of the proportions of a real control surface, where the flap would generally be much shorter than the forebody. Secondly, the bow shock impinges on the flap in their geometry. For a real control surface, this should be avoided in the vehicle design since it generates strong local heating and increases the sensitivity regarding the freestream. Finally, their geometry uses very small nose radii (0.02 mm and 0.1 mm) that are not representative of real geometries. In the chosen configuration, these issues are addressed with a larger nose radius, longer forebody, and shorter flap, which eliminates shock impingement on the flap.

Based on a review of past and present hypersonic vehicle projects [13, 127, 128] and the available data of the future projects by Hermeus [129] and Destinus [130], rep-
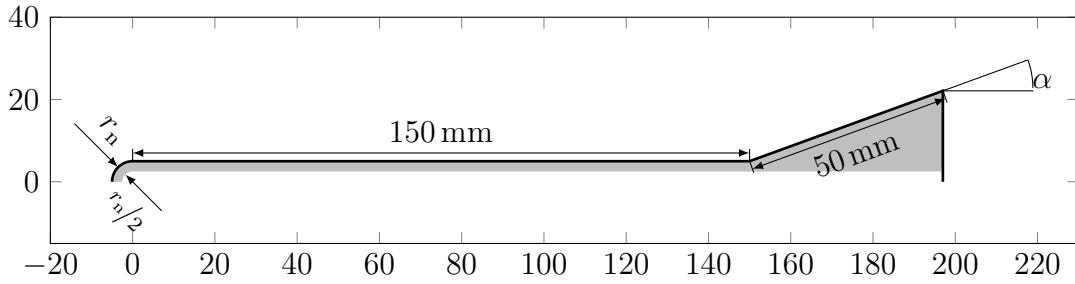
Figure 5.15: Geometry of the 2D version of the generic flap case

grid	total cells	nodes along flap	wall normal nodes
1	38 609	80	109
2	49 329	120	109
3	65 969	120	149
4	71 889	120	149
5	85 569	120	179

Table 5.3: Grid properties of the 2D generic flap case

resentative freestream conditions were chosen. The resulting conditions are $\mathrm{Ma}_\infty = 7$ at an altitude of 30 km. Using the US 1976 standard atmosphere model [10], the remaining parameters are computed: $p_\infty = 1171.87\,\mathrm{Pa}$ and $T_\infty = 226.65\,\mathrm{K}$, which results in a unit Reynolds number of $\mathrm{Re}_{\infty,1} = 2.557 \times 10^6\,\mathrm{1/m}$.

Turbulence is modeled with the Wilcox $k - \omega$ model, the turbulence heat flux is treated with the RPS model. The fluid is treated as equilibrium air with the model by Park, Sutherland's model is used for the viscosity. To improve convergence, the mesh is adapted to the bow shock. Unless otherwise noted, a generic heat-resistant steel is used with a thermal diffusivity of $a = 5.8 \times 10^{-6}\,\mathrm{m^2/s}$, a specific heat capacity of $c = 440\,\mathrm{J/kg\,K}$ and a thermal conductivity of $\lambda = 20\,\mathrm{W/m\,K}$. Where applicable, an emissivity of $\epsilon = 0.8$ was used.

A grid study was conducted with the largest nose radius (5 mm). Table 5.3 shows the properties of the four grids. Using grid 1 as a baseline, the number of nodes along the flap was increased for grid 2. For grid 3, the number of cells in wall normal direction was increased and for grid 4, the number of cells along the flat plate upstream of the flap was increased from 100 to 140. For grid 5, the number of wall normal cells was increased further. Since the previous results in section 5.2.1 already showed that a wall spacing of $y^+ < 1$ is necessary to obtain accurate results with the CHT method, a block with 30 nodes was placed along the wall for all grids. The resulting wall distance is 0.008 mm at the start of the flap which gives $y^+_{\max} \approx 0.75$ on the flap.

The separation length is used to choose an appropriate grid. Due to the reverse flow, the separation region is characterized by the axial wall shear stress $\tau_{\mathrm{W},x} = \mu^{\partial \tilde{u}_x/\partial n}|_{\mathrm{W}} < 0$. Figure 5.16 shows $\tau_{\mathrm{W},x}$ in the separated region, with the
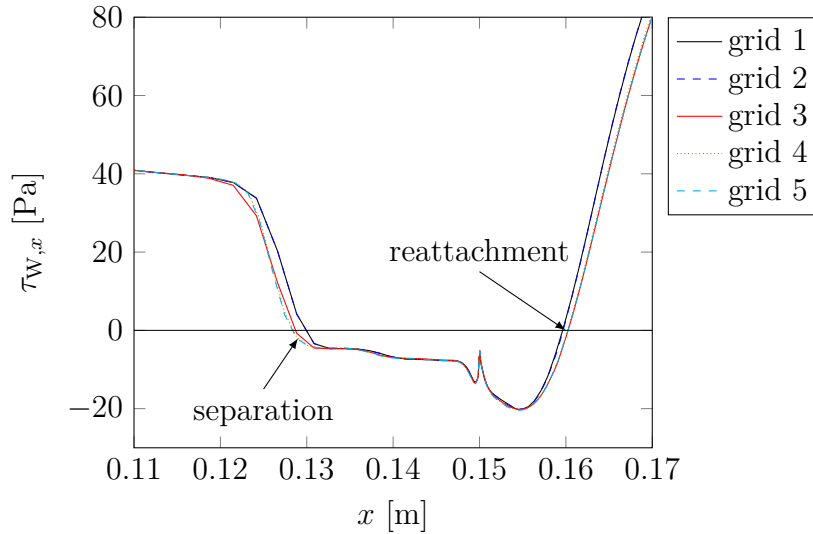
Figure 5.16: Axial wall shear stress in the separated region at the start of the 2D flap for the grids given in table 5.3

flap starting at $x = 0.15\,\text{m}$. The separation is captured similarly on all grids with only minor changes in separation length. With grids 1 and 2 and grids 3 and 4 being very similar, the separation seems to be most sensitive to the number of cells in wall normal direction. The increase of wall normal cells in grid 5 does not change the results drastically, however, so grid convergence can be assumed for grid 4.

5.4.1 Influence of Nose Radius

First simulations of the fluid domain without coupling were conducted. Figure 5.17 a) shows the wall heat flux of the isothermal wall with $T_\text{W} = T_\infty$ along the nose of the body over the normalized surface coordinate s/r_n for the three nose radii. All cases have a similar scaled shock standoff distance of $(x_\text{shock} - x_\text{stag})/r_\text{n} \approx 0.37$, but when the nose radius is decreased, the absolute distance between the shock and the stagnation point decreases. The resulting temperature gradients in the shock layer are larger and the wall heat flux is increased. This increases the temperature gradient in the shock layer and the wall heat flux.

In figure 5.17 b) the wall heat flux near the flap is shown over the absolute coordinate x. Even though the heat flux upstream of the separation region is nearly identical with all nose radii, the heat flux on the flap differs strongly. There is an increase of the wall heat flux with smaller nose radii. The plot also shows how the separation location moves upstream as the nose radius is decreased.

For analyzing the reason for the effects shown in figure 5.17 b), it is useful to investigate the entropy change in the flow. The entropy change from the freestream to any point $\boldsymbol{x}$ in the field can be computed using the following equation:

$$\Delta s = s(\boldsymbol{x}) - s_\infty = \int_\infty^{\boldsymbol{x}} \frac{c_p}{T}\,\text{d}T - \int_\infty^{\boldsymbol{x}} \frac{R}{p}\,\text{d}p\,. \tag{5.4}$$
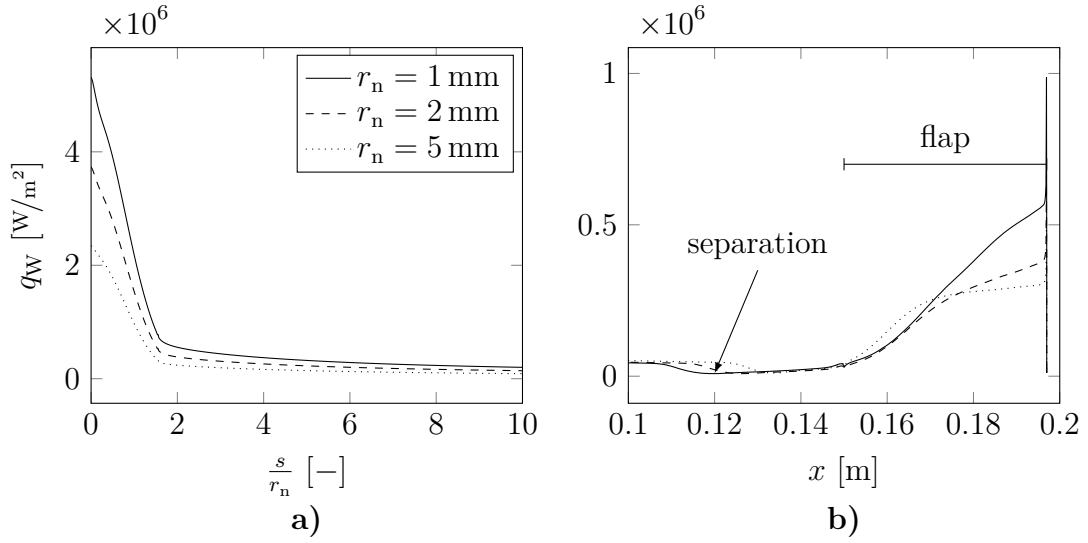
Figure 5.17: Wall heat flux on the $\alpha = 20°$ flap for different nose radii

For a perfect gas, this can be simplified to

$$\Delta s = s(\boldsymbol{x}) - s_\infty = c_p(\boldsymbol{x}) \ln \left(\frac{T(\boldsymbol{x})}{T_\infty} \right) - R(\boldsymbol{x}) \ln \left(\frac{p(\boldsymbol{x})}{p_\infty} \right). \tag{5.5}$$

Since the solution of eq. (5.4) requires the integration along streamlines, the simpler approximation of eq. (5.5) was used even for the non-perfect gas in the current flow.

The entropy variation defines the entropy layer around the body, i.e., the region in the flow field that is influenced by the curved section of the bow shock. Figure 5.18 shows the entropy change around the $\alpha = 20°$ body. As the nose radius is increased, the shock moves further away from the body. More importantly, however, the region that is affected by the shock curvature increases with nose radius. Due to this, the region with large entropy variation increases in size compared to the size of the flap. While the resulting height of the entropy layer is smaller than the height of the flap for $r_\mathrm{n} = 1\,\mathrm{mm}$, the entire flap is inside the entropy layer for $r_\mathrm{n} = 5\,\mathrm{mm}$.

Since this variation in entropy distribution is an effect of the temperature and pressure distribution, the effective inflow conditions upstream of the flap are affected. This impacts the size of the separation bubble at the flap. Figure 5.18 shows qualitatively that the thicker entropy layer at larger nose radii has a stabilizing effect and reduces separation size. This can be seen as a downstream shift of the separation location from $x \approx 0.11\,\mathrm{m}$ at $r_\mathrm{n} = 1\,\mathrm{mm}$, to $x \approx 0.12\,\mathrm{m}$ at $r_\mathrm{n} = 2\,\mathrm{mm}$, and $x \approx 0.13\,\mathrm{m}$ at $r_\mathrm{n} = 5\,\mathrm{mm}$.

The steady state CHT method was also used to investigate the influence of the nose radius on the material heating. Figure 5.19 shows the wall temperature a) and wall heat flux b) along the surface of the 20° flap for the three nose radii. Firstly, the stagnation temperature decreases with the nose radius because the thickness of the material $r_\mathrm{n}/2$ also scales with the nose radius and the inside of the solid wall is isothermal at T_∞. Due to the lower wall temperature and the reduced shock standoff
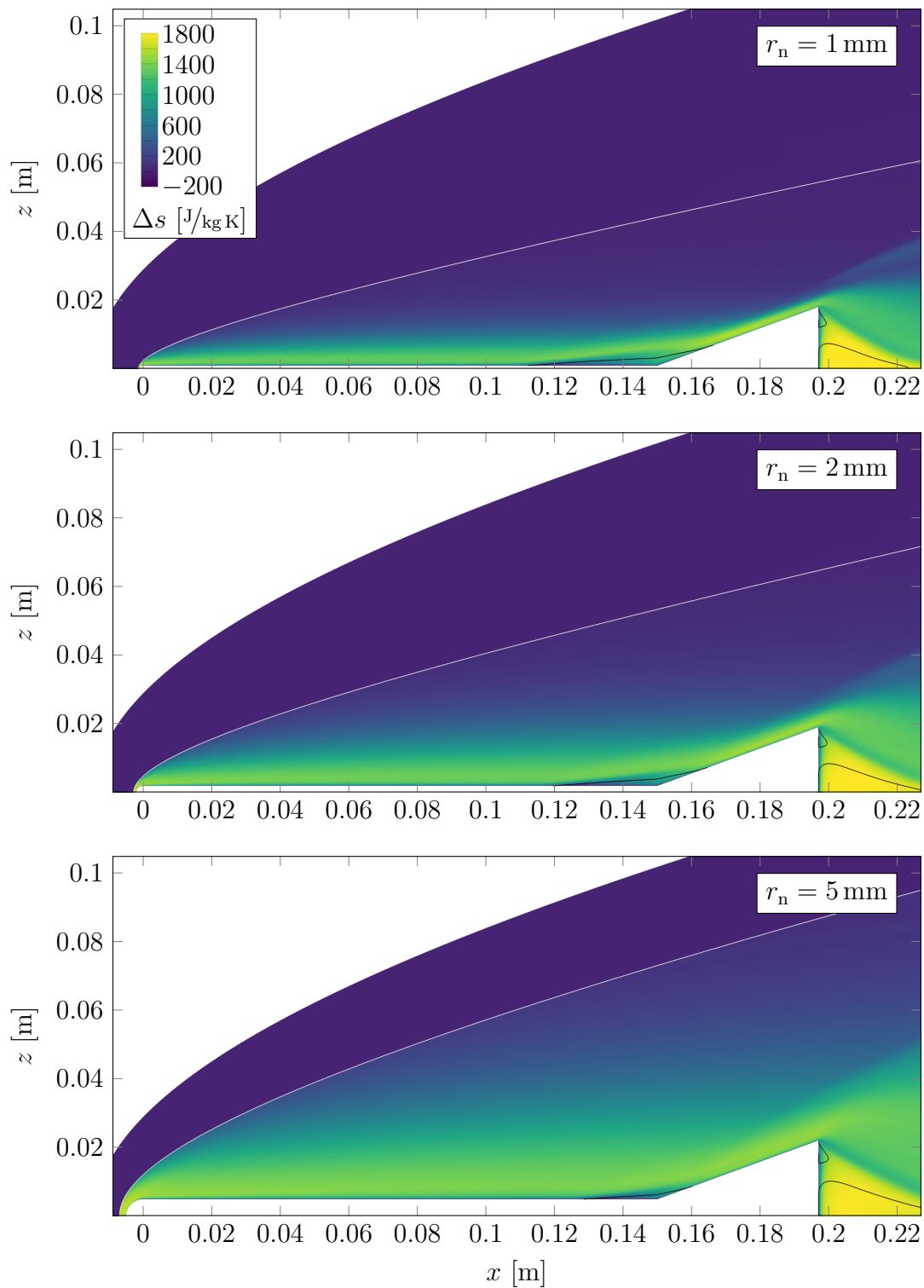
Figure 5.18: Entropy variation around the $\alpha = 20°$ 2D flap at different nose radii, the black line marks the edge of the separated region with $u_x = -0.001\,\mathrm{m/s}$ and the white line follows the shape of the bow shock
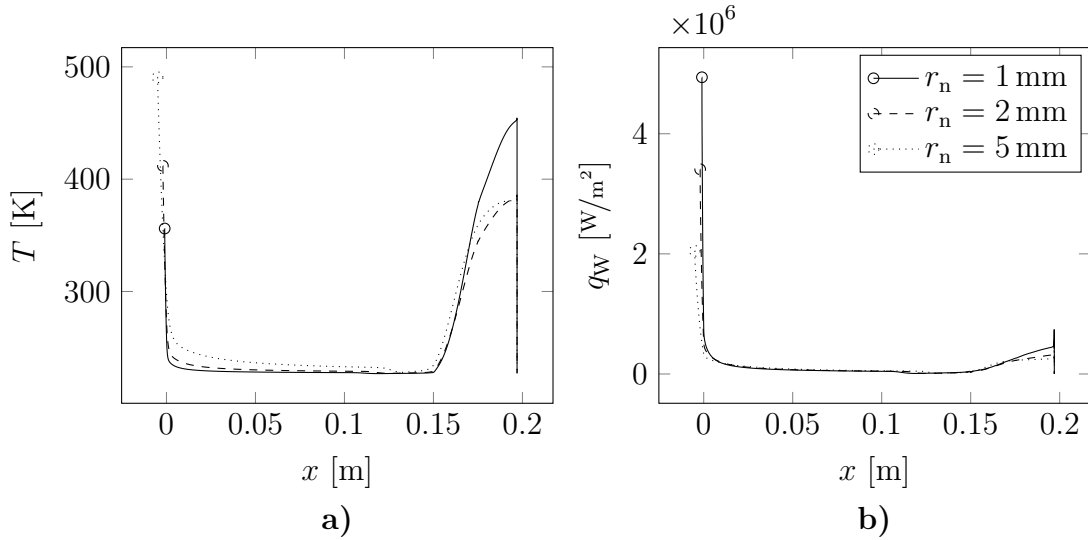
Figure 5.19: Temperature and heat flux along the 20° steady 2D coupled flap, the markers emphasize the stagnation point values

distance, the nose heat flux increases as the nose radius is decreased.

In the region of the flap, however, the temperature with $r_n = 1\,mm$ is significantly higher than with the two larger radii. It reaches a maximum at the tip of the flap of $T \approx 454\,K$ for $r_n = 1\,mm$ and $T \approx 380\,K$ for $r_n = 2\,mm$ and $r_n = 5\,mm$. At the flap, the variation of the material thickness with the nose radius is of secondary importance. The high temperature at the smallest nose radius is mainly a result of the entropy layer shown in figure 5.18. While the entropy layer has a similar thickness as the flap for the two larger radii, it is significantly thinner than the flap with the smallest radius. Thus, the flap at $r_n = 1\,mm$ is more exposed to fluid outside the entropy layer. The low wall temperature of the $r_n = 2\,mm$ case can likely be explained by the thinner flap material compared to the largest radius.

Due to the effect of the entropy layer, the temperature on the flap is higher than the stagnation temperature for the smallest nose radius. Depending on the geometry of the body, a variation of the nose radius may therefore move the region with the highest temperature from the nose to other parts of the body.

The higher wall temperature in the CHT case also affects the shock-induced separation. Figure 5.20 shows the x-component of the wall shear stress. When the hotter CHT wall is used, the separation moves further upstream and the reattachment location moves further downstream. The larger the nose radius, the bigger the difference between the isothermal and CHT wall, since the solid body is thicker in the forebody.

These trends match the findings of Brown et al. [7] and Exposito et al. [8], who showed that laminar separation length increases with wall temperature. This effect may be explained by the lower density in the boundary layer at higher wall temperatures which results in a thicker boundary layer. Due to that, velocity gradients are smaller and the required pressure gradient for critical dilatation is decreased, resulting in a longer separation bubble.
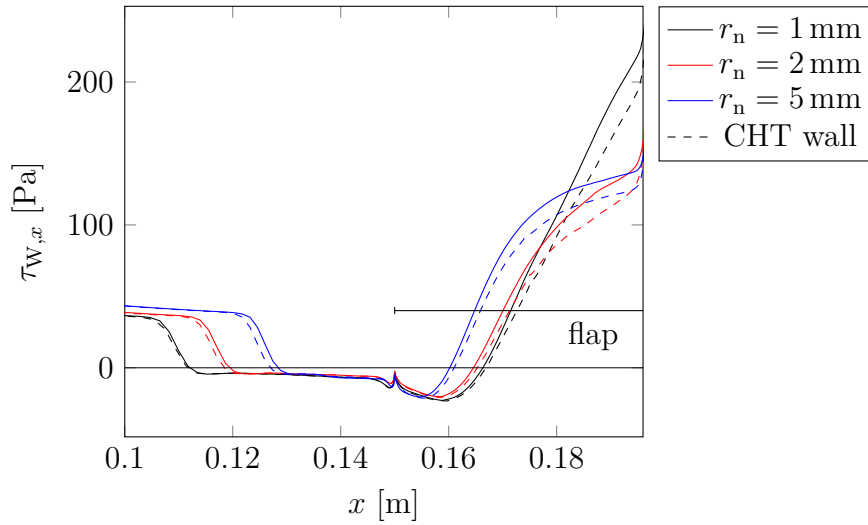
Figure 5.20: Wall shear stress along the 2D 20° flap with isothermal (solid lines) and CHT walls (dashed lines)

Analogous to the wall temperature and heat flux data, the walls shear stress near the tip of the flap is very similar between the two larger radii, while the smallest radius results in significantly higher shear stress on the flap. Again, this can be explained by the thinner entropy layer for the smaller radius, that exposes the flap to faster external flow.

5.4.2 Influence of the Flap Angle

Three different flap angles were simulated: $\alpha = 20°, 25°, 30°$. In figures 5.21 to 5.23, the temperature distribution for the coupled steady state simulations with the three nose radii are shown. As the flap angle increases, the oblique shock becomes stronger and the size of the separation increases. The effect is visible for all nose radii, but it is most pronounced for $r_n = 1\,\mathrm{mm}$, where it moves upstream to $x \approx 0.06\,\mathrm{m}$. Similarly, the reattachment point moves downstream as the flap angle is increased. Again this trend is more pronounced the smaller the nose radius is.

This upstream shift of the separation and the separation shock also affects the thermal state of the incoming fluid in front of the flap. The separation shock deflects fluid away from the wall and therefore increases the thickness of the entropy layer. As the separation shock moves forward, the resulting hot layer covers more of the flap, resulting in a higher temperature inside the flap.

The resulting temperature distribution on the surface of the body is shown in figure 5.24 For $r_n = 5\,\mathrm{mm}$, the flap temperature increases with flap angle. For $r_n = 2\,\mathrm{mm}$, the flap temperature increases from $\alpha = 20°$ to $\alpha = 25°$, but no notable temperature increase is observed, at the largest angle. For the smallest nose radius, that trend continues, and the maximum temperature is observed at the intermediate flap angle. The reason for this behavior might be strong increase of the separation

Figure 5.21: Temperature distribution in the fluid and solid domains for the $r_\mathrm{n} = 1\,\mathrm{mm}$ 2D flap at the three flap angles; The black line marks the edge of the separation bubble with $u_x = -0.001\,\mathrm{m/s}$

Figure 5.22: Temperature distribution in the fluid and solid domains for the $r_n = 2\,\text{mm}$ 2D flap at the three flap angles; The black line marks the edge of the separation bubble with $u_x = -0.001\,\text{m/s}$
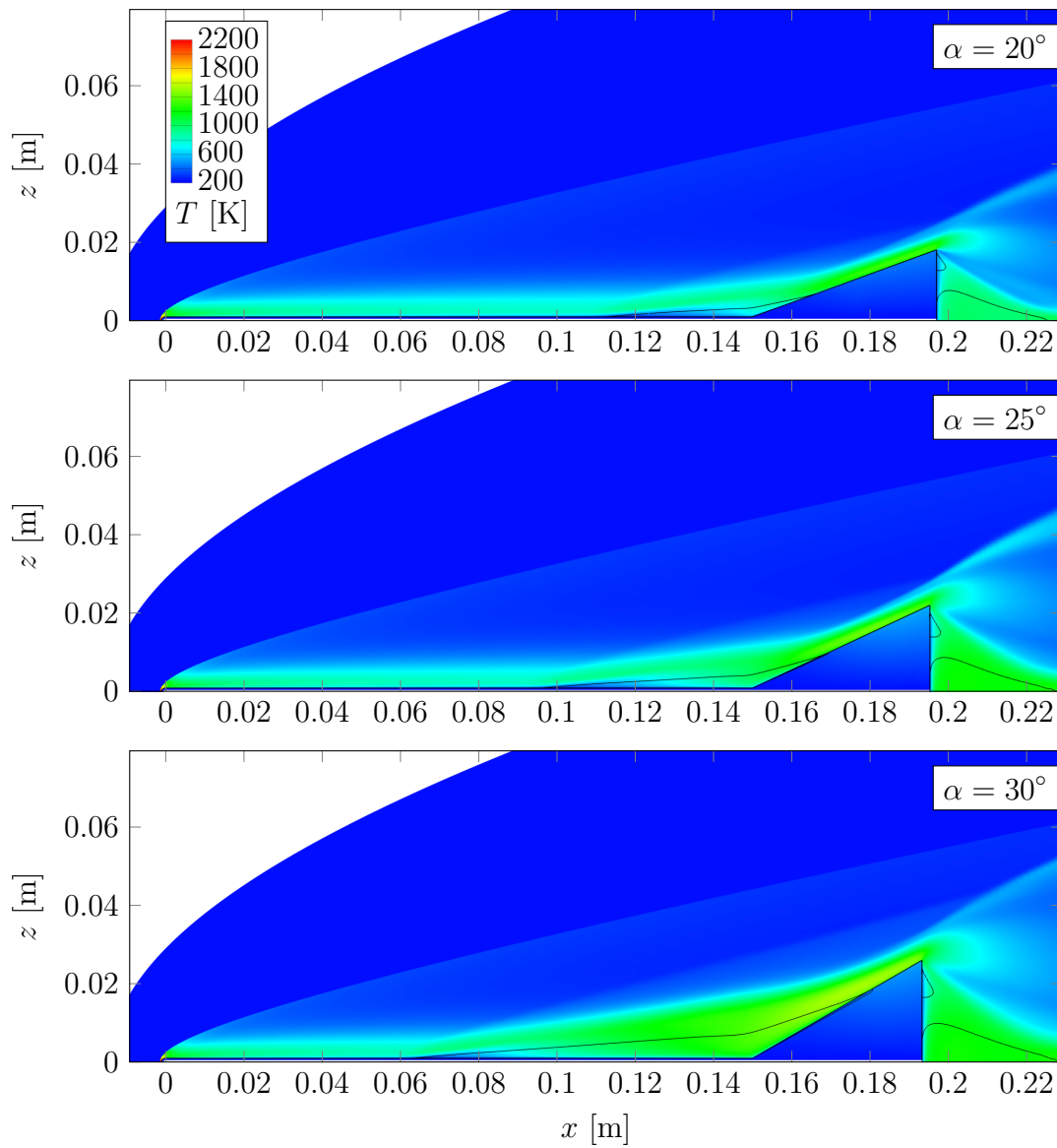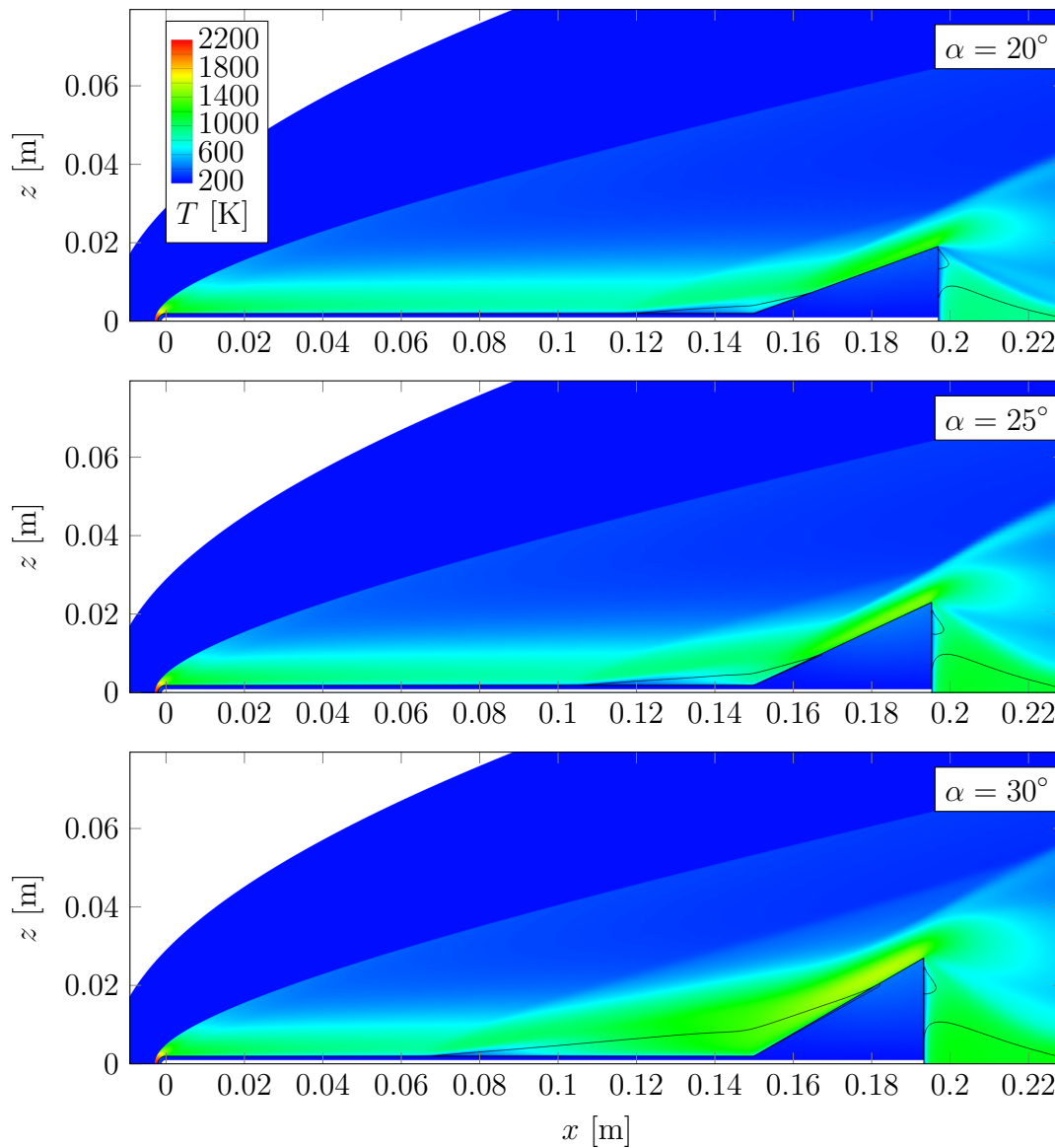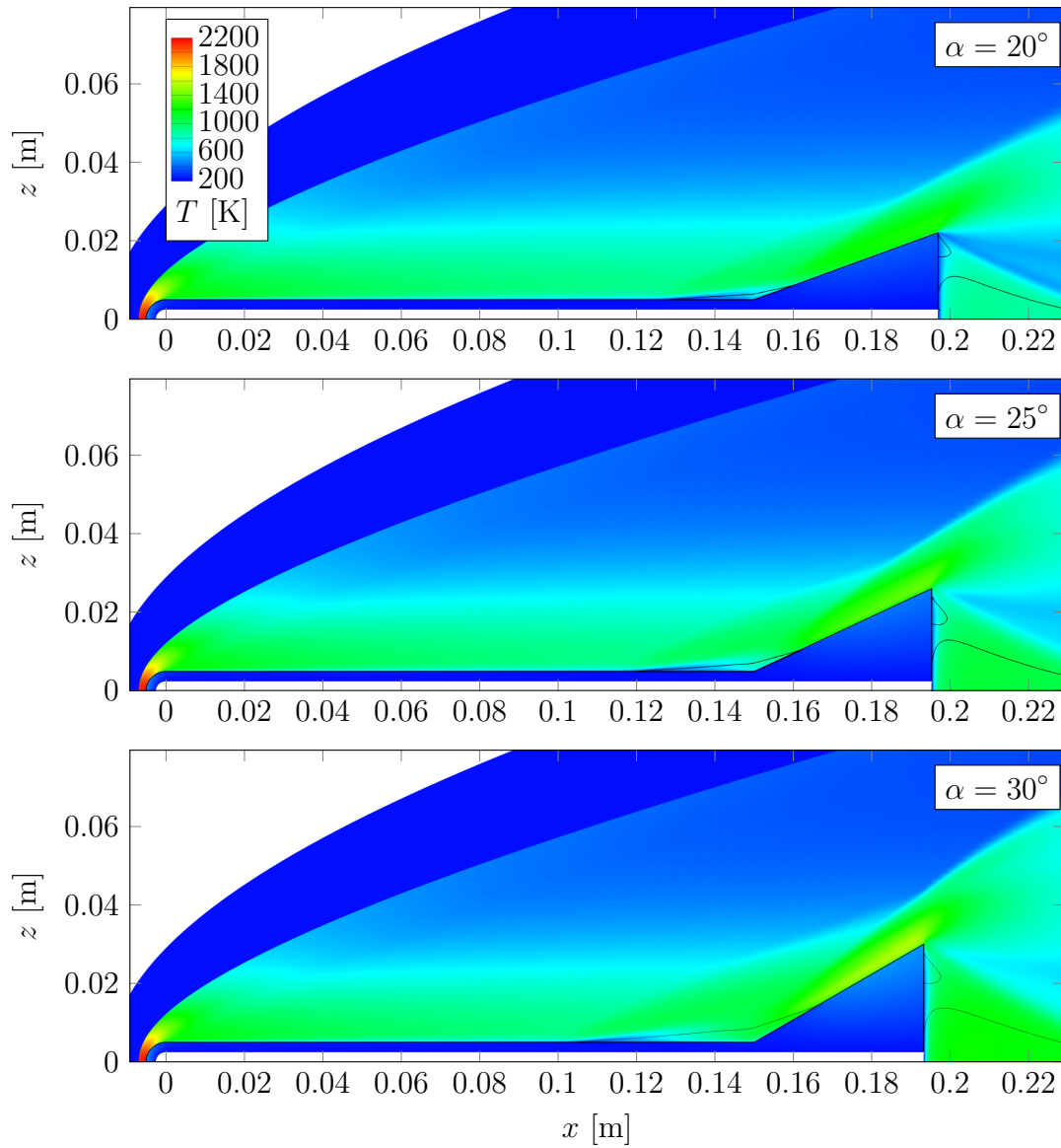
Figure 5.23: Temperature distribution in the fluid and solid domains for the $r_\mathrm{n} = 5\,\mathrm{mm}$ 2D flap at the three flap angles; The black line marks the edge of the separation bubble with $u_x = -0.001\,\mathrm{m/s}$
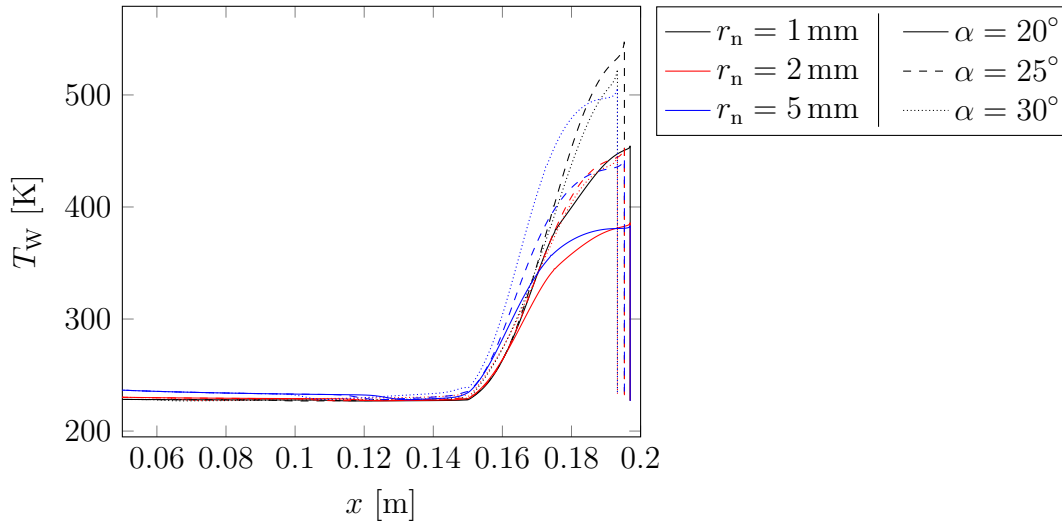
Figure 5.24: 2D flap surface temperature in the coupled simulation at the different nose radii and flap angles

size with small nose radii and large flap angles, which result in a larger distance between the separation shock and the flap.

Due to the strong increase of the separation size for the smaller nose radii, a larger nose radius is generally favorable in the design of new hypersonic vehicles. The smaller separation bubble should reduce the sensitivity of the aerodynamic properties and make the vehicle better to control. The present investigation shows that a thorough CHT analysis is required to identify problematic vehicle configurations.

5.4.3 Transient Heating Effects

To investigate the effect of the changing solid temperature during a transient heating process, unsteady coupled simulations of the 2D flap were conducted. An adiabatic boundary condition was used for the inner wall of the solid body and simulations were started from a developed flow field with a solid temperature of $T_\infty = 226.65\,\text{K}$. The solid timescale was reduced by $c_{\text{ET}} = 10\,000$. The surface temperature and axial shear stress distribution are shown in figure 5.25. The temperature increases drastically along the nose of the body, especially in the first $10\,\text{s}$ of the simulation. Along the flap, a non-uniform temperature increase can be seen. In contrast to the coupled steady state simulations, that result in a monotonically increasing flap temperature along x, a local temperature maximum occurs in the middle of the flap. In the separated region, the heat flux is lower and the material heats up more slowly.

Due to the higher temperature, the shear stress distribution is affected. Similar to the observations for the isothermal and steady CHT walls in figure 5.20, the separation length increases over time as the surface temperature increases. This again proves the relevance of CHT simulations, since the aerodynamic properties depend on flow separation. Note that flap angles 25° and 30° were also investigated
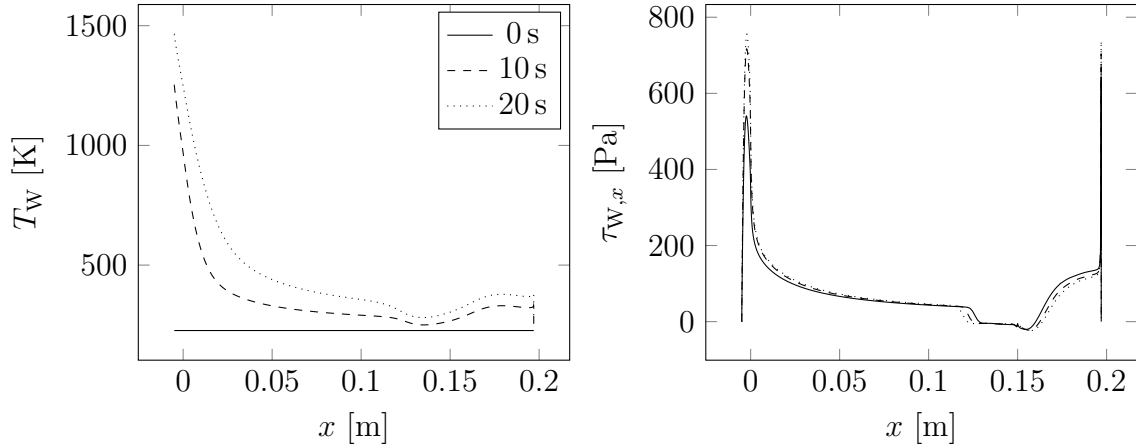
Figure 5.25: Transient heating of the $r_\mathrm{n} = 5\,\mathrm{mm}$ $20°$ flap: wall temperature and shear stress at different time increments

Coefficient	a	λ	c
c_1	0.24248E-18	0.15642E-11	0.58825E-11
c_2	-0.63730E-15	-0.45781E-08	-0.22000E-07
c_3	0.61378E-12	0.51987E-05	0.33358E-04
c_4	-0.26260E-09	-0.28650E-02	-0.24433E-01
c_5	0.45175E-07	0.78100E+00	0.89046E+01
c_6	0.43307E-05	-0.62269E+02	-0.77103E+03

Table 5.4: Polynomial coefficients for the variable material properties

and showed an analogous result.

5.4.4   Effect of Variable Material Properties

As described in chapter 2, properties of solid materials may change with temperature. To assess the impact of this effect, a specific heat-resistant steel (X 11 CrMo 9-1) was chosen from [41]. At room temperature, it has similar properties to the generic heat-resistant steel used in the rest of the investigations. Using the least-squares fit the coefficients of the fifth-order polynomial

$$\phi = c_1 T^5 + c_2 T^4 + c_3 T^3 + c_4 T^2 + c_5 T + c_6 \tag{5.6}$$

are found. They are given in table 5.4, units are omitted for clarity.

The $20°$ flap with the three different nose radii was simulated with these variable material properties. Figure 5.26 shows the surface temperature distribution for constant and temperature-dependent material properties. The thermal conductivity of the chosen material increases with temperature, which results in a reduction of surface temperature compared to the material with constant properties. On the flap,
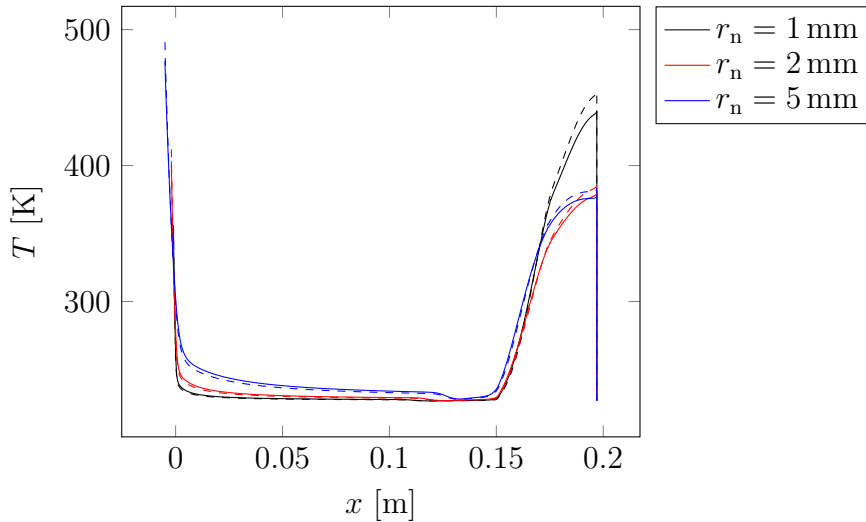
Figure 5.26: Effect of variable material properties: temperature distribution along the 20° 2D flap; temperature-dependent material properties are shown in solid lines, constant properties are dashed

the largest difference is observed for $r_n = 1\,\mathrm{mm}$, where using temperature-dependent material properties results in a $14\,\mathrm{K}$ reduction of the peak temperature.

The impact on the temperature distribution is not negligible and the temperature-dependency of the solid material should be taken into consideration. Since different materials can show drastically different temperature-dependencies, the exact composition of the solid material must be known, however. Furthermore, the data in [41] is only given for the temperature range $20\,°\mathrm{C}$ to $600\,°\mathrm{C}$. Extrapolation outside this range with the polynomial given in equation (5.6) may result in significant deviation from the real distribution due to the high-order terms. For these reasons, the remainder of the investigations were conducted using constant material properties.

5.4.5 3D Effects

To investigate the flow around a more realistic geometry, a 3D version of the generic flap was simulated. The geometry of the body is shown in figure 5.27. The symmetry axis in the $x - z$ plane matches the 2D case. In y-direction, the flap has a width of $50\,\mathrm{mm}$ and the distance to the sides of the computational domain are also $50\,\mathrm{mm}$. Analogous to the 2D case, the entire volume of the flap was treated as solid material.

The surface temperature of coupled 3D simulations are shown in figures 5.28 to 5.30 for $r_n = 5\,\mathrm{mm}$ and $\alpha = 20°$, $\alpha = 25°$, and $\alpha = 30°$, respectively. The plot also shows surface streamlines in black, which follow the surface shear stress vector. Similar to the 2D case, the flap generates a flow separation. While for 2D flows, the separation and attachment locations are defined by $\tau_{W,x} = 0$, in 3D, they are visible as converging and diverging streamlines, respectively. Figure 5.28 also shows the location of the separation line and reattachment line.
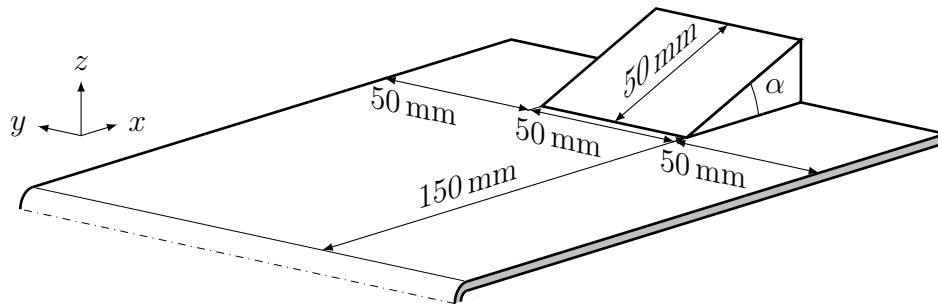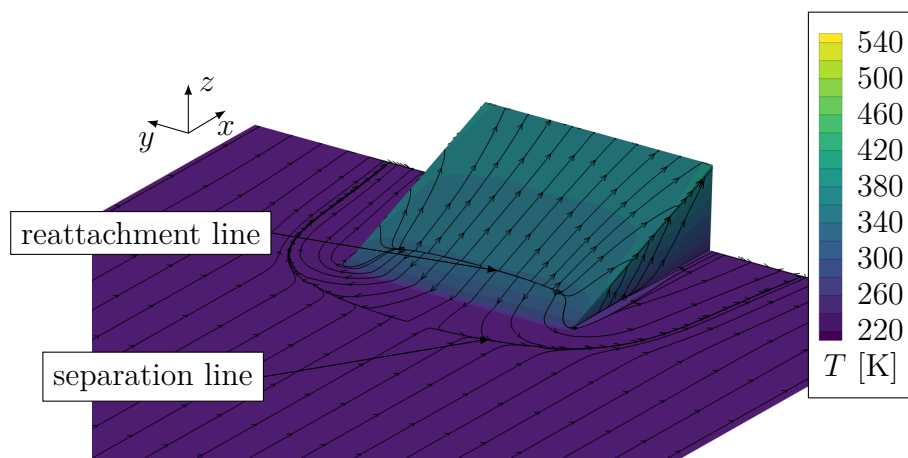
Figure 5.27: Geometry of the 3D generic flap case

Figure 5.28: Temperature distribution on the 3D flap with $\alpha = 20°$ and $r_{\mathrm{n}} = 5\,\mathrm{mm}$; surface streamlines are shown in black

The separation line for all angles has a horseshoe shape with significant shear stress in y-direction near the sides of the flap. Reattachment occurs at a line about $1/4$ along the length of the flap. Near the sides of the flap, separation moves downstream and reattachment moves upstream, the separation bubble therefore decreases in size near the sides of the flap. As the flap angle increases the separation length grows, which is in agreement with the 2D simulations.

The fluid is deflected from the center of the flap and passes the side edges of the flap. Due to that, a vortex forms in the corner between the main body and the side of the flap. This can be seen as two divergent streamlines along the flap.

3D effects are also visible in the temperature distribution. A significant increase in surface temperature is visible near the edges on the sides of the flap. The highest temperature for all flap angles can therefore be found at the top corners of the flap. This shows the necessity for 3D simulations with a 3D CHT approach, since a 1D solid model would fail to capture the impact of the sides of the flap.

To compare the impact of 3D effects on the flap temperature quantitatively, the temperature along the center of the flap for coupled 2D and 3D simulations with $r_{\mathrm{n}} = 5\,\mathrm{mm}$ are shown in figure 5.31. The 3D simulations produce higher temperatures
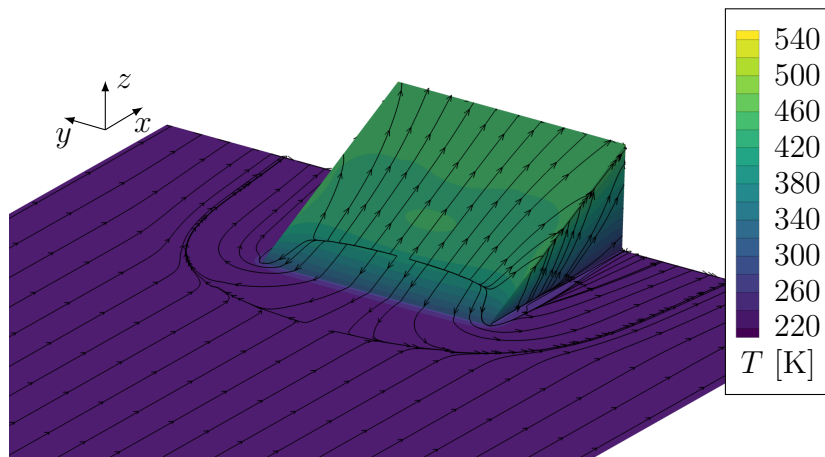
Figure 5.29: Temperature distribution on the 3D flap with $\alpha = 25°$ and $r_{\mathrm{n}} = 5\,\mathrm{mm}$; surface streamlines are shown in black
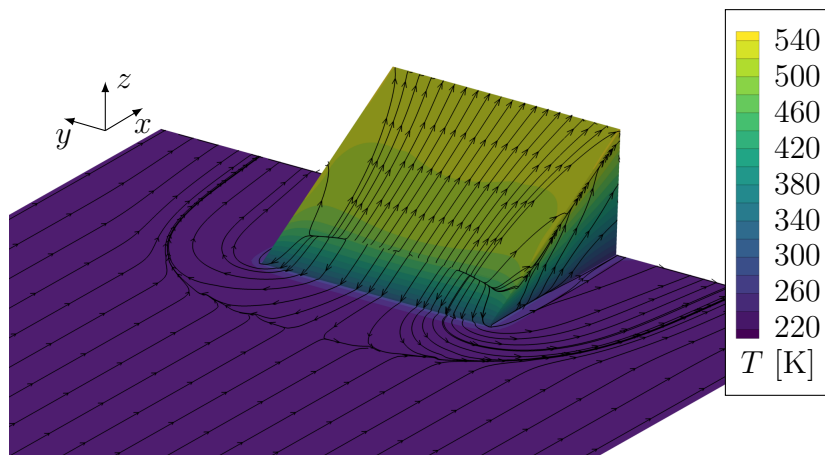
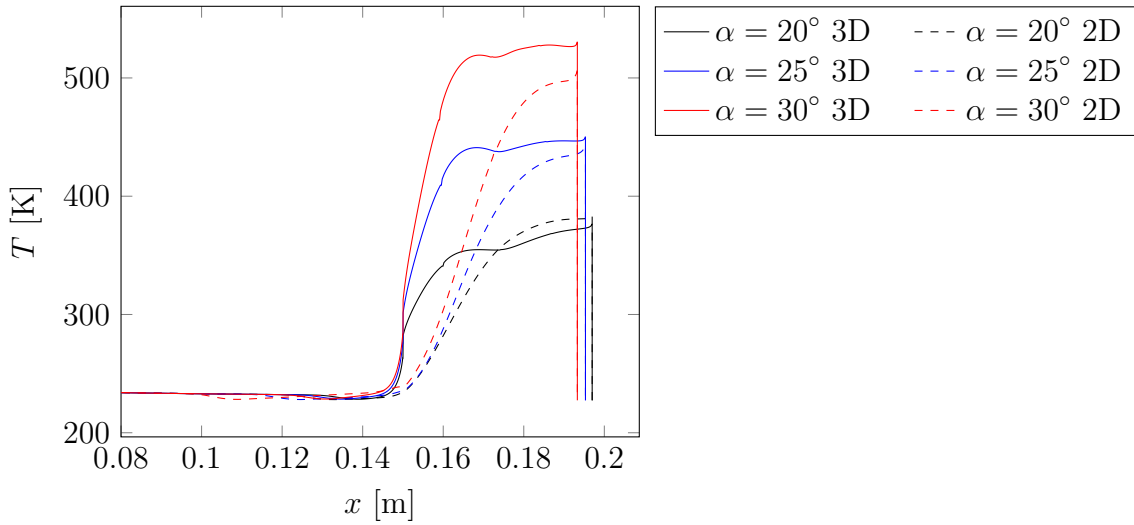Figure 5.30: Temperature distribution on the 3D flap with $\alpha = 30°$ and $r_{\mathrm{n}} = 5\,\mathrm{mm}$; surface streamlines are shown in black

Figure 5.31: Comparison of the axial temperature distribution along the flap in coupled 2D and 3D simulations with $r_\mathrm{n} = 5\,\mathrm{mm}$

for all flap angles and a distinctly different shape to the temperature distribution. The temperature increase at the upstream corner of the flap is significantly stronger in the 3D cases, all of which also show a local minimum at $x \approx 0.17\,\mathrm{m}$.

Figure 5.32 shows the spanwise temperature distribution on the 3D flap with $r_\mathrm{n} = 5\,\mathrm{mm}$ and $\alpha = 20°$ at five equidistant locations between the upstream corner of the flap ($x_0 = 0.15\,\mathrm{m}$) and the lip of the flap ($x_4 = 0.196\,98\,\mathrm{m}$). As can be seen in the previous contour plots, the temperature increases with axial position. The plot shows a significant spanwise temperature variation in a $10\,\mathrm{mm}$ wide region near the sides of the flap. Overall the spanwise variation is relatively small, but due to the large difference between 2D and 3D simulations, 3D simulations are still required.

5.4.6   Flap effectiveness

To analyze the aerodynamic properties of the flap, the aerodynamic forces on a $150\,\mathrm{mm}$ wide section of the body are analyzed. The coefficient for the vertical force can be defined as:

$$C_z = \frac{2|F_{z,150}|}{\rho_\infty U_\infty^2 A_\mathrm{ref}}. \tag{5.7}$$

Note that the lower half of the body was neglected in the simulations. The change of the aerodynamic coefficients between configurations is therefore of interest, rather than their absolute values.

The flap effectiveness can then be determined as the rate of change of the coefficient with flap angle $\mathrm{d}C_z/\mathrm{d}\alpha$. Table 5.5 shows the coefficient of the vertical force on the 2D flap geometries. The vertical force increases as the flap is extended. This effect is similar for all nose radii of the forebody with $\Delta C_z/\Delta\alpha = 8 \times 10^{-5}\,1/°$ on the smallest nose radius and $\Delta C_z/\Delta\alpha = 7 \times 10^{-5}\,1/°$ on the larger two radii. At the same flap angle, the force also increases with nose radius.
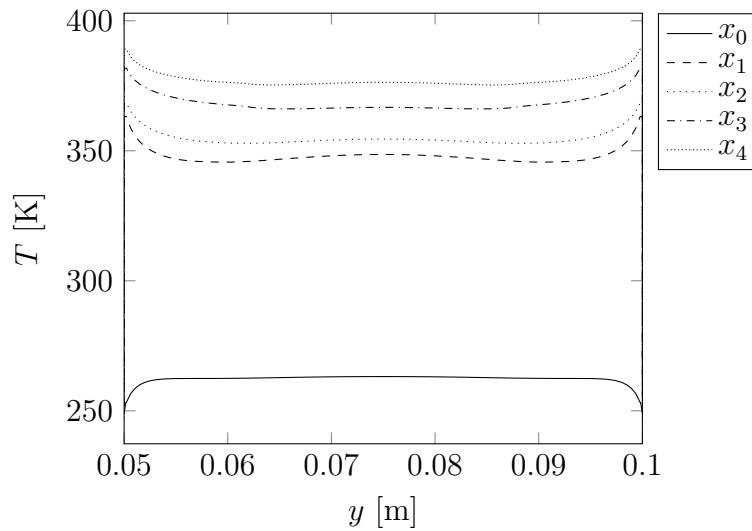
Figure 5.32: Spanwise temperature distribution on the 3D flap at five equidistant locations between the beginning and the end of the flap

		α		
		$20°$	$25°$	$30°$
	$1\,\mathrm{mm}$	0.0025	0.0030	0.0033
r_n	$2\,\mathrm{mm}$	0.0027	0.0031	0.0034
	$5\,\mathrm{mm}$	0.0036	0.0039	0.0043

Table 5.5: Coefficient of the vertical force C_z on the 2D flaps

		$\boldsymbol{\alpha}$		
		$20°$	$25°$	$30°$
	$1\,\text{mm}$	0.0018	0.0020	0.0023
r_n	$2\,\text{mm}$	0.0021	0.0022	0.0024
	$5\,\text{mm}$	0.0030	0.0031	0.0032

Table 5.6: Coefficient of the vertical force C_z on the 3D flaps

The corresponding data for the 3D flaps is shown in table 5.6. Since the 3D flap only covers $1/3$ of the width of the body, the vertical forces are smaller than in the 2D case. Again, the vertical force increases with flap angle, but the effectiveness decreases as the nose radius is increased. It is $\Delta C_z / \Delta\alpha = 5 \times 10^{-5}\,1/°$ on $r_n = 1\,\text{mm}$, $\Delta C_z / \Delta\alpha = 3 \times 10^{-5}\,1/°$ on $r_n = 2\,\text{mm}$, and $\Delta C_z / \Delta\alpha = 2 \times 10^{-5}\,1/°$ on $r_n = 5\,\text{mm}$. This shows firstly that the flap effectiveness decreases with nose radius since the entropy layer is thicker, and secondly that these effects are more relevant in the 3D case.

CHAPTER 6

Conclusion

6.1 Summary

In this thesis, the development and application of a conjugate heat transfer coupling method in the CFD solver NSMB is described. Using the finite-volume method, the unsteady time-accurate heat equation was implemented and coupled to the fluid domain. The development was focused on including all relevant heat fluxes at the interface between domains, which requires an iterative solution due to the diffusion and radiation heat fluxes. These implemented methods were then validated against a range of different cases that test different aspects of the problem. With the newly developed methods, different problems of hypersonic flight were investigated.

Since the CHT problem involves the physics in multiple domains, accurate results can only be obtained when all domains are treated appropriately. First, a numerical study was conducted to find appropriate treatments of the inviscid fluxes, the turbulent heat flux, and the mesh. Adapting the mesh to the detached bow shock has shown to improve convergence and accuracy significantly. The turbulent heat flux model by Roy, Pathak, and Sinha has also shown to improve the heat flux prediction near impinging shock waves.

A thorough investigation of the numerical treatment of the finite-difference operator at the solid/fluid interface was then conducted. A flat plate case in incompressible and hypersonic flow and a hollow spherical body in hypersonic flow were used. It showed that the second-order method significantly increases the mesh dependence compared to the first-order method. While this means that mesh refinement has a greater impact on the result, in all the investigated cases it has shown to make mesh convergence more difficult to achieve. Furthermore, the deficiencies of using an excessively coarse mesh are amplified with the second-order method. The first-order method is therefore favored.

In a complete implementation of the CHT method, the heat flux due to species diffusion must be included in the coupling method between the solid and fluid domains. The relevance of this heat flux component was analyzed with the hollow sphere case, which shows that it is of secondary importance in an equilibrium flow at the moderate hypersonic Mach numbers investigated here. Only in the direct vicin-

ity of the stagnation point there is a notable contribution from species diffusion of about 3 %, which quickly decreases along the nose. Since the diffusion heat flux does not have a significant impact on the overall computational effort, it should still be included in simulations with reacting flows. Furthermore, the Mach numbers in the investigations are in the lower range of hypersonic flows. In higher Mach number flows the temperature in the shock layer is higher, which increases dissociation and results in larger mass fraction gradients near the wall. The current implementation only works for equilibrium flows. In non-equilibrium flows, mass fraction gradients may be higher in regions with a low Damköhler number, which would increase the effect of the species diffusion heat flux. Similarly, regions with large temperature gradients, e.g., shocks also introduce mass fraction gradients and affect the species diffusion heat flux.

The challenging shock wave/turbulent boundary layer interaction case by Schülein [126] was investigated with and without the structural heating method. Like other numerical studies, the heat flux is strongly overpredicted compared to the experiment when using an isothermal wall. Traditionally, this is treated as a deficiency of the RANS turbulence model. However, treating the case as a transient CHT problem, the agreement to the experiment can be improved significantly. This shows the importance of including structural heating simulations even for cases where traditionally an isothermal wall would be assumed to sufficiently represent the problem.

The hollow sphere CHT case revealed an interesting effect regarding the distribution of the heat flux. The heat flux distribution along an isothermal spherical nose section has a local maximum at the stagnation point and then decreases monotonically along the body. In a CHT simulation, in contrast, the heat flux has a second local maximum about halfway along the spherical nose. This is due to the decreasing surface temperature along the nose, which must be determined with a coupled CHT simulation.

The generic flap case underlined the importance of an accurate determination of the thermal state of the surface for aerodynamic predictions. Increasing solid body temperature results in an increased separation length, which affects heat transfer and aerodynamic properties. Separation size is also strongly affected by the forebody nose radius, as the longest separation occurs with the smallest radius. Strong 3D-effects are also visible on the flap, which results in an increased temperature on the centerline of the control surface compared to the 2D case. On the 3D flap, the maximum temperature occurs on the sides of the flaps, which may require special attention for thermal management.

6.2   Outlook

Multiple opportunities for future expansions of the methods present themselves. Firstly, a comparison of the implemented finite-volume method to a finite-element approach could be done. The FEM approach enjoys a more widespread application for structural mechanics and may offer some advantages. Combining multiple domains

with different solution approaches may, however, also present challenges.

Furthermore, an investigation into faster solution approaches for transient simulations would be beneficial. In the transient simulations in this thesis, the method of equalizing the timescales between the solid and fluid domains was used. It offers a drastic acceleration of the simulations while preserving the accuracy of the simulation, but can become limited by stability constraints. As explained in chapter 3, the maximum allowed timestep in the solid domain is inversely proportional to the thermal diffusivity of the material. As a timescale factor $c_{ET} > 1$ is used, the maximum timestep in the solid reduces by a factor of c_{ET}. The solid domain may then impose a stricter limit on the global timestep than the fluid. At that point, the method of equalizing timescales is no longer effective. For short durations in the order of seconds or milliseconds, the method produces acceptable computational cost. When longer timespans should be simulated, e.g., the entire trajectory of a hypersonic plane, the computational effort is excessive. This is especially true for full 3D simulations. Future studies should investigate loose coupling methods that may trade accuracy for efficiency for these applications.

Lastly, the implemented methods can be used as a base for ablation simulations. Additional species transport equations in the solid domain would have to be included, and the coupling condition would have to account for melting, sublimation, and chemical decomposition of the solid body. If the surface regression due to ablation should be simulated, automatic remeshing would be required. This could be built upon the implemented methods for bow shock adaptation.

Bibliography

[1]   Hirschel, E. H. *Basics of Aerothermodynamics*. Berlin and Heidelberg: Springer, 2005.

[2]   Anderson, J. *Hypersonic and High Temperature Gas Dynamics*. 2nd ed. Reston: American Institute of Aeronautics and Astronautics, 2000.

[3]   Blain, L. *"Russia's Elon Musk" is developing hypersonic rocket cargo planes*. 9.02.2022. URL: https://newatlas.com/aircraft/destinus-hypersonic-aircraft/ (visited on Aug. 28, 2023).

[4]   Fry, R. S. "A Century of Ramjet Propulsion Technology Evolution". In: *Journal of Propulsion and Power* 20.1 (2004), pp. 27–58. DOI: 10.2514/1.9178.

[5]   Edney, B. *Anomalous Heat Transfer and Pressure Distributions on Blunt Bodies at Hypersonic Speeds in the Presence of an Impinging Shock*. 1968. DOI: 10.2172/4480948.

[6]   Watts, J. D. *Flight Experience with Shock Impingement and Interference Heating on the X-15-2 Research Airplane*. 1968.

[7]   Brown, S. N., Cheng, H. K., and Lee, C. J. "Inviscid–Viscous Interaction on Triple-Deck Scales in a Hypersonic Flow With Strong Wall Cooling". In: *Journal of Fluid Mechanics* 220 (1990), pp. 309–337. DOI: 10.1017/S0022112090003275.

[8]   Exposito, D., Gai, S. L., and Neely, A. J. "Wall Temperature and Bluntness Effects on Hypersonic Laminar Separation at a Compression Corner". In: *Journal of Fluid Mechanics* 922 (2021). DOI: 10.1017/jfm.2021.474.

[9]   Brauckmann, G. J., Paulson, J. W., and Weilmuenster, K. J. "Experimental and Computational Analysis of Shuttle Orbiter Hypersonic Trim Anomaly". In: *Journal of Spacecraft and Rockets* 32.5 (1995), pp. 758–764. DOI: 10.2514/3.26680.

[10]   COESA. *U.S. Standard Atmosphere*. Washington, D.C., 1976.

[11]   Sutherland, W. "The Viscosity of Gases and Molecular Force". In: *The London, Edinburgh, and Dublin Philosophical Magazine and Journal of Science* 36.223 (1893), pp. 507–531. DOI: 10.1080/14786449308620508.

[12]   Hillje, E. R. *Entry Aerodynamics at Lunar Return Conditions Obtained from the Flight of Apollo 4 (AS-501)*. Washington, D.C., 1969.

[13]   Stappert, S., Wilken, J., Bussler, L., and Sippel, M. "A Systematic Comparison of Reusable First Stage Return Options". In: *8th European Conference for Aeronautics and Space Sciences EUCASS*. 2019.

[14]   Langener, T. and Steelant, J. "Trajectory Simulation and Optimization of the LAPCAT-MR2 Hypersonic Cruiser Concept". In: *29th Congress of the International Council of the Aeronautical Sciences*. 2014.

[15]   Wagner, A., Wartemann, V., Kuhn, M., Dittert, C., and Hannemann, K. "The Potential of Ultrasonically Absorptive TPS Materials for Hypersonic Vehicles". In: *20th AIAA International Space Planes and Hypersonic Systems and Technologies Conference*. Reston, Virginia: American Institute of Aeronautics and Astronautics, 2015. DOI: `10.2514/6.2015-3576`.

[16]   Fay, J. A. and Riddell, F. R. "Theory of Stagnation Point Heat Transfer in Dissociated Air". In: *Journal of the Aerospace Sciences* 25.2 (1958), pp. 73–85. DOI: `10.2514/8.7517`.

[17]   Zoby, E. V., Moss, J. N., and Sutton, K. "Approximate Convective-Heating Equations for Hypersonic Flows". In: *Journal of Spacecraft and Rockets* 18.1 (1981), pp. 64–70. DOI: `10.2514/3.57788`.

[18]   Bershader, D. "9.2. Shock Tubes and Tunnels". In: *Fluid Dynamics*. Vol. 18. Methods in Experimental Physics. Elsevier, 1981, pp. 785–796. DOI: `10.1016/s0076-695x(08)60886-8`.

[19]   Auweter-Kurtz, M. and Wegmann, T. *Overview of IRS Plasma Wind Tunnel Facilities*. Universität Stuttgart, Institut für Raumfahrtsysteme, 2000.

[20]   Dorfman, A. and Renner, Z. "Conjugate Problems in Convective Heat Transfer: Review". In: *Mathematical Problems in Engineering* 2009 (2009), pp. 1–27. DOI: `10.1155/2009/927350`.

[21]   Ferrero, P. and D'Ambrosio, D. "A Numerical Method for Conjugate Heat Transfer Problems in Hypersonic Flows". In: *40th Thermophysics Conference*. Reston, Virginia: American Institute of Aeronautics and Astronautics, 2008. DOI: `10.2514/6.2008-4247`.

[22]   Murty, M. C. S., Manna, P., and Chakraborty, D. "Conjugate Heat Transfer Analysis in High Speed Flows". In: *Proceedings of the Institution of Mechanical Engineers, Part G: Journal of Aerospace Engineering* 227.10 (2013), pp. 1672–1681. DOI: `10.1177/0954410012464920`.

[23]   Peetala, R. K. "Conjugate Heat Transfer Analysis in Hypersonic Applications". PhD Thesis. Indian Institute of Technology Guwahati, 2014.

[24]   Zhang, S., Chen, F., and Liu, H. "Time-Adaptive, Loosely Coupled Strategy for Conjugate Heat Transfer Problems in Hypersonic Flows". In: *Journal of Thermophysics and Heat Transfer* 28.4 (2014), pp. 635–646. DOI: `10.2514/1.T4278`.

[25] Guo, S., Xu, J., Qin, Q., and Gu, R. "Fluid–Thermal Interaction Investigation of Spiked Blunt Bodies at Hypersonic Flight Condition". In: *Journal of Spacecraft and Rockets* 53.4 (2016), pp. 629–643. DOI: 10.2514/1.A33370.

[26] Qin, Q., Xu, J., and Guo, S. "Fluid-Thermal Analysis of Aerodynamic Heating Over Spiked Blunt Body Configurations". In: *Acta Astronautica* 132 (2017), pp. 230–242. DOI: 10.1016/j.actaastro.2016.12.037.

[27] Pogudalina, S. V., Goldfeld, M. A., Pickalov, V. V., and Fedorova, N. N. "Modeling of Conjugated Heat Transfer in Unsteady Hypersonic Flow". In: AIP Conference Proceedings. 2017, p. 030140. DOI: 10.1063/1.5007598.

[28] Reinert, J. D. "Conjugate Heat Transfer Simulations for Hypersonic Vehicles". PhD Thesis. University of Minnesota, 2020.

[29] Zope, A., Collins, E. M., Burgreen, G., Bhushan, S., Luke, E., and Dettwiller, I. D. "Towards More Efficient Fluid-Thermal Interaction Analysis for Hypersonic Trajectory Flights". In: *AIAA SCITECH 2023 Forum*. Reston, Virginia: American Institute of Aeronautics and Astronautics, 2023. DOI: 10.2514/6.2023-1039.

[30] Holman, J. P. *Heat Transfer*. 10. ed. McGraw-Hill series in mechanical engineering. Boston, Mass.: McGraw-Hill Higher Education, 2010.

[31] Balaji, C. *Heat Transfer Engineering: Fundamentals and Techniques*. San Diego: Elsevier Science & Technology, 2021.

[32] Tauber, M. E. *A Review of High-Speed, Convective, Heat-Transfer Computation Methods*. 1989.

[33] Chapman, S. and Cowling, T. G. *The mathematical theory of non-uniform gases: An account of the kinetic theory of viscosity, thermal conduction and diffusion in gases*. 3. ed. Cambridge mathematical library. Cambridge: Cambridge Univ. Press, 1998.

[34] Anderson, J. D. *Computational Fluid Dynamics: The Basics with Applications*. McGraw-Hill series in aeronautical and aerospace engineering. New York: McGraw-Hill, 1995. URL: http://www.loc.gov/catdir/description/mh022/94021237.html.

[35] de Nevers, N. *Physical and Chemical Equilibrium for Chemical Engineers*. 2. ed. Hoboken, NJ: Wiley, 2012. URL: http://www.loc.gov/catdir/enhancements/fy1210/2011046731-b.html.

[36] Ley, W., Wittmann, K., and Hallmann, W., eds. *Handbuch der Raumfahrttechnik*. 5th ed. München: Hanser, 2019. DOI: 45429.

[37] Mundt, Ch., Keraus, R., and Fischer, J. "New, Accurate, Vectorized Approximations of State Surfaces for the Thermodynamic and Transport Properties of Equilibrium Air". In: *Zeitschrift für Flugwissenschaften und Weltraumforschung* 15 (1991), pp. 179–184.

[38] Park, C. "On Convergence of Computation of Chemically Reacting Flows".
      In: *23rd Aerospace Sciences Meeting*. Reston, Virginia: American Institute of
      Aeronautics and Astronautics, 1985. DOI: 10.2514/6.1985-247.

[39] Blottner, F. G., Johnson, M., and Ellis, M. *Chemically Reacting Viscous Flow
      Program for Multi-Component Gas Mixtures*. 1971. DOI: 10.2172/4658539.

[40] Touloukian, Y. S. *Thermophysical Properties of High Temperature Solid ma-
      terials: Volume 3: Ferrous Alloys*. New York, 1966.

[41] *VDI-Wärmeatlas*. Berlin, Heidelberg: Springer Berlin Heidelberg, 2013. DOI:
      10.1007/978-3-642-19981-3.

[42] Bevington, P. R. and Robinson, D. K. *Data reduction and error analysis for
      the physical sciences*. 3. ed., [Nachdr.] Boston, Mass.: McGraw-Hill, 2003.

[43] Nieuwstadt, F. T. M., Boersma, B. J., and Westerweel, J. *Turbulence: Intro-
      duction to Theory and Applications of Turbulent Flows*. Cham: Springer, 2016.
      DOI: 10.1007/978-3-319-31599-7.

[44] Pope, S. B. *Turbulent Flows*. 1. ed. Cambridge: Cambridge Univ. Press, 2000.
      DOI: 44583.

[45] White, F. M. *Viscous Fluid Flow*. 2nd ed. McGraw-Hill series in mechanical
      engineering. New York: McGraw-Hill, 1991.

[46] Anderson, J. D. *Fundamentals of Aerodynamics*. 2. ed. McGraw-Hill series in
      aeronautical and aerospace engineering. New York: McGraw-Hill, 1991.

[47] Adams, N. A. and Stolz, S. "A Subgrid-Scale Deconvolution Approach
      for Shock Capturing". In: *Journal of Computational Physics* 178.2 (2002),
      pp. 391–426. DOI: 10.1006/jcph.2002.7034.

[48] Wilcox, D. C. *Turbulence Modeling for CFD*. Third edition. La Cañada, Cal-
      ifornia: DCW Industries, 2006.

[49] Smith, A. and Cebeci, T. *Numerical Solution of the Turbulent-Boundary-Layer
      Equations*. Douglas aircraft division report DAC 33735, 1967.

[50] Baldwin, B. and Lomax, H. "Thin-Layer Approximation and Algebraic Model
      for Separated Turbulent Flows". In: *16th Aerospace Sciences Meeting*. Reston,
      Virginia: American Institute of Aeronautics and Astronautics, 1978. DOI: 10.
      2514/6.1978-257.

[51] Spalart, P. and Allmaras, S. "A One-Equation Turbulence Model for Aero-
      dynamic Flows". In: *30th Aerospace Sciences Meeting and Exhibit*. Reston,
      Virginia: American Institute of Aeronautics and Astronautics, 1992. DOI: 10.
      2514/6.1992-439.

[52] Launder, B. E. and Sharma, B. I. "Application of the Energy-Dissipation
      Model of Turbulence to the Calculation of Flow Near a Spinning Disc". In:
      Letters in Heat and Mass Transfer 1.2 (1974), pp. 131–137. DOI: 10.1016/
      0094-4548(74)90150-7.

[53] Speziale, C. G., Abid, R., and Anderson, E. C. "Critical Evaluation of Two-Equation Models for Near-Wall Turbulence". In: *AIAA Journal* 30.2 (1992), pp. 324–331. DOI: 10.2514/3.10922.

[54] Tucker, H. J. and Reynolds, A. J. "The Distortion of Turbulence by Irrotational Plane Strain". In: *Journal of Fluid Mechanics* 32.4 (1968), pp. 657–673. DOI: 10.1017/S0022112068000947.

[55] Abe, K., Jang, Y.-J., and Leschziner, M. A. "An Investigation of Wall-Anisotropy Expressions and Length-Scale Equations for Non-Linear Eddy-Viscosity Models". In: *International Journal of Heat and Fluid Flow* 24.2 (2003), pp. 181–198. DOI: 10.1016/S0142-727X(02)00237-0.

[56] Wallin, S. and Johansson, A. V. "An Explicit Algebraic Reynolds Stress Model for Incompressible and Compressible Turbulent Flows". In: *Journal of Fluid Mechanics* 403 (2000), pp. 89–132. DOI: 10.1017/S0022112099007004.

[57] Speziale, C. G., Sarkar, S., and Gatski, T. B. "Modelling the Pressure–Strain Correlation of Turbulence: an Invariant Dynamical Systems Approach". In: *Journal of Fluid Mechanics* 227 (1991), pp. 245–272. DOI: 10.1017/S0022112091000101.

[58] Launder, B. E., Reece, G. J., and Rodi, W. "Progress in the Development of a Reynolds-Stress Turbulence Closure". In: *Journal of Fluid Mechanics* 68.3 (1975), pp. 537–566. DOI: 10.1017/S0022112075001814.

[59] Reynolds, O. "On the Extent and Action of the Heating Surface of Steam Boilers". In: *International Journal of Heat and Mass Transfer* 3.2 (1961), pp. 163–166. DOI: 10.1016/0017-9310(61)90087-4.

[60] Abe, H. and Antonia, R. A. "Turbulent Prandtl Number in a Channel Flow for Pr=0.025 and 0.71". In: *Proceedings of the 6th International Symposium on Turbulence and Shear Flow Phenomena (TSFP6)*. 2009, pp. 67–72.

[61] Kays, W. M. "Turbulent Prandtl Number—Where Are We?" In: *Journal of Heat Transfer* 116.2 (1994), pp. 284–295. DOI: 10.1115/1.2911398.

[62] Tavoularis, S. and Corrsin, S. "Experiments in Nearly Homogenous Turbulent Shear Flow with a Uniform Mean Temperature Gradient. Part 1". In: *Journal of Fluid Mechanics* 104 (1981), pp. 311–347. DOI: 10.1017/s0022112081002930.

[63] Schumann, U. "The Countergradient Heat Flux in Turbulent Stratified Flows". In: *Nuclear Engineering and Design* 100.3 (1987), pp. 255–262. DOI: 10.1016/0029-5493(87)90078-1.

[64] Paranthoën, P., Godard, G., Weiss, F., and Gonzalez, M. "Counter Gradient Diffusion vs "Counter Diffusion" Temperature Profile?" In: *International Journal of Heat and Mass Transfer* 47.4 (2004), pp. 819–825. DOI: 10.1016/j.ijheatmasstransfer.2003.08.026.

[65] Gatski, T. B. *Compressibility, Turbulence and High Speed Flow*. 2nd ed. Burlington: Elsevier Science, 2013. URL: http://www.sciencedirect.com/science/book/9780123970275.

[66] Xiao, X., Hassan, H. A., Edwards, J. R., and Gaffney, R. L. "Role of Turbulent Prandtl Numbers on Heat Flux at Hypersonic Mach Numbers". In: *AIAA Journal* 45.4 (2007), pp. 806–813. DOI: 10.2514/1.21447.

[67] Abe, H. and Antonia, R. A. "Mean Temperature Calculations in a Turbulent Channel Flow for Air and Mercury". In: *International Journal of Heat and Mass Transfer* 132 (2019), pp. 1152–1165. DOI: 10.1016/j.ijheatmasstransfer.2018.11.100.

[68] Roy, S., Pathak, U., and Sinha, K. "Variable Turbulent Prandtl Number Model for Shock/Boundary-Layer Interaction". In: *AIAA Journal* 56.1 (2018), pp. 342–355. DOI: 10.2514/1.J056183.

[69] Rogers, M. M., Mansour, N. N., and Reynolds, W. C. "An Algebraic Model for the Turbulent Flux of a Passive Scalar". In: *Journal of Fluid Mechanics* 203 (1989), pp. 77–101. DOI: 10.1017/S0022112089001382.

[70] Müller, H., Younis, B. A., and Weigand, B. "Development of a Compact Explicit Algebraic Model for the Turbulent Heat Fluxes and its Application in Heated Rotating Flows". In: *International Journal of Heat and Mass Transfer* 86 (2015), pp. 880–889. DOI: 10.1016/j.ijheatmasstransfer.2015.03.059.

[71] Leyland, P., Vos, J., van Kemenade, V., and Ytterstrom, A. "NSMB - A Modular Navier Stokes Multiblock Code for CFD". In: *33rd Aerospace Sciences Meeting and Exhibit*. American Institute of Aeronautics and Astronautics, 1995. DOI: 10.2514/6.1995-568.

[72] Vos, J., Rizzi, A., Corjon, A., Chaput, E., and Soinne, E. "Recent Advances in Aerodynamics inside the NSMB (Navier Stokes Multi Block) Consortium". In: *36th AIAA Aerospace Sciences Meeting and Exhibit*. Reston, Virginia: American Institute of Aeronautics and Astronautics, 1998. DOI: 10.2514/6.1998-225.

[73] Hoarau, Y., Pena, D., Vos, J. B., Charbonier, D., Gehri, A., Braza, M., Deloze, T., and Laurendeau, E. "Recent Developments of the Navier Stokes Multi Block (NSMB) CFD Solver". In: *54th AIAA Aerospace Sciences Meeting*. Reston, Virginia: American Institute of Aeronautics and Astronautics, 2016. DOI: 10.2514/6.2016-2056.

[74] Leyland, P., Bogstad, M. C., and Vos, J. "Navier Stokes Multiblock Calculations for High Speed Aerothermodynamics". In: *2nd European Symposium on Aerothermodynamics for Space Vehicles*. 1995.

[75] Walpot, L., Noeding, P., Tarfeld, F., Molina, R., Gülhan, A., and Paulat, J. C. "Transonic and Supersonic Static Stability Analysis of the CARV Reentry Vehicle". In: *14th AIAA/AHI Space Planes and Hypersonic Systems and Technologies Conference*. Reston, Virginia: American Institute of Aeronautics and Astronautics, 2006. DOI: 10.2514/6.2006-8077.

[76] Goebel, F., Vos, J., and Mundt, Ch. "CFD Simulation of the FIRE II Flight Experiment". In: *42nd AIAA Fluid Dynamics Conference and Exhibit*. Reston, Virginia: American Institute of Aeronautics and Astronautics, 2012. DOI: 10.2514/6.2012-3350.

[77] Charbonnier, D. and Vos, J. "Determination of Dynamic Derivatives of Reentry Vehicles using Unsteady CFD Simulations". In: *FAR 2019 International Conference on Flight Vehicles, Aerothermodynamics and Re-entry Missions & Engineering*. ESA, 2019.

[78] Al-Kebsi, A., Pena, D., Laurendeau, E., Mose, R., and Hoarau, Y. "Multi-Step Level-Set Ice Accretion Simulation with the NSMB solver". In: *23ème Congrès Français de Mécanique*. Association Française de Mecanique, 2017.

[79] Ziefle, J. and Kleiser, L. "Large-Eddy Simulation of a Round Jet in Crossflow". In: *36th AIAA Fluid Dynamics Conference and Exhibit*. 2006. DOI: 10.2514/6.2006-3370.

[80] Mundt, Ch., Vimercati, D., Lopez, S., Cleary, M., Thronber, B., and Michalski, Q. "Comparison of experimental and numerical results of a methane-oxygen rotating detonation engine". In: *Int. Symp. Shock Waves*. 2023.

[81] Vos, J. B. and Hoarau, Y. *NSMB Handbook Version 6.24*. 2022.

[82] Finlayson, B. A. and Scriven, L. E. "The Method of Weighted Residuals - A Review". In: *Applied Mechanics Reviews* 19.9 (1966), pp. 735–748.

[83] Pepper, D. W., Pirbastami, S., and Carrington, D. B. "A Comparison Between FEM and FVM via the Method of Weighted Residuals". In: *50 Years of CFD in Engineering Sciences*. Ed. by Runchal, A. Singapore: Springer Singapore, 2020, pp. 753–777. DOI: 10.1007/978-981-15-2670-1_21.

[84] Andersson, B., Andersson, R., Håkansson, L., Mortensen, M., Sudiyo, R., and van Wachem, B., eds. *Computational Fluid Dynamics for Engineers*. Cambridge University Press, 2012. DOI: 10.1017/CBO9781139093590.

[85] Moukalled, F., Mangani, L., and Darwish, M. *The Finite Volume Method in Computational Fluid Dynamics: An Advanced Introduction with OpenFOAM and Matlab*. Vol. volume 113. Fluid mechanics and its applications. Cham et al.: Springer, 2016.

[86] Benek, J., Buning, P., and Steger, J. "A 3-D Chimera Grid Embedding Technique". In: *7th Computational Physics Conference*. Reston, Virginia: American Institute of Aeronautics and Astronautics, 1985. DOI: 10.2514/6.1985-1523.

[87] Blazek, J. *Computational Fluid Dynamics*. 3rd ed. Burlington: Elsevier Science, 2015.

[88]   Von Neumann, J. and Richtmyer, R. D. "A Method for the Numerical Calculation of Hydrodynamic Shocks". In: *Journal of Applied Physics* 21.3 (1950), pp. 232–237. DOI: 10.1063/1.1699639.

[89]   Swanson, R. and Turkel, E. L. "Artificial Dissipation and Central Difference Schemes for the Euler and Navier-Stokes Equations". In: *8th Computational Fluid Dynamics Conference*. Reston, Virginia: American Institute of Aeronautics and Astronautics, 1987. DOI: 10.2514/6.1987-1107.

[90]   van Leer, B. "Flux-Vector Splitting for the Euler Equation". In: *Upwind and High-Resolution Schemes*. Ed. by Hussaini, M. Y., van Leer, B., and van Rosendale, J. Berlin, Heidelberg: Springer Berlin Heidelberg, 1997, pp. 80–89. DOI: 10.1007/978-3-642-60543-7_5.

[91]   Toro, E. F. *Riemann Solvers and Numerical Methods for Fluid Dynamics: A Practical Introduction*. 3. ed. Berlin and Heidelberg: Springer, 2009. URL: http://www.loc.gov/catdir/enhancements/fy1109/2009921818-d.html.

[92]   Godunov, S. K. and Bohachevsky, I. "Finite Difference Method for Numerical Computation of Discontinuous Solutions of the Equations of Fluid dynamics". In: *Matematičeskij sbornik, Steklov Mathematical Institute of Russian Academy of Sciences* 47(89).3 (1959), pp. 271–306.

[93]   Harten, A., Lax, P. D., and van Leer, B. "On Upstream Differencing and Godunov-Type Schemes for Hyperbolic Conservation Laws". In: *SIAM Review* 25(1) (1983), pp. 35–61. URL: http://www.jstor.org/stable/2030019.

[94]   Einfeldt, B. "On Godunov-Type Methods for Gas Dynamics". In: *SIAM Journal on Numerical Analysis* 25.2 (1988), pp. 294–318. DOI: 10.1137/0725021.

[95]   Toro, E. F., Spruce, M., and Speares, W. "Restoration of the Contact Surface in the HLL-Riemann Solver". In: *Shock Waves* 4.1 (1994), pp. 25–34. DOI: 10.1007/BF01414629.

[96]   Buck, A. and Mundt, Ch. "An Improved Riemann Solver for RANS Simulations". In: *AIAA SCITECH 2023 Forum*. Reston, Virginia: American Institute of Aeronautics and Astronautics, 2023. DOI: 10.2514/6.2023-1800.

[97]   Buck, A. and Mundt, Ch. "On the Extension of a Riemann Solver for RANS Simulations". In: *International Journal of Numerical Methods for Heat & Fluid Flow (under review)* (2024).

[98]   Sinha, K., Mahesh, K., and Candler, G. V. "Modeling Shock Unsteadiness in Shock/Turbulence Interaction". In: *Physics of Fluids* 15.8 (2003), pp. 2290–2297. DOI: 10.1063/1.1588306.

[99]   van Leer, B. "Towards the Ultimate Conservative Difference Scheme. V. A Second-Order Sequel to Godunov's Method". In: *Journal of Computational Physics* 32.1 (1979), pp. 101–136. DOI: 10.1016/0021-9991(79)90145-1.

[100] Harten, A., Engquist, B., Osher, S., and Chakravarthy, S. R. "Uniformly High Order Accurate Essentially Non-Oscillatory Schemes, III". In: *Journal of Computational Physics* 71.2 (1987), pp. 231–303. DOI: 10.1016/0021-9991(87)90031-3.

[101] van Albada, G. D., van Leer, B., and Roberts, W. W. "A Comparative Study of Computational Methods in Cosmic Gas Dynamics". In: *Upwind and High-Resolution Schemes*. Ed. by Hussaini, M. Y., van Leer, B., and van Rosendale, J. Berlin, Heidelberg: Springer Berlin Heidelberg, 1997, pp. 95–103. DOI: 10.1007/978-3-642-60543-7_6.

[102] van Leer, B. "Towards the Ultimate Conservative Difference Scheme. II. Monotonicity and Conservation Combined in a Second-Order Scheme". In: *Journal of Computational Physics* 14.4 (1974), pp. 361–370. DOI: 10.1016/0021-9991(74)90019-9.

[103] Venkatakrishnan, V. "Convergence to Steady State Solutions of the Euler Equations on Unstructured Grids with Limiters". In: *Journal of Computational Physics* 118.1 (1995), pp. 120–130. DOI: 10.1006/jcph.1995.1084.

[104] Peyret, R. and Taylor, T. D. *Computational Methods for Fluid Flow*. Corr. 3rd print. Springer series in computational physics. New York: Springer-Verlag, 1990.

[105] Wesseling, P., Segal, A., and Kassels, C. "Computing Flows on General Three-Dimensional Nonsmooth Staggered Grids". In: *Journal of Computational Physics* 149.2 (1999), pp. 333–362. DOI: 10.1006/jcph.1998.6156.

[106] Yoon, S. and Kwak, D. "Implicit Methods for the Navier-Stokes Equations". In: *Computing Systems in Engineering* 1.2-4 (1990), pp. 535–547. DOI: 10.1016/0956-0521(90)90034-I.

[107] Jameson, A. "Time Dependent Calculations Using Multigrid, With Applications to Unsteady Flows Past Airfoils and Wings". In: *AIAA 10th Computational Fluid Dynamics Conference*. 1991. DOI: 10.13140/2.1.2459.3608.

[108] Xie, W.-C. *Differential Equations for Engineers*. New York: Cambridge University Press, 2010. DOI: 10.1017/CBO9780511761683.

[109] Salas, M. D. "A Brief History of Shock-Fitting". In: *Computational Fluid Dynamics 2010*. Ed. by Kuzmin, A. Berlin, Heidelberg: Springer Berlin Heidelberg, 2011, pp. 37–53. DOI: 10.1007/978-3-642-17884-9_3.

[110] Harten, A. "High Resolution Schemes for Hyperbolic Conservation Laws". In: *Journal of Computational Physics* 49.3 (1983), pp. 357–393. DOI: 10.1016/0021-9991(83)90136-5.

[111] Carpenter, M. H. and Casper, J. H. "Accuracy of Shock Capturing in Two Spatial Dimensions". In: *AIAA Journal* 37.9 (1999), pp. 1072–1079. DOI: 10.2514/2.835.

[112]   Bonfiglioli, A., Paciorri, R., and Di Mascio, A. "The Role of Mesh Generation, Adaptation, and Refinement on the Computation of Flows Featuring Strong Shocks". In: *Modelling and Simulation in Engineering* 2012 (2012), pp. 1–15. DOI: 10.1155/2012/631276.

[113]   Berger, M. J. and Colella, P. "Local Adaptive Mesh Refinement for Shock Hydrodynamics". In: *Journal of Computational Physics* 82.1 (1989), pp. 64–84. DOI: 10.1016/0021-9991(89)90035-1.

[114]   Ameur, F. B. and Lani, A. *Physics-Based R-Adaptive Algorithms for High-Speed Flows and Plasma Simulations.* 2018. DOI: 10.48550/arXiv.1808.09445.

[115]   Höld, R. and Fornasier, L. "Investigation of Thermal Loads of Hypersonic Vehicles with Emphasis on Surface Radiation Effects". In: *19th Congress of the International Council of the Aeronautical Sciences.* 1994.

[116]   Gamet, L., Ducros, F., Nicoud, F., and Poinsot, T. "Compact Finite Difference Schemes on Non-Uniform Meshes. Application to Direct Numerical Simulations of Compressible Flows". In: *International Journal for Numerical Methods in Fluids* 29.2 (1999), pp. 159–191. DOI: 10.1002/(SICI)1097-0363(19990130)29:2<159::AID-FLD781>3.0.CO;2-9.

[117]   He, L. and Oldfield, M. L. G. "Unsteady Conjugate Heat Transfer Modeling". In: *Journal of Turbomachinery* 133.3 (2011). DOI: 10.1115/1.4001245.

[118]   Koren, C., Vicquelin, R., and Gicquel, O. "Self-Adaptive Coupling Frequency for Unsteady Coupled Conjugate Heat Transfer Simulations". In: *International Journal of Thermal Sciences* 118 (2017), pp. 340–354. DOI: 10.1016/j.ijthermalsci.2017.04.023.

[119]   Diefenthal, M., Łuczyński, P., Rakut, C., Wirsum, M., and Heuer, T. "Thermo-mechanical Analysis of Transient Temperatures in a Radial Turbine Wheel". In: *Journal of Turbomachinery* 139.9 (2017). DOI: 10.1115/1.4036104.

[120]   Liu, Q. "Coupling Heat Transfer and Fluid Flow Solvers for Multi-Disciplinary Simulations". PhD thesis. Mississippi: Mississippi State University, 2003.

[121]   Montomoli, F., Adami, P., and Martelli, F. "A Finite-Volume Method for the Conjugate Heat Transfer in Film Cooling Devices". In: *Proceedings of the Institution of Mechanical Engineers, Part A: Journal of Power and Energy* 223.2 (2009), pp. 191–200. DOI: 10.1243/09576509JPE640.

[122]   Luikov, A. V. "Conjugate Convective Heat Transfer Problems". In: *International Journal of Heat and Mass Transfer* 17.2 (1974), pp. 257–265. DOI: 10.1016/0017-9310(74)90087-8.

[123]   Schlichting, H. and Gersten, K. *Grenzschicht-Theorie.* 9th ed. Springer eBook Collection Computer Science and Engineering. Berlin, Heidelberg and s.l.: Springer Berlin Heidelberg, 1997. DOI: 10.1007/978-3-662-07554-8.

[124]   Maffulli, R., Marinescu, G., and He, L. "On the Validity of Scaling Transient Conjugate Heat Transfer Characteristics". In: *Journal of Engineering for Gas Turbines and Power* 142.3 (2020). DOI: 10.1115/1.4045868.

[125]   Esfahanian, V., Herbert, T., and Burggraf, O. "Computation of Laminar Flow Over a Long Slender Axisymmetric Blunted Cone in Hypersonic Flow". In: *30th Aerospace Sciences Meeting and Exhibit.* Reston, Virginia: American Institute of Aeronautics and Astronautics, 1992. DOI: 10.2514/6.1992-756.

[126]   Schülein, E. "Skin Friction and Heat Flux Measurements in Shock/Boundary Layer Interaction Flows". In: *AIAA Journal* 44.8 (2006), pp. 1732–1741. DOI: 10.2514/1.15110.

[127]   Pezzella, G., Marini, M., Reimann, B., and Steelant, J. "Aerodynamic Design Analysis of the Hexafly-INT Hypersonic Glider". In: *20th AIAA International Space Planes and Hypersonic Systems and Technologies Conference.* Reston, Virginia: American Institute of Aeronautics and Astronautics, 2015. DOI: 10.2514/6.2015-3644.

[128]   Thöben, J., Bodmer, D., Liebhardt, B., and Gollnick, V. "Design of Hypersonic Airline Networks with respect to Passenger Demand and Flight Routing". In: *HiSST: 2nd International Conference on High-Speed Vehicle Science & Technology.* 2022.

[129]   Hermeus. *Halcyon.* 2023. URL: https://www.hermeus.com/halcyon (visited on Dec. 15, 2023).

[130]   Destinus. *Hypersonic.* 2023. URL: https://www.destinus.ch/hypersonic/ (visited on Dec. 15, 2023).

APPENDIX A

Implementation Details

The described methods and models were first implemented in NSMB version 6.09.14 and later integrated into NSMB version 6.09.24.

A new flag `isolid` was added for each block and set to 1 for all solid blocks. All blocks with `blocktype > 1` are automatically treated as solid blocks. Additionally, blocks can be marked as solid by setting `solidflag(blocknumber): 1` in the input file. Material properties can either be specified for all solid blocks, or assigned for each of the solid blocks separately using the blockwise input nomenclature.

The following files were added to the NSMB codebase to realize the CHT functionality:

routine	description
bc537.F	fill the solid/fluid interface boundary condition
bc580.F	fill isothermal/constant heat flux boundary condition for solid blocks
calcdiffcoeff.F	compute the species diffusion coefficient
calclambda.F	compute the thermal conductivity for fluids
chtinterface.F	communication between blocks at solid/fluid interfaces
cht_variables.F	module containing variables relevant for CHT
dtsolid.F	compute the timestep in solid blocks
fillchtedges.F	fill edges and corner ghost cells of solid blocks
flipwindow.F	ensure correct mapping at solid/fluid interfaces
initsolid.F	initialize solid blocks
solid_input.F	utility for parsing material input for solid blocks
solid_properties.F	utility for computing coefficients for temperature-dependent material properties
solidprop.F	compute solid material properties
solidsym.F	symmetry condition for solid blocks
updateconduction.F	advance solid blocks in time
updchtbc.F	update boundary conditions for CHT

The settings related to conjugate heat transfer simulations are added to the NSMB input file and follow the existing conventions. The following parameters are available:

Parameter	Description	Default
chtsolidproperties	0: constant properties 1: temperature-dependent properties	0
chtthermaldiffusivity	thermal diffusivity a for solids	-
chtheatcapacity	heat capacity c for solids	-
chtthermalconductivity	thermal conductivity λ for solids	-
chtthermaldiffusivitycoeff	coefficients for a	-
chtheatcapacitycoeff	coefficients for c	-
chtthermalconductivitycoeff	coefficients for λ	-
chtdtscheme	time scheme for solid blocks: rk4: 4-stage Runge-Kutta eul1: Euler explicit	rk4
chtdtfactor	CFL number for solids	0.3
chtETfactor	timescale-equalization factor	1.0
chtinterfaceorder	spacial order of solid/fluid interface 1: first order 2: second order	1
chtinterfacediffusion	0: neglect species diffusion at interfaces 1: include diffusion	1